

**Effects of alloying elements on the microstructure and
fatigue properties of cast iron for internal combustion engine
exhaust manifolds**

by

David J. Eisenmann

A dissertation submitted to the graduate faculty
in partial fulfillment of the requirements for the degree of

DOCTOR OF PHILOSOPHY

Major: Material Science and Engineering

Program of Study Committee:

Scott Chumbley, Major Professor

Alan M. Russell

Iver Anderson

Leonard J. Bond

Frank Peters

Iowa State University

Ames, Iowa

2015

Copyright © David J. Eisenmann, 2015. All rights reserved.

TABLE OF CONTENTS

	Page
LIST OF FIGURES	iv
LIST OF TABLES	viii
LIST OF EQUATIONS.....	ix
ACKNOWLEDGEMENTS.....	x
ABSTRACT	xi
CHAPTER 1 RESEARCH STATEMENT	1
CHAPTER 2 LITERATURE REVIEW.....	3
2.1 The Iron Carbon Phase Diagram	4
2.2 Basic Cast Iron Metallurgy	8
2.2.1 Types of Cast Iron.....	10
2.3 Alloying Contributions to Fe-C	16
2.3.1 Major Contributing Elements.....	16
2.3.2 Minor Contributing Elements.....	17
2.4 Oxidation and Scale Formation.....	18
2.5 Oxide (Scale) Defects	21
2.6 Oxide (Scale) Stress	22
2.7 Failure Mechanisms.....	24
2.8 Fatigue of Crack Growth Approaches for Cast Iron.....	28
2.9 Fatigue Factors of Cast Iron at High Temperature.....	34
2.10 Summary.....	37
CHAPTER 3 EXPERIMENTAL PROCEDURES	39
3.1 Composition Determination.....	40
3.2 Heat Treatments	42
3.3 Metallography.....	44
3.4 Ultrasonic Testing	46
3.5 Hardness Testing.....	47
3.6 Tensile Testing.....	48
3.7 High Temperature Fatigue Testing.....	49
CHAPTER 4 RESULTS AND DISCUSSION.....	61
4.1 Composition Determination.....	61
4.2 Heat Treatment	63
4.2.1 Room Temperature	63

4.2.2	600°C Heat Cycle.....	64
4.2.3	700°C Results	66
4.2.4	800°C Results	67
4.2.5	900°C Results	69
4.3	Metallurgy	70
4.4	Ultrasonic Testing	72
4.5	Hardness Testing.....	74
4.6	Tensile Testing.....	76
4.7	Fatigue Data Results.....	80
4.7.1	Temperature.....	81
4.7.2	Flexural Calculations.....	99
4.7.3	Model Curve Fit.....	107
CHAPTER 5 DISCUSSION OF RESULTS		113
5.1	Effects of the Addition of Mo and Si to Cast Iron.....	114
5.2	Mechanical Testing	120
5.3	Model Estimations.....	126
CHAPTER 6 GENERAL SUMMARY AND CONCLUSIONS.....		135
REFERENCES		139
APPENDIX A: THEORIES OF FATIGUE ESTIMATIONS		147
APPENDIX B: MICROSTRUCTURE IMAGES FROM HEAT TREATMENT ...		153
APPENDIX C: MICROSTRUCTURE OF 700°C HSM COMPOSITE IMAGE ..		161

LIST OF FIGURES

	Page
Figure 1 Fe-C Phase Diagram	4
Figure 2 BCC and FCC Crystal Structure	6
Figure 3 Grey Cast Iron	11
Figure 4 White Cast Iron	12
Figure 5 Malleable Cast Iron	13
Figure 6 Spheroidal Cast Iron	15
Figure 7 Samples as Received	39
Figure 8 GDS Spot Images on Samples	41
Figure 9 High Temperature Furnace	42
Figure 10 Mounting and Polishing Equipment	45
Figure 11 Nikon Microscope	45
Figure 12 Ultrasonic Equipment	47
Figure 13 Rockwell Hardness Tester	48
Figure 14 Instron Model # 5969	49
Figure 15 Interface Screen Shot for Fatigue Settings	50
Figure 16 Three Point Bend Specimen Dimensions	52
Figure 17 Features of High Temperature Furnace	53
Figure 18 Furnace with Load Frame	54
Figure 19 Inconel 718 Rods with Water Jacket	55
Figure 20 Bend Fixture with Inconel Rods	56
Figure 21 Three Point Bend Fixture with Sample	56

Figure 22	Furnace Equipment	57
Figure 23	External Extensometer	58
Figure 24	Complete Fatigue System.....	59
Figure 25	Graph of Alloy Composition	62
Figure 26	200X Edge of Samples without Heat Treatment	64
Figure 27	200X Interior of Samples without Heat Treatment	64
Figure 28	200X Edge of Samples with 600°C Heat Treatment	65
Figure 29	200X Interior of Samples with 600°C Heat Treatment	66
Figure 30	200X Edge of Samples with 30 Hour 700°C Heat Treatment	67
Figure 31	200X Edge of Samples with 30 Minute 700°C Heat Treatment	67
Figure 32	200X Edge of Samples with 30 Hour 800°C Heat Treatment	68
Figure 33	200X Edge of Samples with 30 Minute 800°C Heat Treatment	68
Figure 34	200X Edge of Samples with 30 Hour 900°C Heat Treatment	69
Figure 35	200X Edge of Samples with 30 Minute 900°C Heat Treatment	70
Figure 36	Grain Size Determination.....	70
Figure 37	Average Grain Size with 30 Hour Heat Treatment.....	71
Figure 38	Average Grain Size with 30 Minute Heat Cycle	72
Figure 39	Hardness Values after 30 Hour Heat Treatment.....	75
Figure 40	Hardness Versus Average Tensile Strength.....	76
Figure 41	Tensile Test Specimen	77
Figure 42	Tensile Specimens after Testing.....	78
Figure 43	HSM Tensile Test Results	79
Figure 44	50HS Tensile Test Results	79

Figure 45	HSM Displacement at 22°C	82
Figure 46	50HS Displacement at 22°C	82
Figure 47	Displacement Change for 50HS at Smaller Scale	83
Figure 48	HSM Micrograph at 22°C 200X.....	84
Figure 49	50HS Micrograph at 22°C 200X.....	84
Figure 50	50HS Displacement at 400°C	85
Figure 51	HSM Displacement at 400°C	86
Figure 52	50HS Micrograph at 400°C 200X.....	87
Figure 53	HSM Micrograph at 400°C 200X.....	87
Figure 54	50HS Displacement at 600°C	89
Figure 55	Deflection of 50HS at 600°C after Fatigue	89
Figure 56	HSM Displacement at 600°C	90
Figure 57	Deflection of HSM at 600°C after Fatigue	91
Figure 58	50HS Micrograph at 600°C 200X.....	92
Figure 59	HSM Micrograph at 600°C 200X.....	92
Figure 60	50HS Displacement at 700°C	94
Figure 61	HSM Displacement at 700°C	95
Figure 62	50HS Displacement at 700°C After 10K Cycles.....	95
Figure 63	HSM Displacement at 700°C After 10K Cycles.....	96
Figure 64	Deflection of 50HS at 700°C after Fatigue	96
Figure 65	Deflection of HSM at 700°C after Fatigue	97
Figure 66	50HS Micrograph at 700°C 200X.....	98
Figure 67	HSM Micrograph at 600°C 200X/500X	99

Figure 68	50HS Modulus Average at Temperatures.....	101
Figure 69	50HS Modulus Three Lower Temperatures.....	102
Figure 70	HSM Modulus Average at Temperatures.....	103
Figure 71	HSM Modulus Three Lower Temperatures.....	103
Figure 72	50HS Stress Average at Temperatures.....	104
Figure 73	HSM Stress Average at Temperatures.....	105
Figure 74	50HS Strain Average at Temperatures.....	106
Figure 75	HSM Strain Average at Temperatures.....	107
Figure 76	Instantaneous Curve Fit for 50HS.....	109
Figure 77	Instantaneous Curve Fit for HSM.....	109
Figure 78	Historical Curve Fit for 50HS.....	110
Figure 79	Historical Curve Fit for HSM.....	111
Figure 80	Position Min and Max for HSM 600°C.....	121
Figure 81	Formation of Mo Carbides.....	124
Figure 82	Calculated UMLCI vs. Experimental Data.....	128

LIST OF TABLES

	Page
Table 1	Common Fe-C Microstructure..... 8
Table 2	Qualities of Cast Iron 9
Table 3	Composition of Experimental Alloys 18
Table 4	Comparison of UML to UMLCI..... 33
Table 5	Sample Marking for Heat Treatment..... 43
Table 6	Composition of Experimental Alloys 61
Table 7	Heat treatment Grain Size 71
Table 8	30 Minute Heat Cycle Grain Size 71
Table 9	Values used in Ultrasonic Testing..... 73
Table 10	Results of Ultrasonic Testing 73
Table 11	Values of Hardness Testing..... 75
Table 12	Dimensions of Tensile Specimens..... 76
Table 13	Yield Strength of Alloys..... 80
Table 14	Variables Used in Model Fit..... 112
Table 15	Formulas for CE..... 114
Table 16	Elements Needed for CE Calculations..... 115
Table 17	Results of CE Calculations 115
Table 18	Microstructure Hardness Values..... 116
Table 19	Hardness to Tensile Strength 117
Table 20	Nodule Size Relative to Temperature 119
Table 21	Calculated Modulus versus Literature Values..... 125

LIST OF EQUATIONS

	Page
Equation 1 Total Stress	23
Equation 2 Manson-Coffin.....	31
Equation 3 Basquin	31
Equation 4 Failure Strain Rate	32
Equation 5 Uniform Material Law	32
Equation 6 Calculation of I	51
Equation 7 Maximum Load.....	51
Equation 8 Minimum Load.....	51
Equation 9 R ratio	51
Equation 10 Mean Load	51
Equation 11 Load Amplitude	51
Equation 12 Flexural Stress	100
Equation 13 Flexural Strain.....	100
Equation 14 Flexural Modulus.....	100
Equation 15 Exponential Curve Fitting	107
Equation 16 Uniform Material Law for Cast Iron.....	128
Equation 17 Modified Uniform Material Law for Cast Iron	131
Equation 18 Costa Fatigue Equation.....	132

ACKNOWLEDGEMENTS

I would like to thank my family for having the faith in me, and the support to see me through this process. I would particularly like to thank my wife, Vallery, and my mother for their encouragement during these last few years.

I would like to thank Dr. Scott Chumbley for being my advisor for over 16 years, and his guidance and direction throughout this whole process. I would also like to thank my Director at CNDE, Dr. Leonard Bond, for his support not only through assisting in the numerous equipment repairs, but for the encouragement and the time to complete this work.

Finally I would like to thank the field and technical support personnel at Instron for coming to my aid multiple times throughout the fatigue portion of this work.

ABSTRACT

In the design of exhaust manifolds for internal combustion engines the materials used must exhibit resistance to corrosion at high temperatures while maintaining a stable microstructure. Cast iron has been used for manifolds for many years by auto manufacturers due to a combination of suitable mechanical properties, low cost, and ease of casting. Over time cast iron is susceptible to microstructural changes, corrosion, and oxidation which can result in failure due to fatigue. This thesis seeks to answer the question: "Can observed microstructural changes and measured high temperature fatigue life in cast iron alloys be used to develop a predictive model for fatigue life?" the importance of this question lies in the fact that there is little data for the behavior of cast iron alloys at high temperature. For this study two different types of cast iron, 50HS and HSM will be examined. Of particular concern for the high Si+C cast irons (and Mo in the case of the HSM cast iron) are subsurface microstructural changes that result due to heat treatment including (1) decarburization, (2) ferrite formation, (3) graphitization, (4) internal oxidation of the Si, (5) high temperature fatigue resistance, and (6) creep potential. Initial results obtained include microstructure examination after being exposed to high temperatures, grain size, nodule size, and hardness measurements. The initial examinations concluded that both cast irons performed fairly similarly, although the microstructure of the HSM samples did show slightly better resistance to high temperature as compared to that of the 50HS. Follow on work involved high temperature fatigue testing of these two materials in order to better determine if the newer alloy, HSM

is a better choice for exhaust manifolds. Correlations between fatigue performance and microstructure were made and discussed, with the results examined in light of current and proposed models for predicting fatigue performance based on computational methods, to see if any suitable models exist that might be used to assist in designing with these cast alloys.

CHAPTER 1

RESEARCH STATEMENT

With the demand for cleaner, more efficient cars coupled with stricter emission controls and a desire for increased automotive horsepower at less weight comes an increase in the operating temperature of exhaust manifolds. In addition to the higher temperatures also comes a need for greater corrosion control in the cast iron alloys typically used for these manifolds. The increased temperatures have created several fundamental issues in the design of manifolds, such as; how to minimize the increased stress that come with higher temperatures and how to manage the thermal deformation which occurs as a result of thermal cycling. Over time, repeated cyclic thermal stress can cause plastic deformation and fracture to initiate [31].

The motivation for this study is the result of the development of a new heat resistant cast iron alloy by an automobile manufacturer, and is in direct response to the demand for higher efficiency automobiles. The specific alloys studied, being considered are typical of the types of alloys under consideration by other companies. Thus, this research should have application to many different alloy systems.

The two different types of cast iron used in manufacturing engine exhaust manifolds were received for this study. The first type, denoted as 50HS, meaning it is high in silicon, is typical of the type of cast iron currently used. The second, denoted as HSM, which stands for high amounts of silicon and molybdenum, is a

newer type of cast iron. Of particular concern for the high Si+C (and Mo in the case of the HSM cast iron) alloys is the need to investigate subsurface changes that result due to heat treatment including (1) decarburization, (2) ferrite formation, (4) graphitization, and (5) internal oxidation of the Si.

The objective of this study was to determine whether the newer HSM cast iron can better withstand exposure to conditions found in high temperature environments as compared to 50HS. By subjecting samples of each material to various conditions, this study examined the microstructure and fatigue properties of the alloys at different temperatures and load conditions. Testing conditions included: thermal cycling to measure corrosion resistance, grain growth and nodule changes. Hardness and ultrasonic testing to make estimations on tensile strength and modulus values, tensile testing to determine yield strength needed for fatigue testing and high temperature fatigue testing to characterize the behavior of cast iron while under load and high temperatures.

The goal of the study was to answer the question: "Can microstructural changes in cast iron due to high temperature exposure, and properties determined from experimental data obtained from the high temperature fatigue of cast iron alloys, be used with an existing fatigue life model, or used to develop a new fatigue life model?" Such predictions are known to be difficult given the wide range of possible microstructures and the non-linear elastic behavior of cast irons.

CHAPTER 2

LITERATURE REVIEW

Background

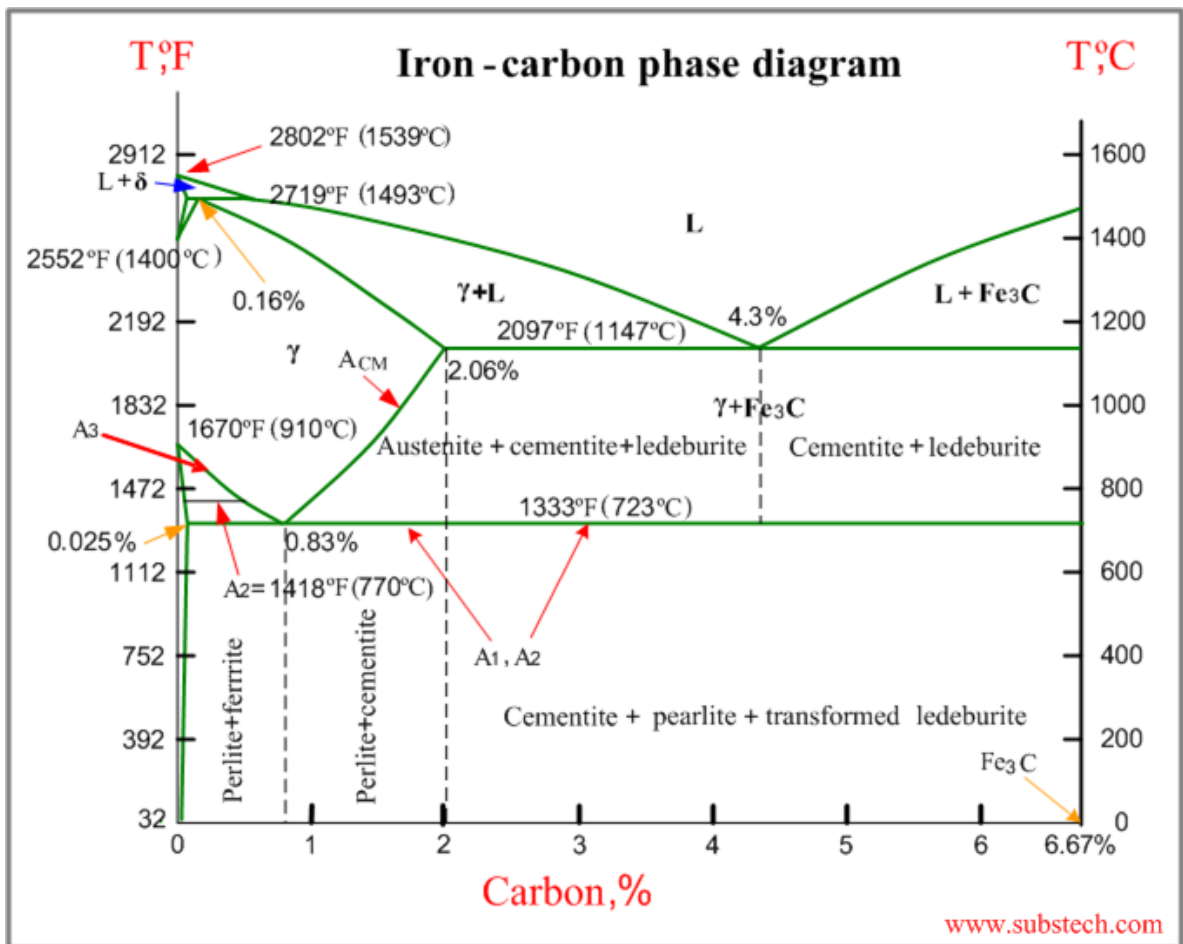
Ferrous metals have been known for their strength and durability in structural components for thousands of years [1]. Prior to the development of the technology needed for steel making, wrought iron (also sometimes known as malleable iron) was the most common type of iron. Wrought iron is tough, ductile, and malleable and is easily welded. It is often thought of as “pure iron” [2, 3]. The term wrought iron is still in use today, but it typically refers to that type of iron made by hand, not the type of iron originally developed in ancient times.

With the development of the open-hearth furnace and the Bessemer process, production of large amounts of steel began in the mid to late 1800's. At that time there were differing opinions as to what constituted steel and what differentiated it from that which was known as iron. Ultimately it was agreed that chemical composition (specifically carbon content) would be the ultimate deciding factor [4]. Alloys with the least amount of the element carbon (0 to 0.008 wt% C) were defined as wrought irons while alloys containing 0.008 wt% C to 2.14 wt% C were designated as steels. Steels are the most common type of ferrous alloys due to their extreme versatility in use. This versatility is derived primarily from the many different elements that are added to the steel, and the type of heat treatment to which that particular alloy is subjected.

The last category of ferrous metals is cast irons which contain anywhere from 2.14 wt% C to 4 wt% C. Like steels, the characteristics of cast iron are defined by the elemental composition of the alloy.

2.1 The iron-carbon phase diagram

The difference between steels and cast irons is best understood by examination of the iron-C phase diagram (Figure 1).

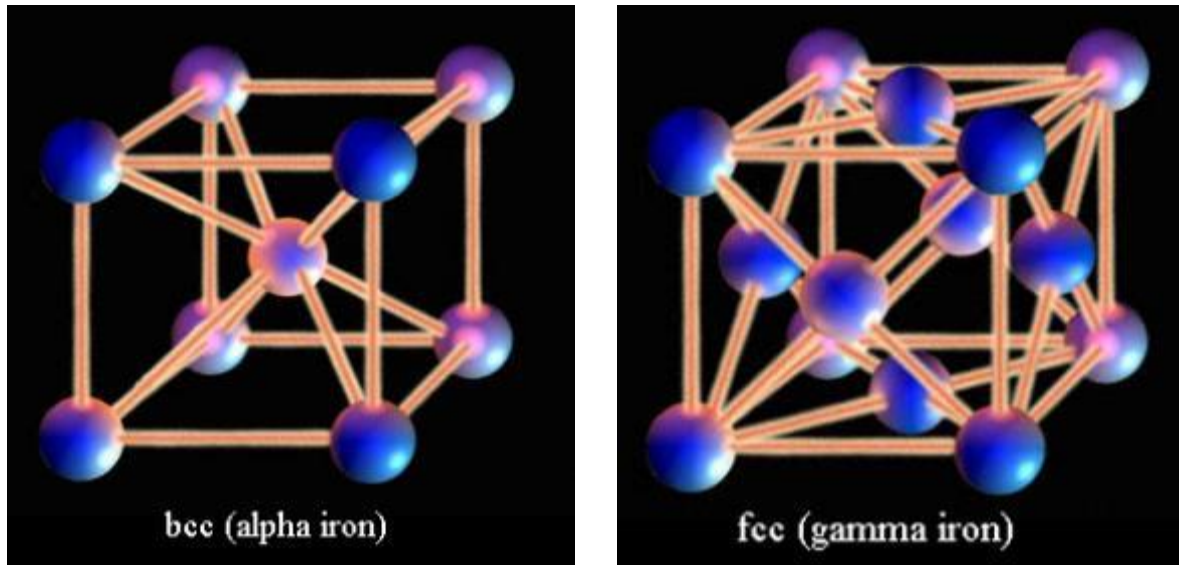


http://www.substech.com/dokuwiki/doku.php?id=iron-carbon_phase_diagram

Figure 1. Fe-C phase diagram showing the placement of steel and cast iron (Ledeburite is a mixture of 4.3% carbon in iron and is a eutectic mixture of austenite and cementite.)

A basic iron – carbon (Fe-C) phase diagram is divided into many different sections depending on the temperature (found along the Y axis) and carbon content (found along the X axis). An iron carbon phase diagram is essentially broken up into five distinct phases with a weight percentage of carbon (wt% C) ranging from a very low wt% C, up to 6.7 wt% C. The diagram is commonly truncated at this point, which denotes formation of a phase having the atomic composition Fe_3C known as cementite. In practical terms the region beyond 6.7 wt% is of no interest since this only represents an increasing percentage of carbon + Fe_3C (up to 100% carbon) having no engineering applications. The four distinct stable solid phases below 6.7 wt% in the diagram are; C (cementite, Fe_3C), alpha (α) ferrite, gamma (γ) austenite, and delta (δ) ferrite.

Alpha ferrite is a stable form of iron that exists at room temperature in a body centered cubic (BCC) crystal structure (Figure 2). The maximum solubility of carbon for this phase is 0.022 wt% C.



<http://www.cashenblades.com/metallurgy.html>

Figure 2. Illustration of BCC and FCC crystal structures

At a higher temperature of 912 °C the α ferrite transforms to γ austenite with a face centered cubic (FCC) crystal structure. Gamma austenite is a solid solution of carbon in an FCC crystal structure where the solubility of carbon in this phase reaches a maximum of 2.14 wt% C. Below a temperature of 727 °C this phase is not considered stable, unless rendered so by alloying additions. Above a temperature of 1395 °C the crystal structure changes from a FCC back to a BCC, resulting in δ ferrite. Delta ferrite is a solid solution of Fe-C that is only stable at higher temperatures above 1395 °C. Once the solid solution reaches a temperature of 1538 °C, the solution changes to a mixture of liquid and solid Fe-C.

Cementite is considered a metastable solid. This means that over time it will change to α ferrite and graphite (pure carbon) in a temperature range of 650

– 700 °C. The exact temperature that any of the phases change to the liquid form is determined by the alloy composition and the weight percent carbon.

The reason for the differences in the solubility of carbon into iron is related to the crystal structure of iron. Since carbon acts as an interstitial impurity, a crystal structure such as BCC, which has smaller interstitial positions, limits the amount of carbon that can be present. Larger crystal structures such as FCC have larger interstitial regions, which allow for greater solubility of carbon [5].

Today ferrous alloys are commonly divided into three classifications, which can be seen the phase diagram from page 10:

1. Iron: less than 0.008 wt% C in α ferrite at room temperature
2. Steels: 0.008 – 2.14 wt% C in α ferrite and Fe_3C at room temperature
3. Cast Iron: 2.14 – 6.7 wt % C

One of the reasons Fe-based alloys are often used is that different heating and cooling rates, especially when combined with other elemental alloying additions, creates a wide range of different microstructures that can have markedly different mechanical properties. In some cases additional metastable phases form whose crystal structure is different from either the stable FCC or BCC phases denoted on the phase diagram. The characteristic nature of these microstructures have caused them to obtain their own familiar designations, and a brief table of common microstructures is found below in Table 1.

Table 1. Table of common Fe-C microstructures [6]

Austenite	Solid solution of one or more alloying elements in the FCC polymorph of iron
Bainite	Eutectoid product of ferrite and a fine dispersion of carbide at temperatures below 450 – 500 °C
Upper Bainite	Aggregate containing parallel lath shaped unites of ferrite formed above 350 °C
Lower Bainite	Individual plate shaped units formed below 350 °C
Carbide	Compound of carbon and one or more metallic elements
Cementite	Metastable carbide of Fe ₃ C with limited substitutional solubility
Ferrite	A solid solution of one or more alloying elements in BCC iron
α ferrite	Solid solution of one or more alloying elements in the high temperature BCC iron (δ-Fe)
Graphite	Hexagonal polymorph of carbon
Ledeburite	Cementite with austenite or its lower temperature products – formed below 1148 °C
Martensite	In steel – formed by diffusionless transformation of austenite during cooling between the M _s and M _f temperatures
Pearlite	Eutectoid product of ferrite and cementite with an ideally lamellar structure whose spacing can change with cooling rate

2.2 Basic cast iron metallurgy

In the mid-15th century cast iron was beginning to be found in Western Europe, but due to its brittle nature was used only in certain circumstances [7]. It wasn't until the 1890's that issues in steel production were resolved and steel finally replaced iron as the standard material for structural applications [8].

Cast iron is defined by the content of carbon and silicon contained in the material. Typically, cast irons contain from 2.14 wt% to 4.0 wt% carbon and anywhere from 0.5 wt% to 3 wt% of silicon. Cast iron also has a lower melting point than traditional steel, which makes it easier to cast than standard steels. It is an ideal material for sand casting into complex shapes such as exhaust manifolds without the need for extensive further machining. Materials made from

cast iron tend to be resistant to the effects of oxidation. They tend to be brittle, which is not desirable for structural materials, but the fluidity and ease of casting makes it an excellent candidate for non-structural applications. Cast irons can be divided into four sub categories based upon their microstructure and composition. A basic table illustrating the comparative qualities of each category of cast iron is found below in Table 2.

Table 2. Comparative qualities of cast irons

Name	Nominal composition [% by weight]	Form and condition	Yield strength [ksi (0.2% offset)]	Tensile strength [ksi]	Elongation [% (in 2 inches)]	Hardness [Brinell scale]	Uses
Grey cast iron (ASTM A48)	C 3.4, Si 1.8, Mn 0.5	Cast	—	50	0.5	260	Engine cylinder blocks, flywheels, gearbox cases, machine-tool bases
White cast iron	C 3.4, Si 0.7, Mn 0.6	Cast (as cast)	—	25	0	450	Bearing surfaces
Malleable iron (ASTM A47)	C 2.5, Si 1.0, Mn 0.55	Cast (annealed)	33	52	12	130	Axle bearings, track wheels, automotive crankshafts
Ductile or nodular iron	C 3.4, P 0.1, Mn 0.4, Ni 1.0, Mg 0.06	Cast	53	70	18	170	Gears, camshafts, crankshafts
Ductile or nodular iron (ASTM A339)	—	cast (quench tempered)	108	135	5	310	—

Lyons, William C. and Plisga, Gary J. (eds.) *Standard Handbook of Petroleum & Natural Gas Engineering*, Elsevier, 2006

2.2.1 Types of cast iron

Grey cast iron

Grey cast iron is the oldest and most common type of iron in existence and probably what most people think of when they hear the term “cast iron”. Grey cast iron has good thermal conductivity and specific heat capacity, therefore it is often used in cookware and brake rotors [9]. Grey cast iron (Figure 3) is characterized by its grey appearance when fractured. This is due to the presence of graphite in its composition [10]. In grey cast iron the graphite forms as flakes, taking on a three dimensional geometry. The tips of these flakes act as preexisting notches, which results in a brittle structure [11]. The typical chemical makeup of grey cast iron is 2.5 – 4.0 wt% carbon, 1 – 3 wt% silicone, 0.4 – 1.0 wt% manganese, 0.05 – 0.25 wt% sulphur, 0.05 1.0 wt% phosphorus, and the remainder being made up of iron.



Figure 3. Grey Cast Iron <http://www.doitpoms.ac.uk/miclib/micrograph.php?id=62>

White cast iron

White cast iron (Figure 4) is referred to as such due to its whitish appearance when fractured. This appearance is a result of cementite (Fe_3C) found in the matrix. The presence of cementite in the matrix makes the cast iron hard, but not particularly tough. Materials made from white cast iron are typically brittle and therefore not used for structural materials. Because of the hardness and abrasion resistance of the Fe_3C , white cast iron is used in instances where wear resistance is desirable, such as on the teeth of excavators. White cast iron

can also be formed on the outer surfaces of castings. When a casting is cooled rapidly a thin lining or covering is formed on the outer surface of the casting. This outer layer of white cast iron surrounds the inner region of the casting, which is typically grey cast iron. This type of casting, sometimes referred to as a “chilled casting” has a harder outer surface and a tougher inner core. White cast typically has a lower carbon and silicon content, allowing for a hard brittle carbide to form with no free graphite [12]. White cast iron is composed of 1.8 – 3.6 wt% carbon, 0.5 – 2.0 wt% silicone, 0.2 – 0.8 wt% manganese, 0.06 – 0.2 wt% sulphur, 0.06 – 0.18 wt% phosphorus, and the remainder being made up of iron.

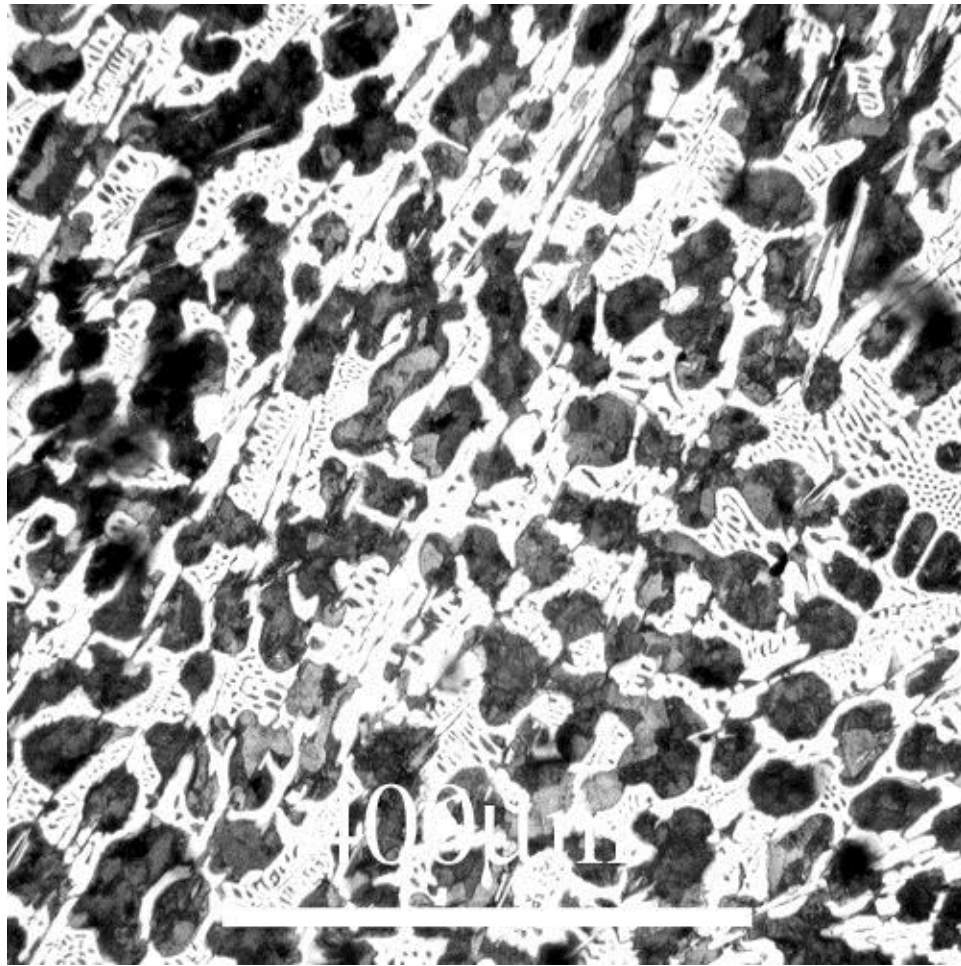


Figure 4. White Cast Iron (<http://www.doitpoms.ac.uk/miclib/micrograph.php?id=66>)

Malleable cast iron

Malleable cast iron (Figure 5) is white cast iron that has been annealed. Therefore, its composition is very similar to that of white cast iron, with slightly higher amounts of carbon and silicon. The weight percent of carbon in malleable cast iron ranges from 2.0 – 2.6, and the weight percent of silicon ranges from 1.1 – 1.6. During the annealing process carbon diffuses through the matrix and can gather into either small flakes, known as temper carbon, or as small nodules, depending on the amount of silicon or boron present [13]. The existence of these nodules in the matrix gives malleable cast iron good ductility. Malleable cast iron also exhibits greater fracture toughness at lower temperatures due to its lower silicon content. Uses of malleable cast iron include such things as hand tools, brackets and machine parts [14].

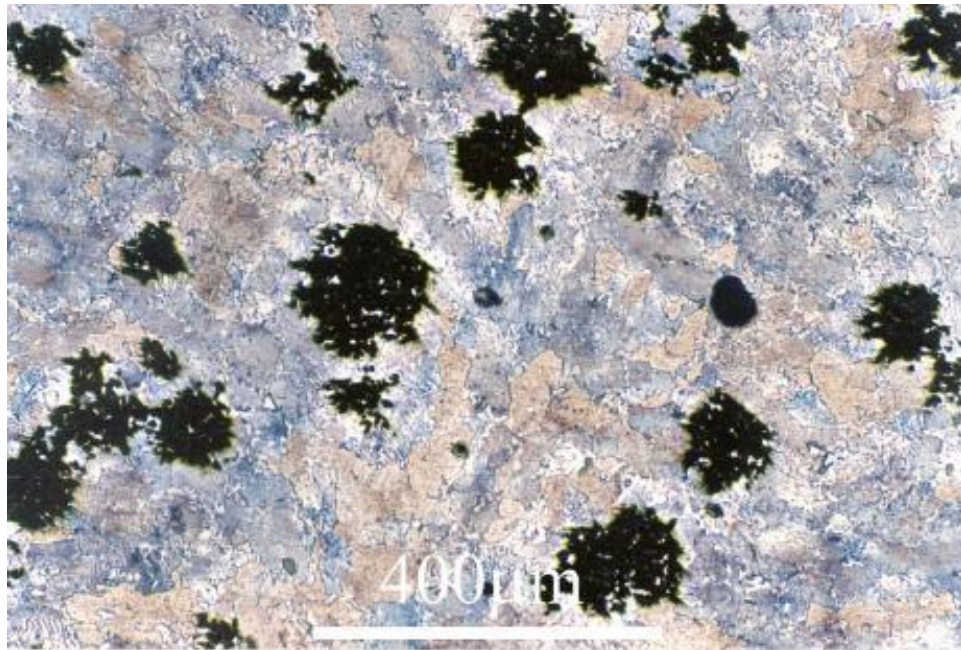


Figure 5. Malleable Cast Iron in a pearlite background
(<http://www.doitpoms.ac.uk/miclib/micrograph.php?id=354>)

Spheroidal or nodular cast iron

Although most versions of cast iron are often brittle, spheroidal cast iron (Figure 6) has much greater fatigue and impact resistance due to its nodular graphite inclusions [15]. By adding a small amount of magnesium or cerium to the alloy when in the liquid phase, the growth of graphite can be slowed during the solidification process. With an increase in silicon to the cast matrix, coupled with the magnesium and cerium additions, the carbon is much more likely to form nodules rather than flakes. This nodule formation helps increase the ductility of the cast, making it more desirable for certain applications. The background matrix of spheroidal cast is often a pearlite formation. A typical chemical composition consists of 2.3 to 3.4 wt% carbon, 2.2 to 2.8 wt% silicon, 0.003 to 0.005 wt% magnesium and lesser amounts of other trace elements. Uses of spheroidal cast iron include engine exhaust manifolds, oil well pumps and ductile iron pipe.

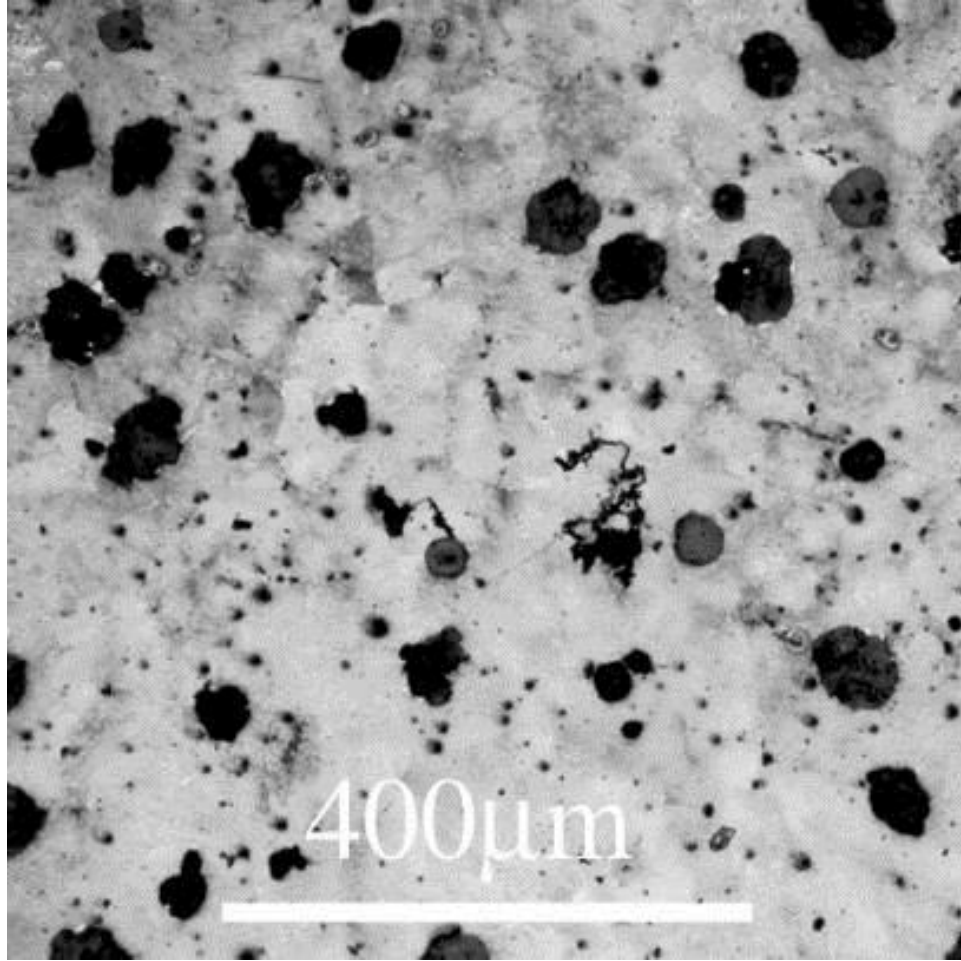


Figure 6. Spheroidal cast iron (<http://www.doitpoms.ac.uk/miclib/micrograph.php?id=64>)

The sensitivity of the cast alloys to composition, especially when coupled with controlled heating and cooling schedules, enable a wide variety of cast iron microstructures to be produced, having associated effects on the physical properties of the material such as hardness and toughness. In the following sections, the theoretical effects on the ultimate material properties of the two different alloys of cast iron examined in this research (HSM and 50HS) will be discussed. Topics will include; alloying effects, corrosion response, temperature resistance, changes in microstructure and material processing.

2.3 Alloying Contributions to Fe-C

As we discussed briefly earlier in this work, the Fe-C system is extremely flexible in that there are many different elements that can be added to affect its material properties and characteristics. Each element, either by itself or in conjunction with additional elements can greatly change the properties of the alloy under consideration. For the purpose of this thesis we will discuss only those elements that have a major effect on the behavior of the alloys, and several elements which have a minor effect on the behavior of the alloy. These elements were identified by either their wt% or their contributing effects. A list of all elements present in the two alloys is found in Table 3. The four major contributing elements are carbon, manganese, silicon and molybdenum. The minor contributing elements are chromium, copper, magnesium, nickel and titanium.

2.3.1 Major contributing elements

Carbon is considered due to its major role in defining the alloy on the phase diagram. The amount of carbon present in both alloys dictate that they be defined as cast iron [4]. Carbon will promote graphitization during solidification, and can increase the hardness of an alloy as well as its brittleness [16]. After carbon, silicon is the most important element in a cast iron alloy. One of silicon's primary duties is to enable the carbon to come out of solution to form graphite. This graphite formation decreases the hardness of the alloy, reducing its strength and its density. In addition to causing the carbon to fall out of solution, silicon is

also used to contribute to the heat and oxidation resistance [17] and to increase the fluidity of the molten metal.

Manganese is added to the mix to counter the negative effects of sulfur, which when combined with iron forms iron sulfide, which has a negative effect on the graphitization process [18]. The presence of sulfur can also make the molten material difficult to pour, causing short runs in the casting. With the addition of the manganese to the mix a compound of manganese sulfide is created. This compound will float to the top of the molten solution and be removed with the slag, thereby reducing the amount of sulfur in the solution.

Molybdenum is the final major contributing element in the two alloys examined. Its major contributions are to increase the strength and creep resistance of the alloy at high temperature, as well as to aid in the corrosion resistance of the alloy [17].

2.3.2 Minor contributing elements

One of the more obvious effects of the contributing elements is from the element chromium. Chromium is added to reduce the effects of corrosion on the alloys. Chromium can also be added to the matrix to increase the high temperature stability of the matrix [19]. Nickel is often added along with the chromium to increase the hardenability as well as promote graphitization of the carbon [19]. Copper can be added to the matrix to help refine the graphite and to increase the fluidity of the molten mixture [18]. Another element that aids in the fluidity is titanium. Titanium is also used as a degasser and deoxidizer, aiding in

the corrosion resistance of the matrix [18]. Finally, magnesium is added to the matrix mainly as a spheroidizing agent to assist in the formation of carbon nodules [18].

Table 3. Table of Elemental Composition of Alloys – ***Bold Italics Underlined*** indicate major contributing elements, ***Bold*** highlights indicate minor contributing elements

Element	50HS Ave	HI Si Mo	Difference	Average	% Diff	Element
Fe	92.49889	91.48244	1.0164	91.9907	1.1049	Fe
<i><u>C2</u></i>	<i><u>2.885067</u></i>	<i><u>2.489733</u></i>	<i><u>0.3953</u></i>	<i><u>2.6874</u></i>	<i><u>14.7106</u></i>	<i><u>C2</u></i>
<i><u>Mn</u></i>	<i><u>0.259718</u></i>	<i><u>0.218413</u></i>	<i><u>0.0413</u></i>	<i><u>0.2391</u></i>	<i><u>17.2775</u></i>	<i><u>Mn</u></i>
P	0.025003	0.021412	0.0036	0.0232	15.4737	P
S	0.001649	0.004232	0.0026	0.0029	87.8674	S
<i><u>Si</u></i>	<i><u>3.642311</u></i>	<i><u>4.318778</u></i>	<i><u>0.6765</u></i>	<i><u>3.9805</u></i>	<i><u>16.9943</u></i>	<i><u>Si</u></i>
Ni2	<i><u>0.020093</u></i>	<i><u>0.021521</u></i>	<i><u>0.0014</u></i>	<i><u>0.0208</u></i>	<i><u>6.8630</u></i>	Ni2
Cr2	<i><u>0.048401</u></i>	<i><u>0.037504</u></i>	<i><u>0.0109</u></i>	<i><u>0.0430</u></i>	<i><u>25.3702</u></i>	Cr2
<i><u>Mo</u></i>	<i><u>0.421067</u></i>	<i><u>1.106311</u></i>	<i><u>0.6852</u></i>	<i><u>0.7637</u></i>	<i><u>89.7282</u></i>	<i><u>Mo</u></i>
Cu2	<i><u>0.084104</u></i>	<i><u>0.120533</u></i>	<i><u>0.0364</u></i>	<i><u>0.1023</u></i>	<i><u>35.6043</u></i>	Cu2
<i><u>V</u></i>	<i><u>0.001992</u></i>	<i><u>0.003311</u></i>	<i><u>0.0013</u></i>	<i><u>0.0027</u></i>	<i><u>49.7393</u></i>	<i><u>V</u></i>
Ti	<i><u>0.029339</u></i>	<i><u>0.033519</u></i>	<i><u>0.0042</u></i>	<i><u>0.0314</u></i>	<i><u>13.2998</u></i>	Ti
Co	0.010292	0.012115	0.0018	0.0112	16.2746	Co
<i><u>Mg</u></i>	<i><u>0.02638</u></i>	<i><u>0.046682</u></i>	<i><u>0.0203</u></i>	<i><u>0.0365</u></i>	<i><u>55.5758</u></i>	<i><u>Mg</u></i>
Al2	0.013441	0.031092	0.0177	0.0223	79.2722	Al2
B	0.000802	0.001223	0.0004	0.0010	41.5216	B
Nb	0.008525	0.010534	0.0020	0.0095	21.0816	Nb
Pb	0.000248	0.00118	0.0009	0.0007	130.6297	Pb
Sn	0	0	0.0000	0.0000	0.0000	Sn
W	0.011518	0.01622	0.0047	0.0139	33.8986	W
Zr	0.002802	0.004323	0.0015	0.0036	42.6974	Zr

2.4 Oxidation and scale formation

The contributions to corrosion prevention and, thus, oxide (or scale) formation appears to be very dependent on the characteristics of the elements present. A large amount of literature shows that the high-temperature oxidation

behavior of chromia (Cr_2O_3)-forming alloys, such as certain cast iron alloys, is significantly influenced by the presence of silicon additions, particularly under thermal cycling conditions. Silica (SiO_2) is thermodynamically more stable than chromia and so the former will consequently tend to form beneath or at the alloy/ Cr_2O_3 -scale interface. The formation of a continuous inner silica layer tends to improve isothermal oxidation resistance by reducing the amount of cation transport through the Cr_2O_3 scale and thus reducing the rate of Cr_2O_3 -scale growth; however, an inner SiO_2 layer can also greatly worsen the extent of scale spallation [20-29]. Evans et al. [20] tested a series of 20Cr-25Ni stainless steels with 0.05-2.35 wt.% silicon in a CO_2 -based atmosphere at 850 °C and found that the extent of scale spallation increases with Si content above about 0.92 wt%. Some studies [27-29] reported that the silica layer formed at the chromia/alloy interface is vitreous. Two features of vitreous silica are a low defect concentration and a lack of grain boundaries, both of which would contribute to low rates of diffusion. As a result, vitreous silica can act as an excellent diffusion barrier. The combined effect of Si in the alloy and H_2O in the reacting atmosphere presents further complications that are presently neither well documented nor understood.

Previous studies [30-32] have also shown that silicon facilitates the formation of a chromia scale. For example, Kumar and Douglass [30] studied the oxidation behavior of austenitic Fe-14Cr-14Ni steels containing up to 4 wt.% Si over the temperature range 900-1100 °C in air. The alloy without Si addition formed a scale comprised of Fe- and Ni-rich oxides and internal precipitates of spinel oxides, while a continuous chromia layer formed above a silica layer for

the alloy with 4 wt.% Si. According to Stott *et al.* [21], the formation of silica precipitates during the early stages of oxidation facilitates the development of a Cr_2O_3 scale on an Fe-14Cr- 10Si alloy oxidized at 1000 °C. The continuous inner silica scale layer that eventually developed on this alloy improved isothermal oxidation resistance compared to Fe-26Cr-1Si and Fe-14Cr-3Si alloys, but did result in more extensive scale spallation on cooling. Clearly, the presence of Si in the alloy can be beneficial, but practical guidance of optimum levels is presently not available.

The addition of even very small concentrations of alloying elements to iron can significantly affect oxidation rates. For example, depending on the oxidation temperature, silicon in steels can have either a protective or accelerating influence on oxidation rates. The silicon can react at high temperatures to form either SiO_2 or fayalite (Fe_2SiO_4). Thermally grown fayalite has been reported to be extremely fragile and to exhibit weak adhesion to the steel substrate [33]. However, a continuous layer of fayalite is also known to provide protection against oxidation, by suppressing iron diffusion [33, 34]. Logani and Smeltzer [34] suggested that a protective layer of fayalite forms only if the silicon content in the steel is greater than 1.5 wt.%. In the event of scale separation, a non-protective inner-scale layer composed of a $\text{FeO}+\text{Fe}_2\text{SiO}_4$ mixture interspersed with bands of Fe_2SiO_4 will tend to form.

The combinations of oxidants present in a combustion gas (O_2 , CO_2 and H_2O) can also give rise to complex interactions with the growing scale. For example, the addition of water vapor to oxygen affects scale-metal adhesion

during iron oxide scale growth [33, 35] and changes mass transport within porous scales [36]. Very few studies of steel oxidation in combustion gas environments have been reported [37-39] and no systematic investigation appears to have been undertaken.

2.5 Oxide (scale) defects

Oxides are formed to provide a protective layer of the surface of their parent material. When this protective layer is damaged, problems can arise which can lead to further oxidation and result in material loss. These problems may arise from some sort of impact on the surface, some sort of mechanical stress, or they may occur as a result of thermal cycling where repeated expansion and contraction occur. When mechanical failure of the oxide layer occurs it is usually the result of three general factors; defects, stresses and stress reliefs [40]. Defects may be defined as porosity, voids or micro cracks [41-45]. Stresses may be the result of thermal cycling or the production of the oxide layer itself. The stress relief refers to the layer in between the oxide layer and the sub-structure [46]. How the scale will fail is determined by the interaction of the above mentioned factors.

The oxidation failure of cast iron is typically thought of as being the result of porosity. The formation of porosity on cast iron is typically due to the higher rates of oxidation associated with the presence of water vapor. Tuck et al. [47] observed that the formation of the scale can be associated also with the geometry of the specimen as well. It was observed that on curved shapes the

scale tended to be more porous, whereas on flat specimens the oxidation tended to be more compacted. When pores form, they generally develop at the metal/scale interface as a result of iron vacancies by cation transport. Rahmel and Tobolski [48] and Tuck et al. [47] maintain that there is continued contact between the scale and the metal regardless of the vacancies as a result of plasticity of the scale itself. This plasticity of the oxide and vacancy at the metal/scale interface allow for not only porosity but micro channeling as well. With the mention of porosity and micro channels, it is necessary to mention a few of the reactive gasses and their characteristics:

H – a nonpolar molecule with low polarability and weak donor/acceptor properties

H₂O – a large dipole moment and lone pair electrons which therefore makes it a good donor. Absorption into the scale matrix occurs by an acid/base interaction with the metal ions.

CO – a very weak donor even though it has a lone pair of electrons

CO₂ – can act as either a weak donor or acceptor

O₂ – a very powerful donor or acceptor which can be reduced in multiple ways

Metals with a high reactivity such as iron can generate active sites for the development of scale, particularly at higher temperatures. The plasticity of the oxide at these higher temperatures increase the transport of cations and anions, which may help how/why explain H₂O and O₂ increase the oxidation rate of silicon [49, 47].

2.6 Oxide (scale) stress

Generally speaking, there are only four main types of stress concerned with oxide or scale. The most important type of stress, as mentioned before, is

thermal stress, σ_{th} , which comes from thermal cycling. Thermal stress arises due to differences in thermal expansion coefficients between the metal substrate and the oxide. The cooling of the mated materials typically results in a compressive stress. There is one exception to this typical compressive stress condition, which is the development of a tensile stress that can occur when a multilayered type of oxide forms. Growth stress, σ_{gro} , is the result of a difference between molar volumes that can occur between the oxide and the metal. Typically the oxide volume is larger, and the ratio between the oxide and the metal is known as the Pilling-Bedworth ratio [49]. Although compressive stresses are typically considered, there is a type of stress that can develop during the phase changes of oxidation. This type of stress is known as transformational stress, σ_{trans} . When looking at iron based alloys, the transformation of magnetite to hematite can occur when porosity or voids are created in the scale which can result in a compressive stress [50, 51]. As also mentioned above, the shape of the specimen can have an effect on the total stress of the system. Geometric stress, σ_{geo} , is related to the location for the development to the scale. Depending on whether the shape is convex or concave, either tensile or compressive stress may result. The last type of stress that must be considered is the type of stress that is applied to the system overall. System applied stress, σ_{app} , is the direct result of stress applied from the outside. The total stress applied to the oxide scale, σ_{tot} , is an accumulation of the above mentioned stresses.

$$\sigma_{tot} = \sigma_{th} + \sigma_{gro} + \sigma_{trans} + \sigma_{geo} + \sigma_{app} \quad (1)$$

2.7 Failure mechanisms

The failure of cast iron in the application of exhaust manifolds is typically the result of thermal fatigue. Thermal fatigue failure is a result of two conditions: a temperature variance, and some type of mechanical constraint. The thermal variance, i.e., expansion and contraction caused during periods of acceleration and deceleration and during the warm up and cool down phase of operation [52] results in thermal stress. At high temperature there is also the matter of oxidation, which can add several additional components to the fatigue process. Thus, the primary properties of a material required for such operations are; resistance to oxidation, structural stability and strength with resistance to the thermal cycling [53].

There are several ways to identify thermal fatigue stress; by the multiple initiation sites that join in random motion to form the main crack, transgranular fracture, an oxide wedge filling the crack, and transverse fractures [54]. Cracks that are formed as a result of thermal stress typically run parallel to one another. Failure due to these types of thermal fatigue can occur when, at higher temperatures, oxygen may penetrate near the grain boundaries and cause a general weakening of the microstructure and mechanical cycling.

Fatigue life consists of two distinct periods, namely, time to initiation plus time of propagation. Surface finish and / or the presence of flaws greatly decreases the amount of time required for crack initiation. In cast irons it appears that defects (cracks) leading to failure form from two ways – the first is

from the surface thru failure in the oxide scale that forms during operation, either by spalling to expose the surface or by micro-cracking and micro-tunnels in the scale [41-45]. A second failure mechanism noted in ductile cast irons occurs when the graphite nodules near the surface shrink during operation, creating micro cracks that result from the voids created by shrinkage. Since both mechanisms can occur rapidly during service in a thermal cycling environment one must therefore assume that the fatigue life and limit are mainly controlled by crack propagation laws and by the threshold stress intensity factor [55, 56].

There are three items we must bear in mind when considering fatigue and failure of nodular cast iron: the size of the nodule which may become a fracture origin, the microstructure (especially hardness) near the fracture origin, and the stress applied at the fracture origin. Of these three the primary factor appears to be the interaction of the nodules with the matrix microstructure, which is comprised of both pearlite and ferrite. In typical nodular cast irons the amount of pearlite present is kept to approximately ten percent or less. However, in production of exhaust manifolds, that percent is increased to approximately twenty five percent [57]. This is because pearlite has a higher strength and hardness than ferrite, however, it is more prone to brittle failure than the soft and ductile ferrite [58].

The formation of the graphite nodules is a key factor in the matrix of the material, proving critical to the strength provided by the matrix. In fatigue the size, shape and distribution of the nodules play a role in crack initiation and propagation, but does not have a significant role in the cyclic hardening of the

material. Spheroidal graphite (most desirable) is formed during the cooling process, crystallizing from the melt during manufacturing. The crystallization is controlled by the diffusion of carbon through the matrix. The rate of diffusion may decrease with an increase of the size of the mold. The larger the thickness the lower the cooling rate, which can result in a lower nodule count, which has been seen to translate to a lowering of the fatigue strength [59, 60]. This is because as the cooling rate decreases there is a greater likelihood for the nodules to deviate from the ideal spherical shape in order to adjust the mass balance of carbon during the solidification.

As the nodules stray from the spherical shape there is a greater contribution to crack formation as a result of the lower ductility and strength [61, 62]. In addition, the shape of the nodule can act as an indicator of the internal notch effect, which can have a strong influence on the fatigue behavior of the material [63-67]. For example, with a spherical nodular shape if the graphite were to pull away or de-bond from the matrix due to shrinkage or plastic strain the voids created by this de-bonding create weak points [68]. A weak point that is spherical in shape is less susceptible to crack initiation and may act similarly to a stop-drilled-hole used to arrest crack growth in materials. However, in thicker walled (>100 mm) castings there is a much greater tendency to deviate away from the desired spherical nodule to other, less desirable shapes such as chunky, spikey, coral, or other irregular shapes [69]. When the shape is not spherical, but perhaps chunky, similar shrinkage of the nodule away from the wall produces a sharper void, increasing stress concentration. Another issue related

to non-spherical nodules is a decrease in nodularity count and decreases the mechanical properties around the irregular shaped formations. The end result is that the material can be expected to have a lower strength overall, specifically a lower ultimate tensile strength and elongation to failure [59, 70, 71].

Since cooling rate plays an important role in the development of the microstructure, and can affect the shape and number of graphite nodules present in the matrix, one must consider the possibility that there may be different strengths and properties in cast molds of varying thicknesses. Studies have shown [72] that smaller spherical graphite nodules in higher numbers decrease the crack propagation rate as compared to larger or irregularly shaped nodules. In considering the effects of smaller defects, it is thought that the fatigue strength is determined by the maximum size of the nodule, whether individually, or in instances of coalescing nodules. In either case, the finer microstructure results in a minimization of the number of initiated cracks as well as a reduction in the propagation rate.

Cooling rate is important to the strength and, ultimately, the failure of the material in ways other than the effect on nodule formation since the formation of ferrite and pearlite also are determined during this process. An increase in cooling rate increases the rate of pearlite formation. The need for the greater formation of ferrite than pearlite is that ferrite is more stable at higher temperatures than pearlite.

As mentioned in Sections 2.5 and 2.6, the addition or subtraction of specific elements can play a key role in the development of the matrix. Magnesium and silicon are often added to promote formation of nodules. Additionally, elements such as nickel and copper may also be added to the matrix to aid in the formation of nodules, especially in thicker castings where larger or irregularly shaped nodules are more likely to form. In addition to increasing fluidity and promoting the formation of graphite nodules, Silicon performs an additional role by promoting development of a condensed Fe_2SiO_4 layer inside the FeO layer formed at the surface [57]. This layer aids in the prohibition of crack initiation at higher temperatures. The addition of molybdenum, again mentioned earlier, is important to the resistance to failure in that it helps resist creep and improves stress rupture strength at high temperature by the formation of Mo rich carbides which form along grain boundaries, and are stable at higher temperatures [57, 73, 74]. These rich carbides are distributed in the pearlite phase of the microstructure.

2.8 Fatigue crack growth approaches for cast iron

The modeling of fatigue damage can be traced back to the 1920's and 30's, when it was first recognized that damage increases with applied loads in a cumulative manner. It is the accumulation of fatigue damage that plays an important role in the life prediction theory. Since that time assessing damage accumulation and modeling of that damage has received great interest. From those early beginnings until the 1970's, theories that were developed had a phenomenological approach, and were based on three basic concepts; linear

summation, change in endurance limits, and the crack growth based approach. The phenomenological approach attempted to improve on the linear damage rule, and as a result many theories were developed. These theories can be divided into five major groupings; the damage curve approach, the S-N curve modification approach, the two stage damage approach, and the crack growth approach. Over the years since its first inception and acceptance, there have been over 50 fatigue damage models that have been developed. A table of the major theories on fatigue [75], along with pertinent information and nomenclature can be found in Appendix A as Tables (A1) through (A8).

There are but a few papers related to the topic of high temperature of cast iron at the time that this literature review was conducted. At the time of this writing the author only found six relevant articles. A brief description of the models and the work dealing with the fatigue of cast iron are described here. Li Chang et al., carried out work based on the concepts of thermal conduction equations, where the three-dimensional (3D) temperature field of a work roll was investigated using finite element method (FEM) [76]. Costa et al., studied the importance of the role of geometrical features such as shape, size, and relative position of either casting defects as well as graphite nodules have on the definition of the fatigue limit [77]. Seifert and Riedel developed a strategy to efficiently identify the model parameters based on isothermal experiments [78]. Damir et al., studied the response of modal parameters (damping ratio, natural frequency, and FRF magnitude) to variations in material microstructure, as a main factor affecting fatigue life [79]. Germann et al. developed fatigue life

prediction methods to calculate Woehler curves for probabilities of failure [80]. Metzger et al. developed a model based on crack growth due to low frequency loading (thermomechanical and low cycle fatigue) and due to high cycle fatigue [81].

In looking at the existing fatigue damage models, they could be classified into six basic categories:

1. Linear damage evaluation and linear summation – the issues with LDR's is that they cannot account for either the load sequence or the effects of interactions due to their linear nature [82].
2. Nonlinear damage curves and two stage linear approaches – in this category the damage process is broken down into two stages – crack initiation and crack propagation [83].
3. Life curve modifications to account for load interactions – these modifications are load dependent and are based on modification of the material S-N curves [84, 85].
4. Crack growth based approaches – this approach has gotten wide-spread acceptance given that they can be directly related to the physics of the of the damage process [86].
5. Continuum damage mechanics based approaches - these approaches are based on a relatively new approach of modeling the damage process at the continuum level [87].
6. Energy based models – here the models are based on the concept of unifying damage caused by different types of loading such as creep, fatigue and thermal loading [88].

Although each of these six different categories contains merit, they are only capable of accounting for one, or at the most several, of the phenomenological factors. For some of these approaches, there is no real boundary or distinction between models or theories. This can create problems when trying to fit data to a particular model. Additionally, due to the complex nature of fatigue, there is no one model that encompasses all of the different aspects of the problem. One of the most common type models employs an

integration of the Paris –type crack growth rate equations, with modifications adapted to account for the effects of interaction factors and load ratios.

There are three equations that are typically best for describing the behavior of low cycle fatigue behavior. They are the Coffin – Manson equation (2) which is one of the more common methods for the analysis of fatigue data, and can be used to examine the relationship between the applied strain and the fatigue life [89].

$$\frac{\Delta\varepsilon_p}{2} = \varepsilon'_f (2N_f)^c \quad (2)$$

Where

$\Delta\varepsilon_p$ is the cyclic plastic strain range
 N_f is the number of cycles to failure
 ε'_f is the fatigue ductility coefficient
 c is the fatigue ductility component

The other two equations used for the examination of fatigue data are the Basquin equation (3) which establishes a log-log relationship for SN curves, using Wöhler's test data.

$$\sigma_a = \frac{\Delta\varepsilon_e}{2} E = \sigma'_f (2N_f)^b \quad (3)$$

Where:

σ_a is the cyclic peak stress
 $\frac{\Delta\varepsilon_e}{2}$ is the cyclic strain amplitude
 E is Young's modulus
 σ'_f is the failure strength amplitude
 $2N_f$ is the number of strain reversals to failure (N_f equals the number of cycles to failure) and b is the fatigue strength exponent.

The last equation is the Hollomon equation (4) which is a power law relationship, relating stress and the amount of plastic strain [90-93]. The failure strain rate for this equation is represented by ε'_f and N_f is taken to be $\frac{1}{2}$.

$$\sigma_a = K' \left(\frac{\Delta \varepsilon_e}{2} \right)^{n'} \quad (4)$$

Where K' is the cyclic strain hardening coefficient and n' is the cyclic strain hardening exponent.

In recent years there is a new model type, adapted from the uniform material law, for high strength steel, referred to here as the Uniform Material Law for High Strength Steel (UMLHS) [94]. The equation for UMLHS is given below:

$$\varepsilon_a = (\sigma'_f)/E * (2N)^b + (\varepsilon'_f) * (2N)^c \quad (5)$$

Where;

ε_a is the strain amplitude
 (σ'_f) is the fatigue strength coefficient
 E is Young's modulus
 N is the number of cycles at endurance limit
 b is the fatigue strength exponent
 c the fatigue ductility exponent
 (ε'_f) is the fatigue ductility constant

This model provides an estimate for the endurance limit and the expected deviation between estimated and experimental data curves [94]. Although this newer model is a step in the right direction for fatigue, it does not address the application to cast iron. To resolve this issue, one adaption of the UML has been found that adapts the UMLHS to the material of cast iron and has been denoted

as the Universal Material Law for Cast Iron (UMLCI) [95]. In this model for the fatigue damage for cast iron, stress amplitudes, strain amplitudes and the relationship with the number of cycles is investigated. The work is validated by examining the experimental data with the estimations based on calculations. By taking into account the changes in material properties, such as ultimate tensile strength, UMLCI can be adaptable to different types of cast irons. By adapting the UMLHS to cast iron, certain modifications need to be carried out;

n' an empirically determined value is set to 0.1 instead of being a function of b/c

(σ_f') becomes a function of the ultimate tensile strength of the material.

(ε_f') becomes an empirically determined constant

The table below gives a comparison of the differences between UML, UMLHS and UMLCI [95].

Table 4. Comparison of UML, UMLHS and UMLCI

<i>UML</i>	<i>High-strength steel</i>	<i>Cast iron</i>
K'/Mpa	$\sigma_f'/(\varepsilon_f')^{n'}$	$\sigma_f'/(\varepsilon_f')^{n'}$
n'	b/c	0.1
σ_f'	$R_m *(1+ \Psi)$	1.34 * $R_m + 208$
ε_f'	0.58 * $\Psi + 0.01$	0.26
B	$-\log (\sigma_f'/ \sigma_E)/6$	$-\log (\sigma_f'/ \sigma_E)/6$
σ_E/Mpa	$R_m *(0.32+\Psi/6)$	0.4*R_m
c	-0.58	-0.7
N_E	500,000	1,000,000
Ψ	$0.5*\{\cos[\pi*(R_m-400)/2,200]+1\}$	

In the development of the ULMCI, a method of trial and error was used to determine the constants used in the calculations as in the fatigue ductility and endurance stress calculations.

2.9 Fatigue factors of cast iron at high temperature

Over the years a lot has been written about the benefits of the alloying elements to the matrix of cast irons (discussed earlier in this work), but there has been little work on the response of alloyed cast iron at high temperature fatigue. The Si-Mo addition alloys have been developed for many reasons, but automobile exhausts are one of the more common areas, where temperatures can reach 750 °C or higher in some instances.

Most studies found dealt with the temperatures ranging from room temperature (approximately 22 °C) to 800 or 900 °C. At these varied temperatures there has been a wide range of responses, which should not be surprising given the complex nature of cast iron and the different damage mechanisms which can cause failure, such as creep cavitation, transgranular fracture, fatigue crack nucleation and growth due to voids created by graphite, environmental attack and microstructural ageing (coarsening and reprecipitation) [96]. When fracture occurs at room temperature, the fracture surface is formed by the splitting of the ferrite matrix with the graphite nodules becoming detached. When the temperature is increased there are mechanisms operating below the surface that play a significant part in fatigue and eventual failure. At higher temperatures, both the yield strength and ultimate tensile strength can decrease dramatically, which in turn will allow for an increase in elongation of the material.

It was found in one study dealing with cast iron [97] that uniform elongation was not consistent with the sample above 800 °C. The increased temperature results in an increase in the thermally activated atoms, which will increase the vacancy concentration. Micro voids within the matrix will coalesce with voids created by the graphite nodules to form cracks. There is a decrease in the strength of the material at the grain boundaries, and the movement of the dislocations will also increase [98, 99]. Also, there is a transition from elastic to plastic strain at elevated temperatures. The softer material therefore means that the plastic strain will be a major factor in predicting the degradation behavior.

While the subsurface degradation is occurring, simultaneously there are defect mechanisms occurring at the surface where scale is formed [100,101]. At the surface a layer of $\text{FeO} + \text{Fe}_2\text{SiO}_4$ is typically formed near the base material of the specimen, and a layer of Fe_2O_3 is formed at the surface [102-106]. During cyclic loading, the scale can be continually cracked and oxygen can penetrate the scale where it progresses to the grain boundaries and a weakening of the material will develop into cracks. This repeated cracking and oxygen penetration is more straightforward at temperatures in the 600 °C range, but as temperatures near the 800 °C range, the scaling process becomes more complicated with severe oxidation.

As the temperature of the material increases, the amount of pearlite present will begin to change. At temperatures of 600 °C the amount of pearlite will look similar to that of room temperature amounts. Closer to 800 °C the amount of pearlite will diminish, decomposing into the matrix as either ferrite or

globular pearlite after long periods of temperature exposure [97]. During thermal cycling thermal stresses can arise due to the decomposition of pearlite into graphite, which can result in thermal expansion.

Microstructure was also studied by Canzar et al., who described that a higher fatigue life corresponded to smaller more regular shaped nodules [107]. Graphite nodules are usually thought of as defects which affect the fatigue behavior at the point of the graphite/matrix interface [108,109].

There are several reactions that can take place at high temperature, oxidation of the carbon can occur producing CO_2 , molybdenum carbides can form, and iron can be oxidized to form several different compounds of iron oxide. Because the carbon is smaller than the iron, it can move interstitially, allowing for fast movement through the matrix, particularly at temperatures around 800 °C. As temperatures increase in the range of 600 °C to 800 °C decarburization is more common than the oxidation of iron [110].

It was found from earlier studies that the addition of both molybdenum and silicon strengthen the cast iron by the molybdenum forming carbides and the silicon going into solid solution [102,103,111,112]. However, at higher temperatures the silicon may become soluble, thereby reducing the strength of the solid solution. Earlier in the paper a discussion was held on the benefit of silicon for the formation of oxide layers in high temperature fatigue, but one must bear in mind that silicon can act as either a protector or an accelerator of the oxidation rate. Tholence, et al. submitted that an amount of silicon over 4 weight

percent effectively reduces the formation of the oxide layer because of the presence of the FeSiO_4 layer [104-106].

When molybdenum is added into a cast iron alloy, at the higher fatigue temperatures, it can form carbides that locate at the grain boundaries. This collection of carbides can act as precipitate hardening at high temperatures, which increase its tensile strength, thermal fatigue life and creep resistance [104,105,112]. At elevated temperatures this effect can have the result of a buildup of precipitates at the carbide/matrix interface, which can result in crack initiation from brittleness [113]. Above the A1 temperature however, decomposition of the carbides may occur [114].

By increasing the temperature of the fatigue process, there are multiple factors that can affect the failure mechanisms, as mentioned above. As the temperature increases, failure mechanisms move from the brittle like failures to the ductile like due to the softening of the matrix, and the scale formation and eventual oxidation of the surface can lead to crack initiation and eventual failure.

2.10 Summary

With there being discussions on the coming of global warming and the increased demand for more efficient transportation, the demand for higher performing materials has been increasing at the same rate [115,116]. It has been discussed that the addition of certain elements to cast iron, specifically silicon and molybdenum, along with a host of several other “Major” elements and “Minor” elements, can contribute to the demand for better performance. Other

factors that can have an affect the on the performance of fatigue life are the casting temperature and the cooling rate of the cast.

The main damage to vehicles in service is the cyclic “thermal” or thermo-mechanical fatigue, along with high temperature oxidation of its components. The testing of these components for fatigue life is typically done in isothermal testing, which result in the conclusion that operation at high temperatures can result in the early generation of fatigue cracks. The art of high temperature testing has been conducted for about 140 years, while the art of high temperature, high strain fatigue testing has only been conducted for approximately the last 70 years [117]. The description of the factors that affect fatigue life of cast iron was described by Suresh et al. as being dependent upon the strength of the matrix, the strength of the defects, and the strength of the inclusion/matrix interface [118]. The use of S-N curves, initially devised by Wohler are often used for determining fatigue life. It was discussed by Murakami that the factor that makes it hard to predict fatigue life is the shape and size of the internal defects [119].

CHAPTER 3
EXPERIMENTAL PROCEDURES

Two different types of cast iron were received from an automobile manufacturer for this research project, both of which are used in the manufacturing of engine exhaust manifolds (Figure 7).

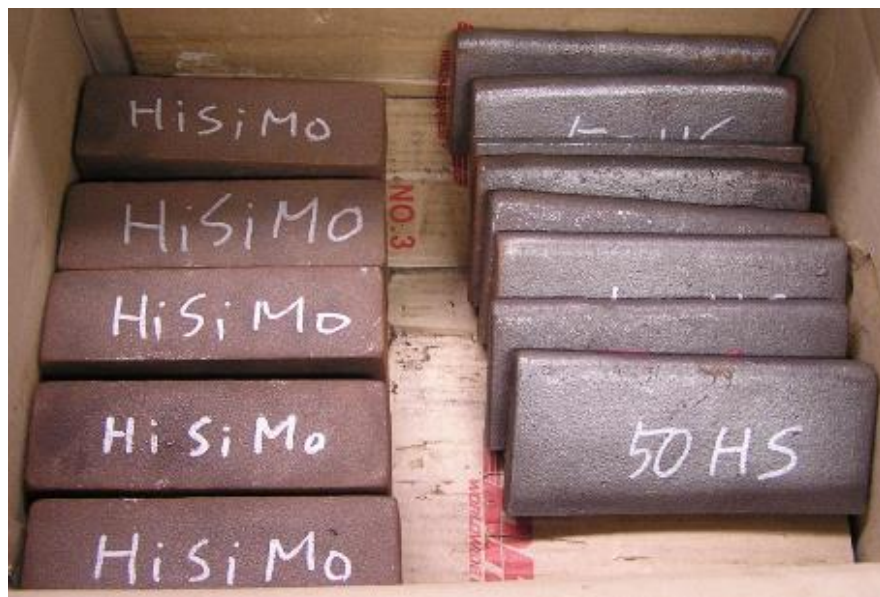


Figure 7. Samples as received in the shipping container. Samples were all keel sections from castings of the exhaust manifold.

The first type, referred to as 50HS, (meaning it is high in silicon), has traditionally been the more common type of cast iron used. The second alloy, HSM, (referring to the higher amounts of silicon and molybdenum), is a more recently developed type of cast iron. The received materials did not come with any composition information, only identification of the two alloy types.

3.1 Composition determination

The elemental composition of each alloy was verified using a LECO Glow Discharge Spectrometer (GDS) SA-2000, which uses an argon plasma to aid in the determination of the excitation energy of the constituent elements present and the results were shown in Table 3 (Chapter 2). The advantage to using a GDS over other methods such as an energy dispersive spectroscopy (EDS) in a Scanning Electron Microscope (SEM) is that it possess the capability to detect elements at lower atomic numbers, and provide a quantitative assessment of the sample. An image of the GDS sampled spot for each sample can be seen below in Figure 8. Samples prepared for the GDS were wet sanded to a 600 grit preparation prior to being placed into the instrument for testing.

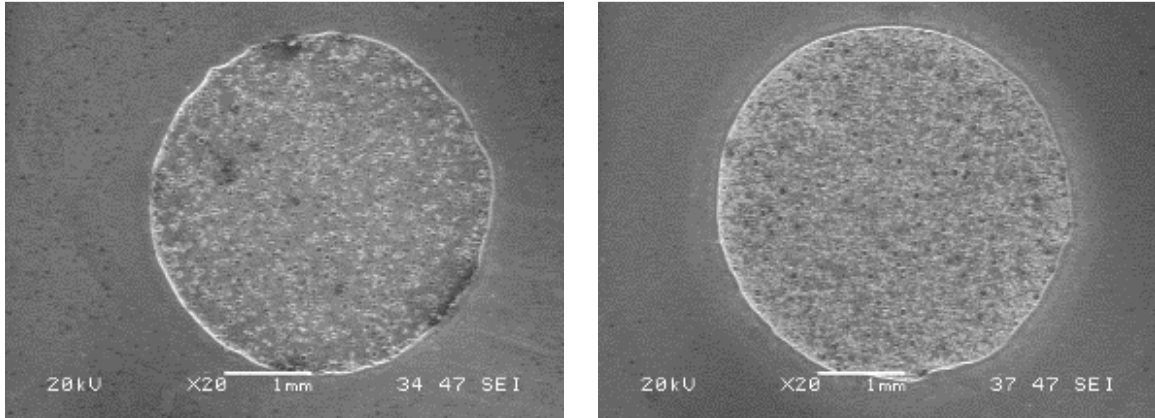


Figure 8. HSM (left) and 50HS (right) GDS spot taken in an SEM at 20X magnification

Although the composition of the alloys was not provided at the beginning of this work, no agreements of nondisclosure were required for this material.

3.2 Heat treatments

After composition was determined, two heat treatment experiments were conducted in order to determine how the materials reacted after being exposed to higher temperatures. Both the grain size and the protective (oxide) outer layer of the material were examined. Samples of each material were placed in a CM High Temperature Furnace, Model 1710 Gas Sealed, at progressively higher temperatures ranging from 600° to 900°C. The furnace uses silicon heating elements connected in series to generate the temperature inside the insulated chamber. An image of the furnace and the furnace controller is shown in Figure 9.



Figure 9. *CM High Temperature Furnace and controller*

To perform this experiment, small samples (< 1 in.³) were cut from larger blocks of each of the materials. The first experiment was conducted with a sample of each cast iron heated for 30 hours at temperatures of 700 °C, 800 °C,

and 900 °C, respectively. The second heat treatment required a sample of each alloy to be heat cycled at four different temperatures for 30 minutes. A total of six heat runs was performed. For both heat treatments, samples were placed in two different sections of the furnace. This was to confirm even heating throughout the oven in the event that there was a lack of heat conformity within the furnace itself. For the 30 hour heat treatment samples were labeled with either an “A” or a “B”, whereas for the cyclic heat treatments samples were labeled with either an “AA” or “BB”. All designations are shown below in Table 5.

Table 5. Designation of sample markings for the heat treatments

50HS	HSM	
600AA	600AA	Heat Cycle 30 min at temp w/a room temp cool in between
700AA	700AA	
800AA	800AA	
900AA	900AA	
600BB	600BB	
700BB	700BB	
800BB	800BB	
900BB	900BB	
700A	700A	30 Hour heat treat w/an oven cool afterwards
800A	800A	
900A	900A	
700B	700B	
800B	800B	
900B	900B	

For the 30 hour heat treatment, the furnace was turned off at the prescribed time and the samples were furnace cooled until room temperature was reached. For the 30 minute heat treating cycle, samples were heated in the

furnace at the preset temperature, and once the set temperature was achieved, the time commenced. At the end of the cycling time samples were removed from the furnace and allowed to air cool before being returned for another cycle.

3.3 Metallography

After all heat treatments were completed the samples were sectioned to examine the microstructure and scale. Samples were mounted in Bakelite using a LECO PR – 22 Pneumatic Mounting Press shown in Figure 10. After mounting, the samples were then polished with a Buehler Ecomet III Polisher/Grinder using the steps listed below:

- 60 grit Si-C paper, wet
- 120 grit Si-C paper, wet
- 240 grit Si-C paper, wet
- 400 grit Si-C paper, wet
- 600 grit Si-C paper, wet
- 1 micron diamond polish, Depti DP Blue Lubricant
- 1 micron alumina polish
- 0.3 micron alumina polish

Between each polishing step the samples were rinsed with water to avoid contamination in the next polishing step. Once polished, the samples were etched using a 2% nital solution for 150 seconds to reveal the grain structure of the material.



Figure 10. Mounting and polishing equipment

To examine the samples, images were taken at 200X and 500X magnifications using a Nikon Epihot 200 inverted metallurgical white light microscope (Figure 11).



Figure 11. Nikon inverted microscope

Grain size measurements were calculated using the Intercept Method per ASTM E112 – 96. Images were taken at 500X magnification for the different materials at each of the heat treatment temperatures. For this calculation, a scaling tool was created to compare the printed image size and the actual size to be measured. A scale for the 500X images was created using Image-Pro software, printed, and measured with a ruler for conversion. For these measurements a 12.3 cm line represented 0.00502 inches for the 500X images. To then measure the average grain size of the samples, one of these 12.3 cm lines was drawn at a random orientation on the image. The number of grains the line crossed was then counted (if the end of the line landed inside of a grain it was counted as $\frac{1}{2}$). To calculate the grain size 0.00502 was divided by the number of grains counted to get the average size in inches for that line. This was done three times per image and four images were used for each sample. These 12 sizes were then averaged to get an average grain size of the whole sample.

3.4 Ultrasonic testing

Ultrasonic velocity testing was done on the samples as they were received, without any heat treatment to determine initial materials properties by a nondestructive method. For the ultrasonic tests a Lecroy LT262 digital oscilloscope was paired with a Panametrics 5052 Pulser/Receiver. Two types of measurements were taken; a shear wave velocity measurement was made using a Panametrics V156 5 MHz, 0.25 inch diameter probe, and a longitudinal wave velocity measurement was made using a Panametrics V110 5 MHz, 0.25 inch diameter probe. The couplant for the transducer was Ultragel II for the

longitudinal measurement, and Panametrics shear wave couplant for the shear wave measurement, both of which are standard couplants used for ultrasonic testing. Figure 12 shows an image of the digital oscilloscope and pulser/receiver used in the velocity measurements.



Figure 12. *Digital Oscilloscope and Pulser/Receiver*

3.5 Hardness testing

Both alloys were tested for hardness in the “As Received” condition and after heat treating for the 30 hour timed test. The hardness testing machine was a Wilson Rockwell, Model 4YR Hardness Tester, shown in Figure 13. The samples were tested using the Rockwell B test, which employs a 1/8” spherical indenter and a load of 100 Kg.



Figure 13. *Wilson Rockwell Hardness Tester*

3.6 Tensile testing

Additional work needed for this research focused on the determination of the material properties of the individual alloys. In the first part of this work, tests were done to determine the yield strength using standard tensile tests in accordance with ASTM E 8M-04. The tensile tests were done on the two alloys used for this research. The tests were carried out using an Instron Model 5960 50 KN Dual Column Tabletop Testing Systems (Figure 14). The software used to control the load frame is supplied by the manufacturer and known as Bluehill® 3. The rate of speed of the crosshead during the testing was done at 0.01 inches per second until failure.



Figure 14. Instron 5969 Electromechanical Load Frame

3.7 High temperature fatigue testing

For the temperature fatigue work there were four sets of tests done on each of the two alloys. Each alloy was fatigued at room temperature (approximately 21 °C), 400 °C, 600 °C, and 700 °C for 100,000 cycles and at four Hertz. The number of cycles for the fatigue test was determined by a number of factors; frequency of the test – as allowed by the test conditions and the sensitivity of the machine, expected lifespan of the sample, and the amount of flexure from the sample at the set temperature. These parameters remained constant throughout the testing process, except for one sample, which broke around the 53,000 cycle mark. Samples were not fatigued to failure, as failure of the samples may have resulted in damage to the sensitive bend fixture. Each of

these tests were done in three point bend, with the determination of load calculations based on a simple spreadsheet interface written for fatigue work as seen in Figure 15 below.

Three Point Bending Calculations					
	Material x	Material Y	Material Z		
Width	1	1.034	1	<==User Input	
Thickness	0.5	1.031	0.5	<==User Input	
Span (in)	4	4	4	<==User Input "Determined by the machine"	
80% Yield (psi)	129120	112000	34400	<== Make sure to have correct Yield Value	
I=	0.0104	0.0944	0.0104		
Max Load	5380	20517	1433		
Min Load	538	2052	143		
Mean Load	-2959	-11284	-788	<==MTS Settings	
Amplitude	4842	18465	1290	<==MTS Settings	
R Ratio	0.1	0.1	0.1		
Mean Load	-13.1623	-50.1942	-3.5067	<==INSTRON Setting	MTS setting converted to kN
Amplitude	10.7691	41.0680	2.8691	<==INSTRON Setting	MTS setting converted to kN and then divided by 2

Figure 15. Example of user interface in determination of load settings

The user of the load frame inserts the sample’s dimensions and yield strength and the calculations within the spreadsheet provide the proper settings for the equipment. The determination of the settings for the load frames used are based on standard fatigue calculations and are shown below in Equations 6 thru 11.

$$I = \frac{bd^3}{12} \quad (6)$$

$$P_{max} = \frac{(4I)(0.8*Yield)}{L\frac{d}{2}} \quad (7)$$

$$P_{min} = P_{max}R \quad (8)$$

$$R = \frac{P_{min}}{P_{max}} \quad (9)$$

$$P_{mean} = -\left(\frac{P_{max} - P_{min}}{2}\right) \quad (10)$$

$$Amplitude = P_{max} - P_{min} \quad (11)$$

P = load at a given point, (N)

I = moment of inertia

L = Support span, (mm)

b = Width of test beam, (mm)

d = Depth of tested beam, (mm)

R = ratio of min to max load

The dimensions of the samples dictate the final settings for the fatigue test once the yield values have been determined by the tensile tests. Below is a representation of a fatigue sample used for this fatigue work, showing the dimensions used for calculations (Figure 16).

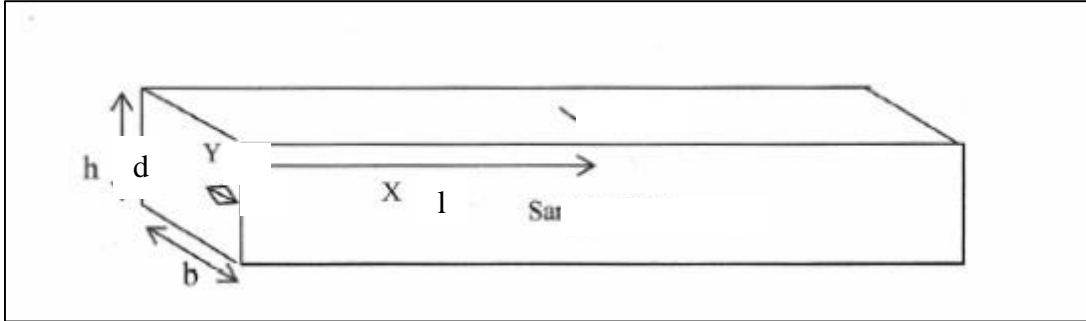


Figure 16. Drawing of 3 point bend specimen showing dimensions

To conduct the high temperature fatigue work, a system of equipment was assembled containing both a high temperature furnace and a load frame capable of fatigue testing. The furnace (mentioned in the heat treating section) is capable of achieving temperatures in excess of $900\text{ }^{\circ}\text{C}$, and is water cooled, not only around the jacket but at the point where the fatigue rods are to be placed (Figure 17). The furnace mount was designed to allow the furnace to slide in-between the vertical uprights of the load frame for fatigue work, as can be seen in Figure 18.

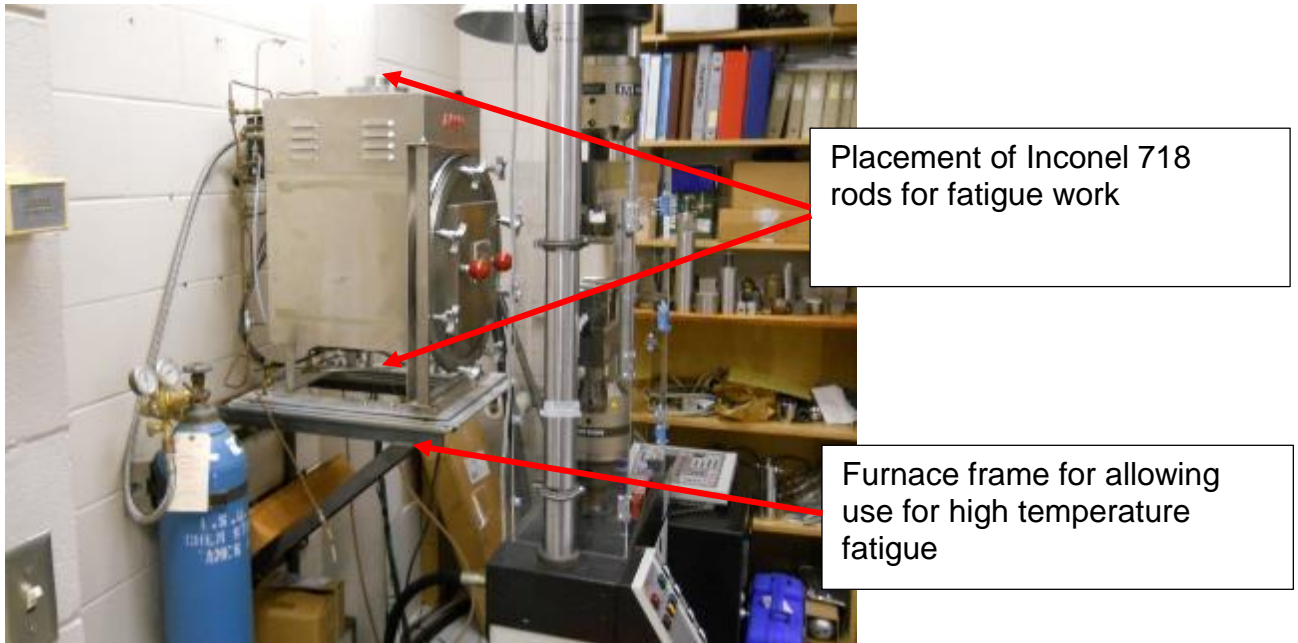


Figure 17. Features of high temperature furnace

In addition to these pieces of equipment, Inconel 718 rods (Figure 19) were machined to hold the three point bend fixture used for high temperature fatigue, which was made of Inconel 718 as well. Inconel 718 was chosen for this work due to its high strength and maximum allowable working temperature.

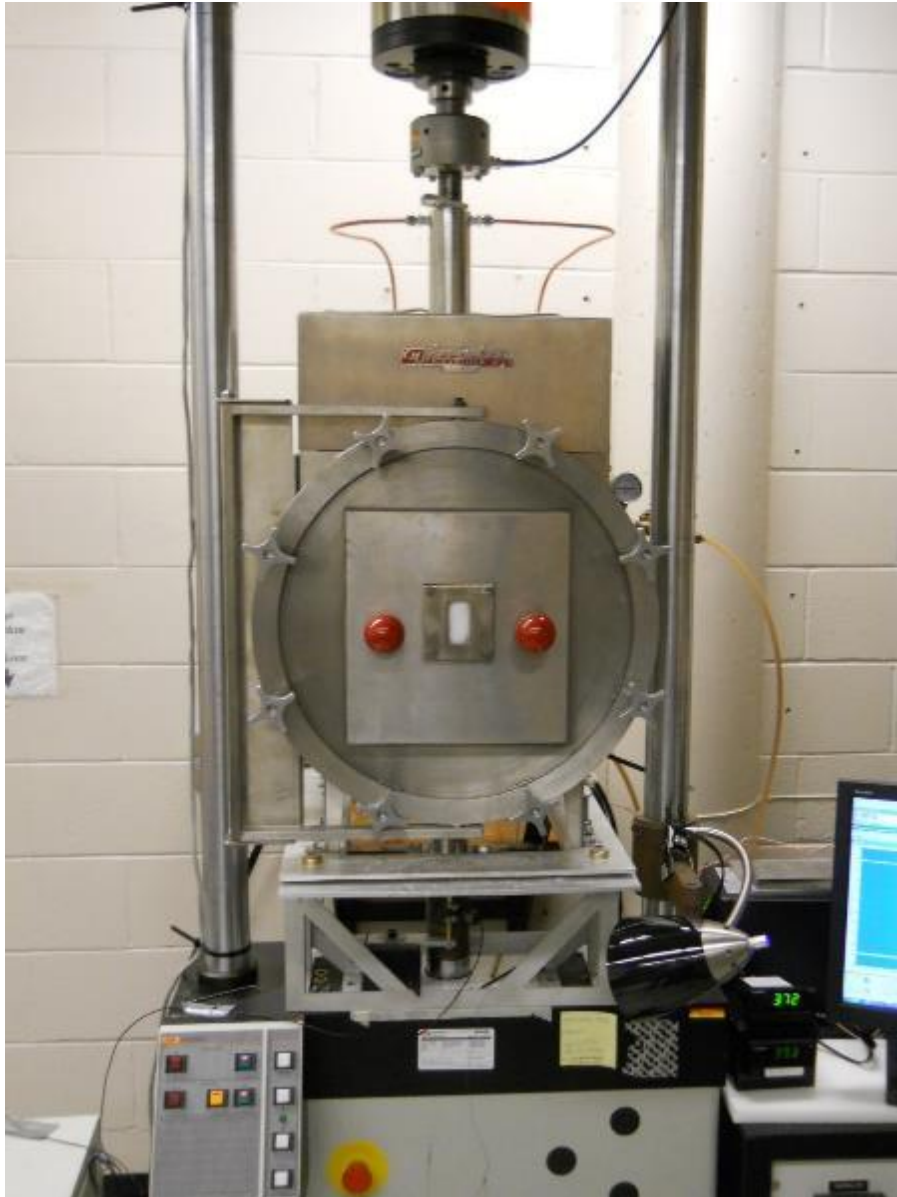


Figure 18. Image showing alignment of furnace with load frame

Initially it was thought to use Alumina rods, but with the long distance between the load cell and the actuator, precise alignment of the rods was of concern.



Figure 19. *Inconel 718 Rods and Water Jacket Fixture used to hold the rod*

Initial intent was to have the static portion of the bend fixture connected by a ball joint between the Inconel 718 rod and the Inconel 718 bend apparatus to allow for any slight misalignment, which might develop during the fatigue process and prove detrimental to the entire fixture if failure were to occur. After some initial testing it was found that the upper bend fixture had a tendency to rotate slightly if alignment of the samples was not absolute. This problem was resolved by notching each end of the rod by a dimension slightly larger than the bend fixture itself. As can be seen in Figure 20, with the notched rods in place, the bend fixture fits nicely into the set up.



Figure 20. Illustration of the bend fixture placed into the rods.

A close up image of the orientation of the fatigue sample within the three point bend Inconel 718 fixture is seen below in Figure 21, showing the upper and lower bend fixtures, the sample, and the rollers.

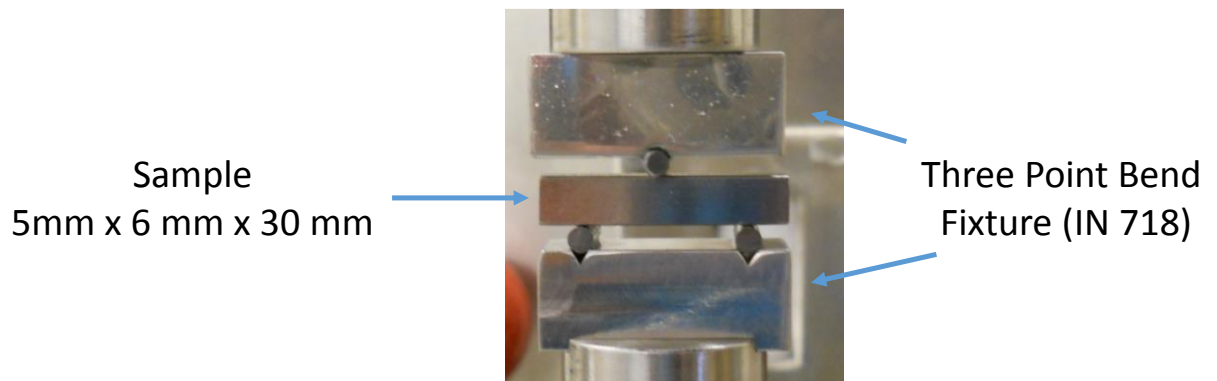


Figure 21. Image of three point bend fixture with sample in place

As an added measure to ensure alignment of the complete system and to try to ensure the best data possible, all of samples for a given alloy were made at

the same time. All were machined and wet ground to create even, parallel planes on the sides of the samples. A picture of the high temperature setup assembled outside of the furnace can be seen in Figure 22.

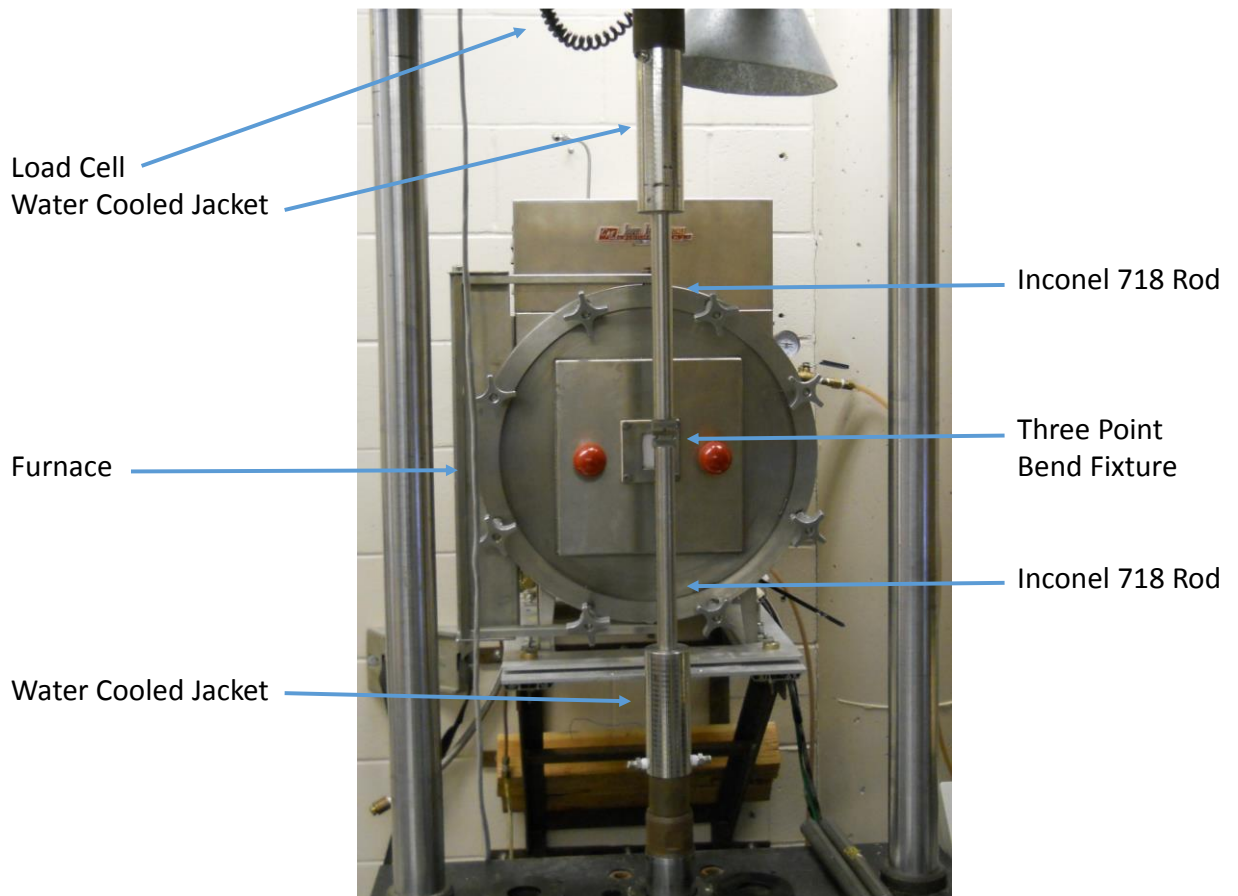


Figure 22. *Fatigue Process Equipment*

There were issues which delayed the commencement of the fatigue work, related to the sensitivity of the load cell to the small loads required (less than 600 pounds of compression) and to the sensitivity of the actuator given the displacement required to run the system in “Load Control”. In order to overcome the sensitivity of the load cell, a new, smaller capacity load cell was purchased, which had a maximum capacity of up to 1,124 pounds. To accurately measure

the displacement required for this work, an external extensometer was mounted to the outside of the furnace and attached to the actuator of the load frame, Figure 23.



Figure 23. External extensometer used for displacement recording.

The reason for the external extensometer was related to the size of the actuator piston (approximately 2.5 inches) and the displacement needed for load control operation (approximately 0.003 inches). Given the size of the load frame, the standard method of operation resulted in the noise of the system being equal to, or in some instances greater than, the sensitivity of the displacement. With the addition of the external extensometer, far greater accuracy was recorded for each of the tests.

An image of the entire setup, including the furnace, load frame and computer system is shown below in Figure 24.

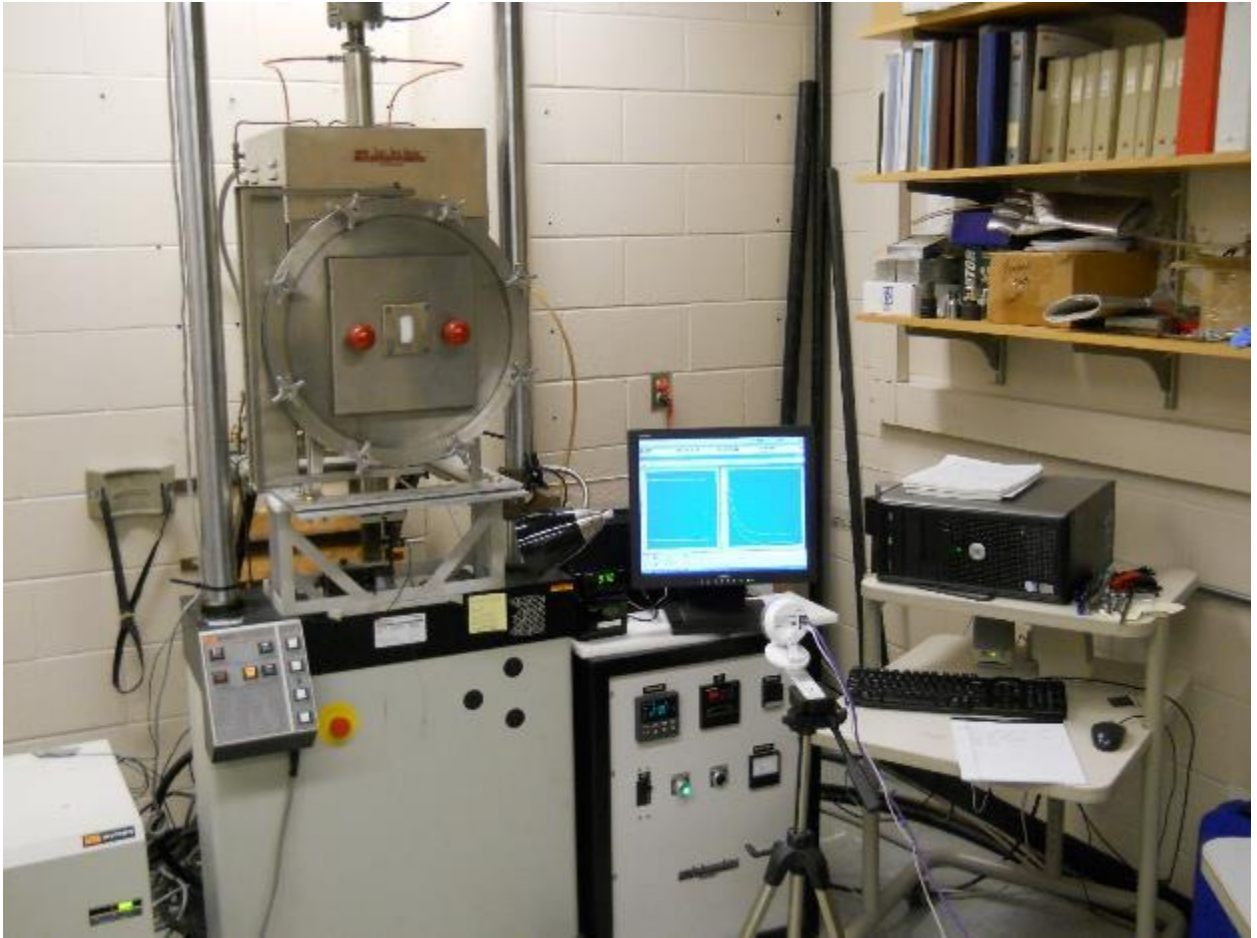


Figure 24. Image of the complete fatigue system while in operation

For each temperature test, a pre-load of approximately 20 pounds was placed onto the sample while the furnace was turned on and working temperature was achieved. This was done to ensure that contact remained with the rods and the bend fixture/sample during heat up. During preheating, the temperature was closely monitored to enable initiation of the fatigue test once the desired temperature was obtained. Once the temperature was obtained, the extensometer was set into position, and fatigue was initiated. The entire time for the preheating and fatigue testing varied by the operating temperature for the test. For the 400 °C tests the preheating time was approximately 30 minutes, for

the 600 °C tests the preheating time was approximately 1 hour, and for the 700 °C tests, the preheating time was approximately 1 hour and 20 minutes. The time for 100,000 cycles of fatigue at 4 Hertz is approximately 6 hours and 57 minutes. At the conclusion of the fatigue test, data was saved, the load was removed from the sample, and the furnace was turned off. The sample remained inside the furnace and were allowed to furnace cool overnight to room temperature.

CHAPTER 4

EXPERIMENTAL RESULTS

4.1 Composition determination

The determined composition of each alloy is shown tabulated in Table 6, and graphically in Figure 25. As expected by the name, the HSM alloy does contain greater amounts of silicon and molybdenum, and a lesser amount of carbon than the alloy 50HS.

Table 6. Composition of 50HS and HSM (wt %). The number 2 behind some of the elemental symbols refers to the second order wavelength used in emission spectroscopy

Name	Fe	<u>C2</u>	<u>Mn</u>	P	S	<u>Si</u>	<u>Ni2</u>	<u>Cr2</u>	<u>Mo</u>	<u>Cu2</u>
50HS Avg	92.49 9	2.885	0.260	0.025	0.00 2	3.64 2	0.02 0	0.048	0.42 1	0.08 4
HSM Av	91.48 2	2.490	0.218	0.021	0.00 4	4.31 9	0.02 2	0.038	1.10 6	0.12 1
Difference (HSM - 50HS)	-1.016	- 0.395	- 0.041	- 0.004	0.00 3	0.67 6	0.00 1	- 0.011	0.68 5	0.03 6

Name	<u>V</u>	Ti	Co	Mg	Al2	B	Nb	Pb	W	Zr
50HS Avg	0.002	0.029	0.010	0.026	0.01 3	0.00 1	0.00 9	0.000	0.01 2	0.00 3
HSM Av	0.003	0.034	0.012	0.047	0.03 1	0.00 1	0.01 1	0.001	0.01 6	0.00 4
Difference (HSM - 50HS)	0.001	0.004	0.002	0.020	0.01 8	0.00 0	0.00 2	0.001	0.00 5	0.00 2

As discussed in Chapter 2, elements can play either a major or minor role in determining the characteristic material properties of the cast alloy. Those elements shown in **Bold**, *Italics* and Underlined in the table above are considered major contributing elements, while those in **Bold** are considered to be

the minor contributing elements to the alloy. Those not highlighted may serve a role, but they were not considered in this work. The figure below shows the compositions of the two alloys, with the contributing elements listed above the x axes.

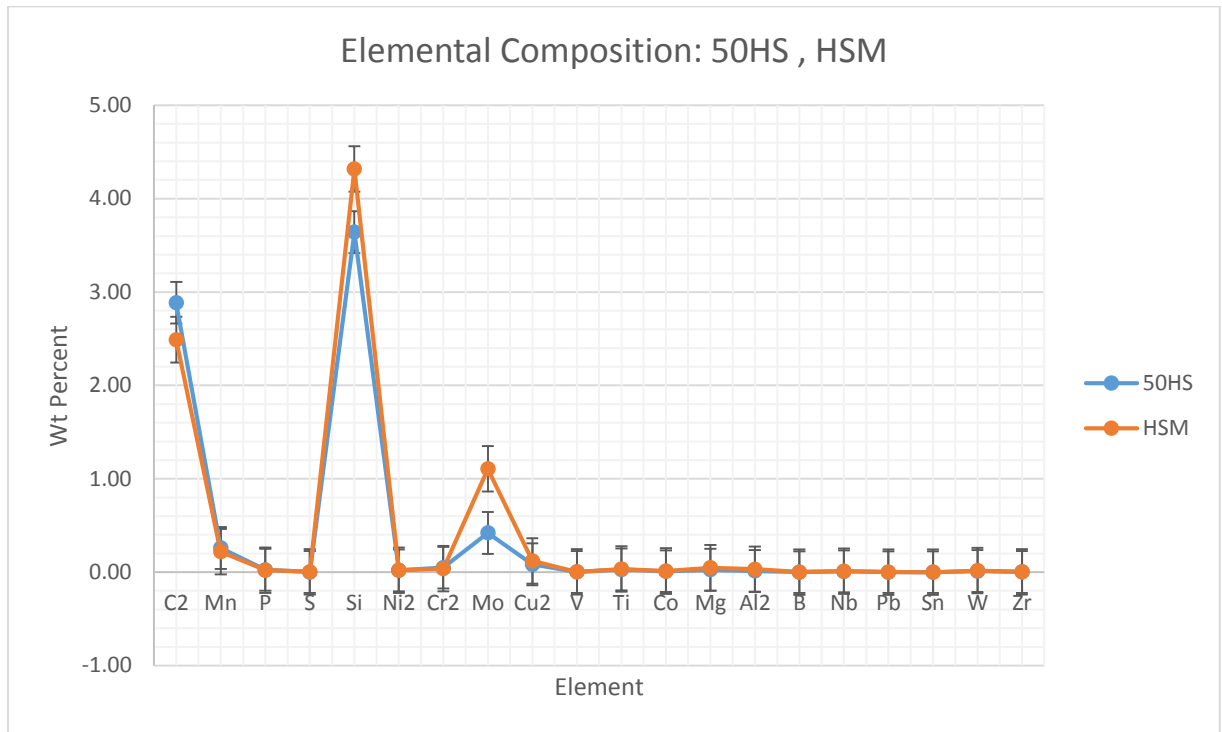


Figure 25. Composition of 50HS and HSM Alloys

The accuracy of the elemental values listed in Table 6 is somewhat questionable. Volatile elements like Mg, Al, Ca, Ce, La, etc. are very difficult to measure in the as-cast condition because the carbon is not in solution in the matrix as it is in standards used during the calibration of the GDS. Silicon is also an element that is difficult to measure for this same reason, but because it is more stable in the iron, by spark testing the same spot multiple times it is hoped that the value obtained from these as-cast samples is very close to what would

be obtained from running chill samples. To address the measurement difficulties and ensure the most accurate data possible, each alloy was sampled three times with 15 burns for each trial. With each burn the depth of the alloy is penetrated further, which allowed for a better sampling of the matrix. Once data from all 45 burns was gathered, an average of each element was determined.

4.2 Heat treatments

Two different types of heat treatments were conducted on the samples, a 30 hour at-temperature heat soak, and a 30 minute at-temperature cyclic treatment. Sample images are shown below, with the remaining images provided in Appendix A. Only those images showing the edge of the sample during the heat treatment are shown in this chapter. The nodularity across the sample did not change in any noticeable way across the sample width.

4.2.1 Room temperature results

Figure 26 shows the microstructures of both alloys taken at room temperature. In each sample one can see the three main constituents of ferrite, pearlite and graphite nodules. The nodules are primarily spherical, but there is some globularity (misshapen graphite nodules) present in both alloys. The noticeable difference between the two samples is the greater amount of pearlite present in the HSM sample, as can be seen on the right hand image of Figure 27.

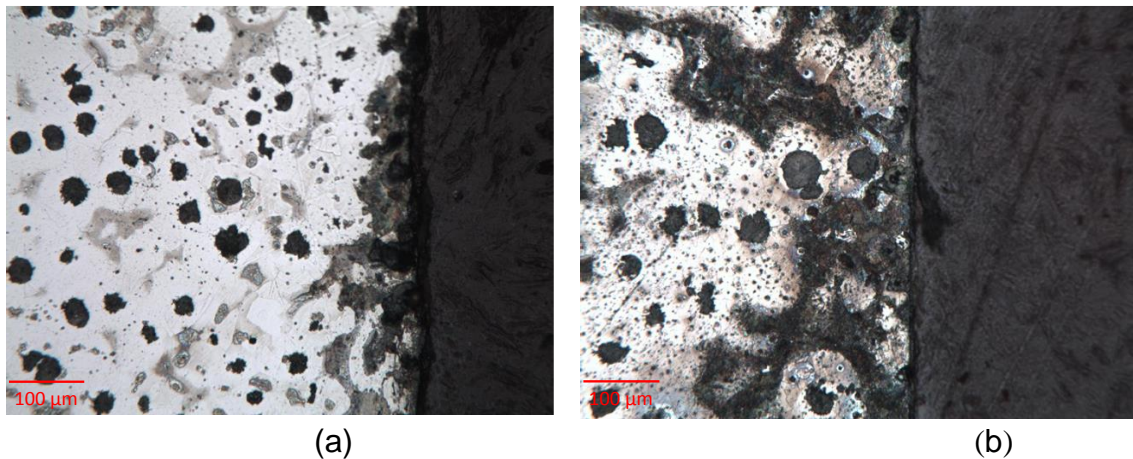


Figure 26. Images of sample edge at 200X of (a) 50HS and (b) HSM (without heat treatment)

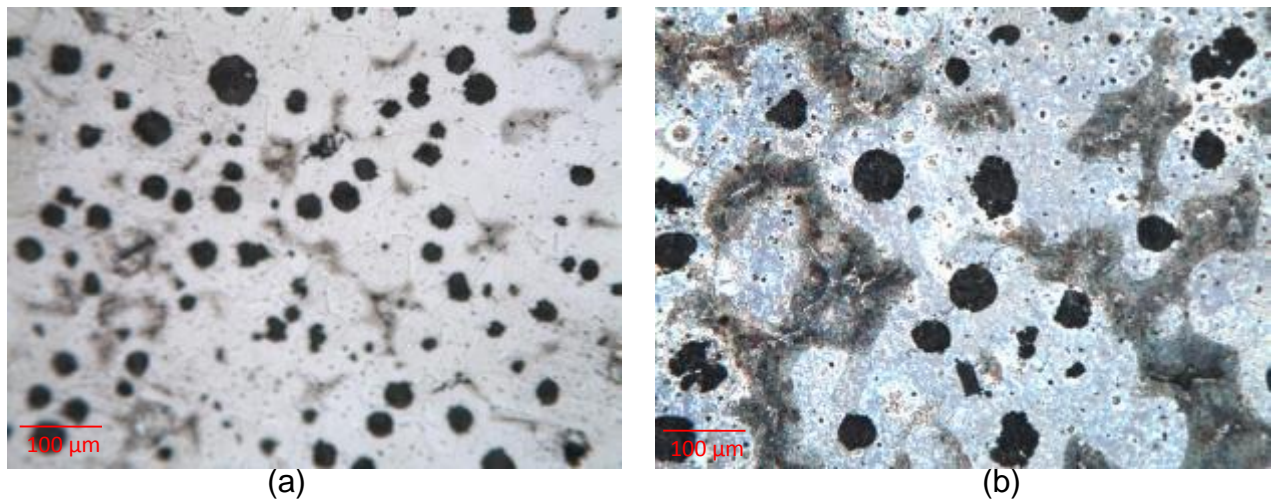


Figure 27. Images of sample center at 200X of (a) 50HS and (b) HSM without heat treatment

4.2.2 600 °C heat cycle results

Heat treatment at 600 °C consisted of repeated thermal cycling, where the samples were heated to 600 °C for 30 minutes, cooled to room temperature, then the process repeated six times. The primary difference between the two samples (Figure 28) appears to be the outer oxidation layer. While the thickness of the layer for either sample appears to be about the same, a difference in color is

evident, which may be due to etching effects. Both samples appear to have pearlite forming, and there is clear diffusion of carbon from the regions around the graphite nodules in both samples. The graphite nodules of the 50HS also appear to be changing shape from circular to more globular. Images taken from the center of the samples, (Figure 29) clearly show more pearlite than ferrite in the HSM sample.

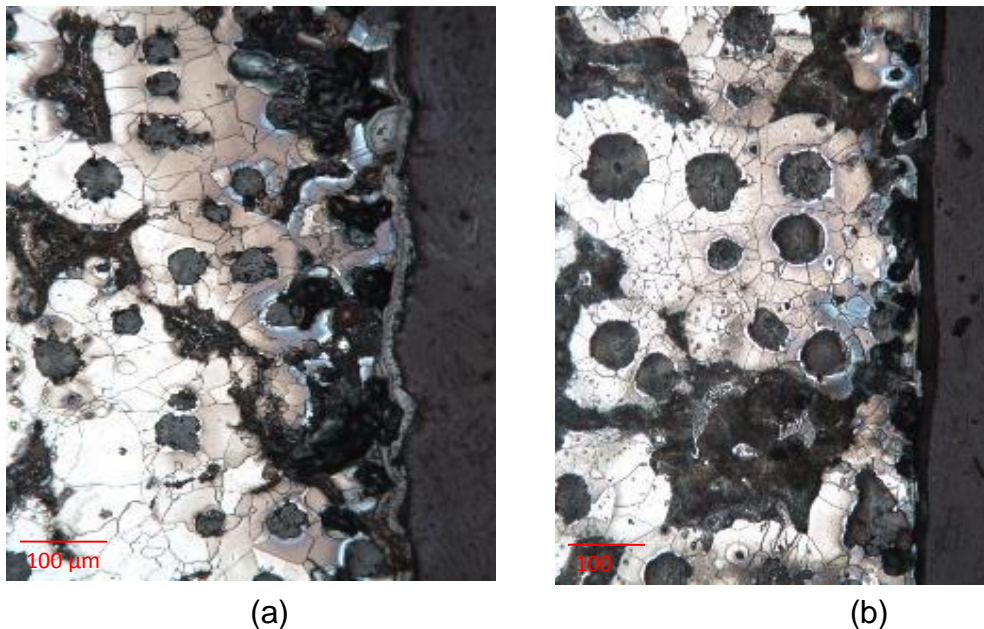
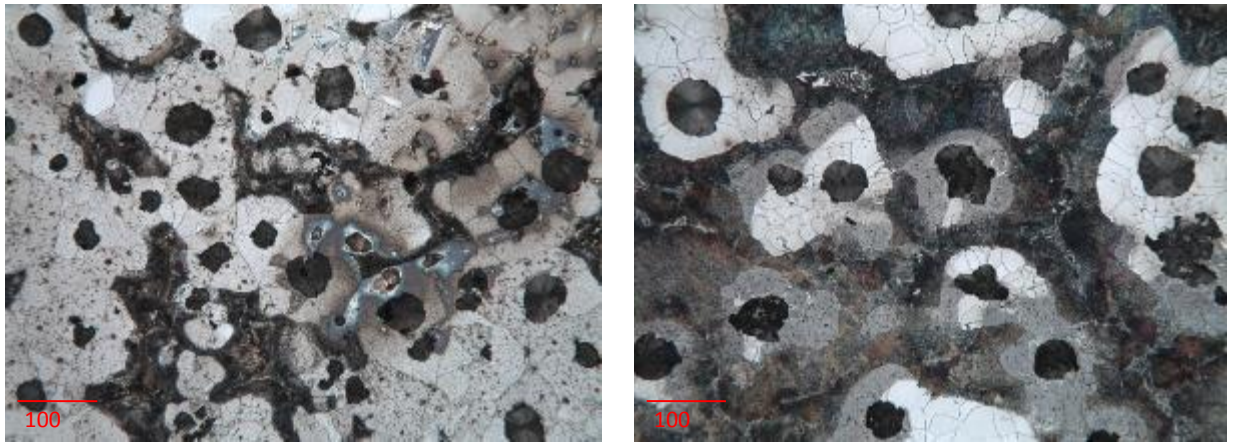


Figure 28. Images of sample edge at 200X of (a) 50HS and (b) HSM after 600 °C 30 minute heat treatment



(a) (b)
Figure 29. Images of sample center at 200X of (a) 50HS and (b) HSM with 600
°C
30 minute heat treatment

4.2.3 700 °C results

The 700 °C micrographs begin to show real differences in the two alloys. There is diffusion of carbon from the pearlite region surrounding the nodules to the nodules themselves, leaving ferrite surrounding the nodules occurring in the HSM sample. There is also a difference in the thickness of the oxide layer on the 50HS sample, as seen in Figure 30.

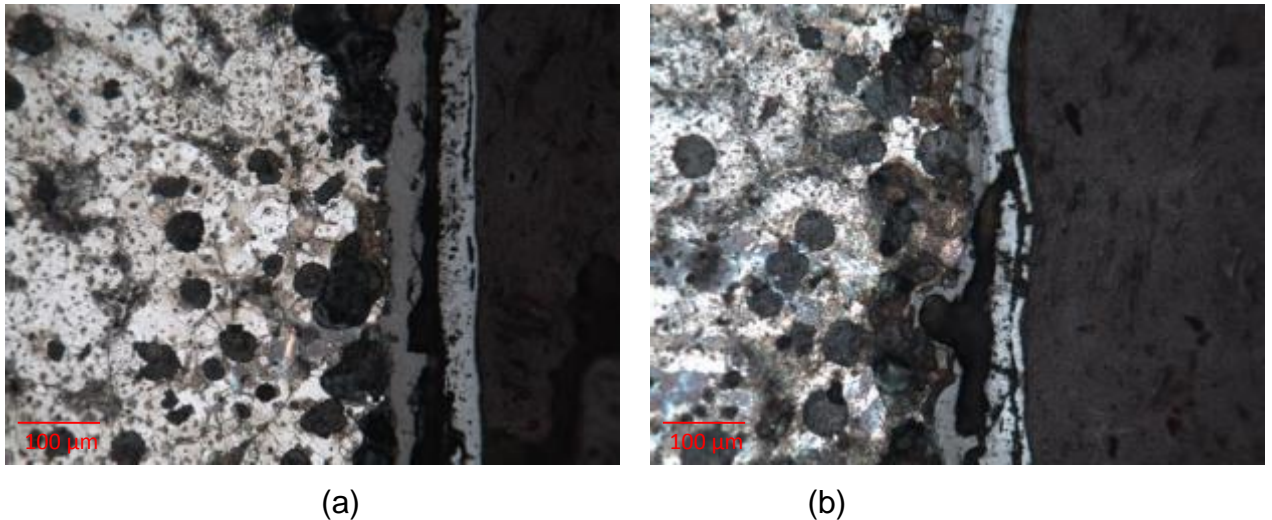


Figure 30. Images of sample edge at 200X of (a) 50HS and (b) HSM after 30 hour 700 °C heat treatment

The same increase in thickness of the oxide layer is evident in Figure 31 for the heat cycled samples. The diffusion of carbon seems to be greater in the 50HS sample.

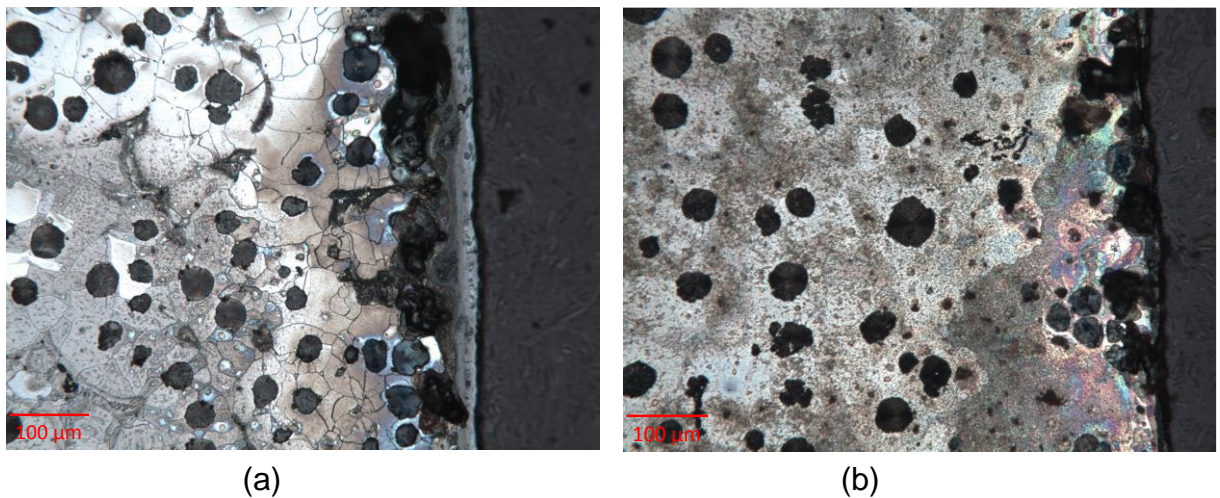


Figure 31. Images of sample edge at 200X of (a) 50HS and (b) HSM after 30 minutes at 700 °C heat treatment

4.2.4 800 °C results

At 800° C two significant differences are seen between the two alloys, Figures 32 and 33. First, as in the 700 °C samples, the oxide layer is much

thicker on the 50HS alloy than on the HSM alloy. The second difference is the number and size of nodules that appear near the surface of the two samples; the number of nodules in the HSM alloy appears greater in size than for the 50HS sample number but smaller in number. There also appears to be diffusion of carbon from the pearlite to the nodules, as in earlier heat treated samples.

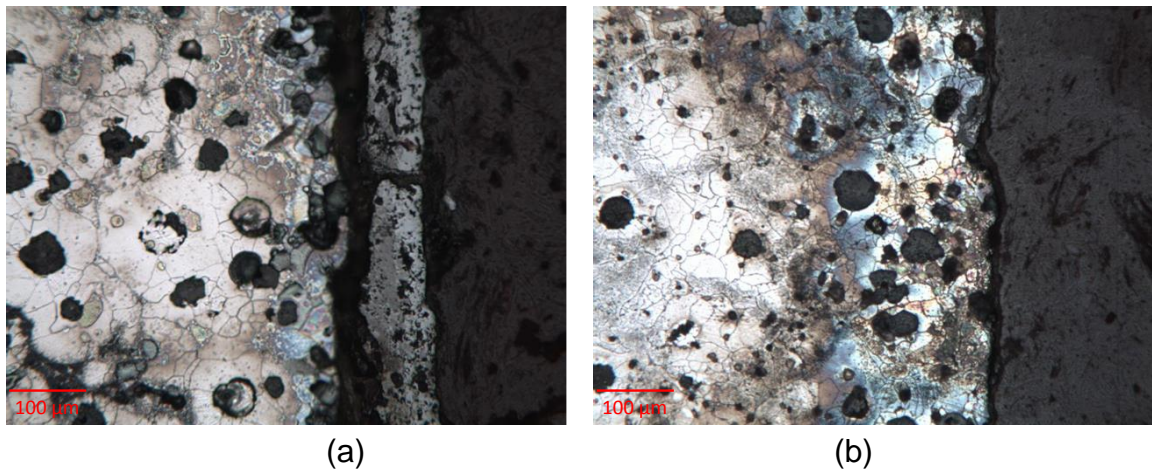


Figure 32. Images of sample edge at 200X of (a) 50HS and (b) HSM after 30 hour 800 °C heat treatment

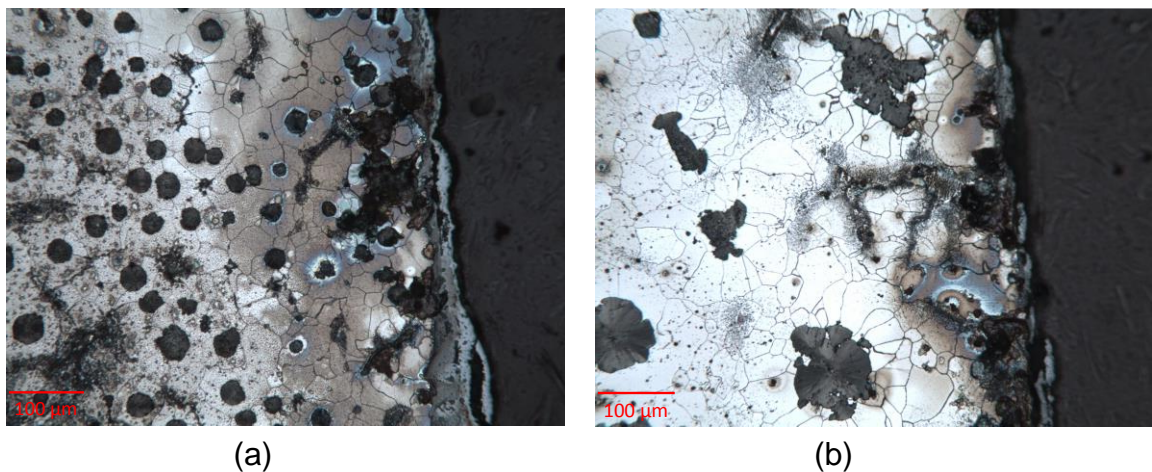


Figure 33. Images of sample edge at 200X of (a) 50HS and (b) HSM with 30 minute 800 °C heat treatment

4.2.5 900 °C results

At this temperature the major differences between the two alloys again lies in the thickness of the oxide layer and in the number and size of nodules present near the surface of the alloys (Figures 34 and 35). The 50HS alloy has a very noticeable oxide layer as compared to the HSM alloy, being approximately six to seven times thicker. There also appears to be a greater number of graphite nodules present in the 50HS alloy. It interesting to note the differences in the thickness of the oxide layer when comparing the 30 hour heat treatment samples to the 30 minute heat cycling samples. It appears that the cyclic exposure to higher temperatures results in a thicker oxide layer formed.

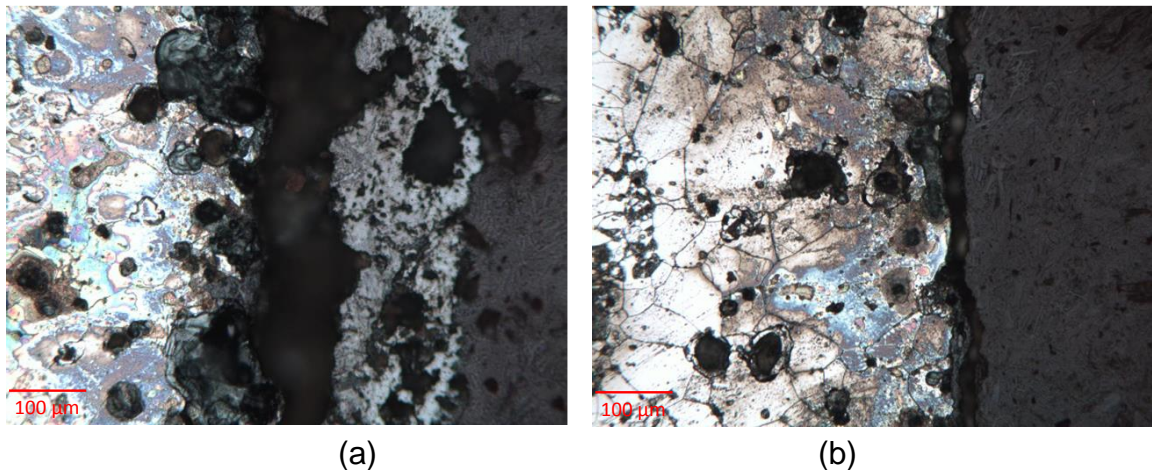


Figure 34. Images of sample edge at 200X of (a) 50HS and (b) HSM after 30 hour 900 °C heat treatment

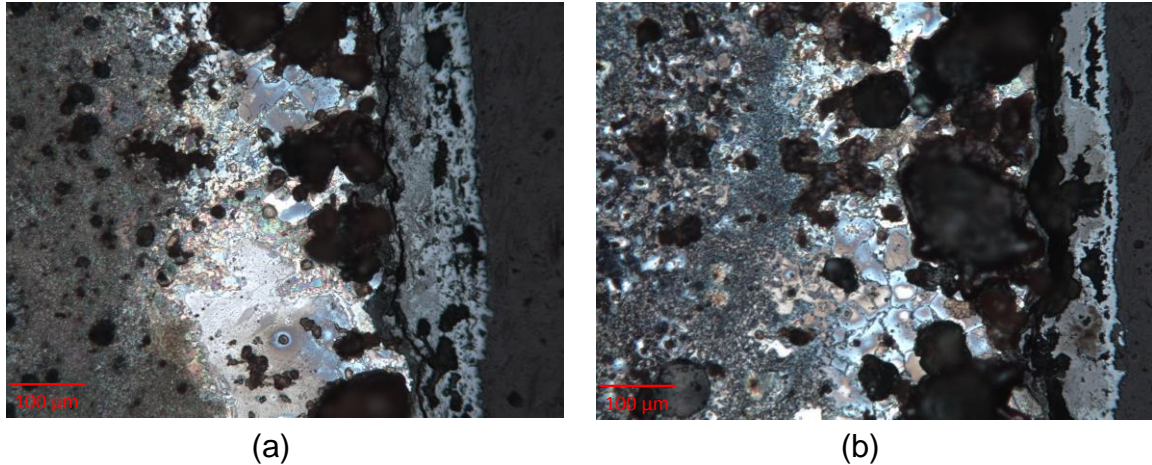


Figure 35. Images of sample edge at 200X of (a) 50HS and (b) HSM with 30 minute 900 °C heat treatment

4.3 Metallurgy

Grain sizes determined from the samples are shown in Tables 7 and 8. In both the 30 hour heat treatment and the 30 minute heat cycling heat treatments the HSM alloy had larger grain sizes than the 50HS alloy, except for the room temperature samples. These results can be compared to the images obtained and shown in Figure 36 below.

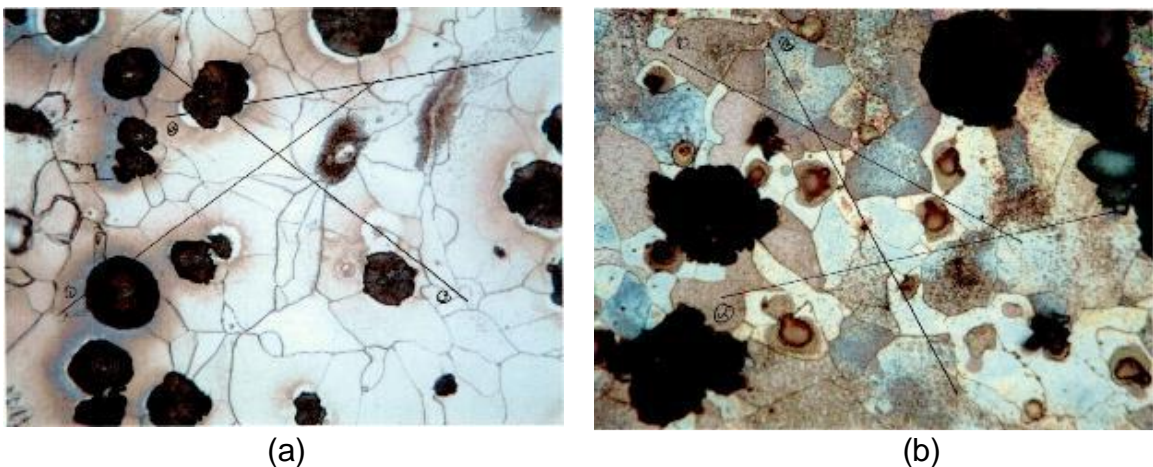
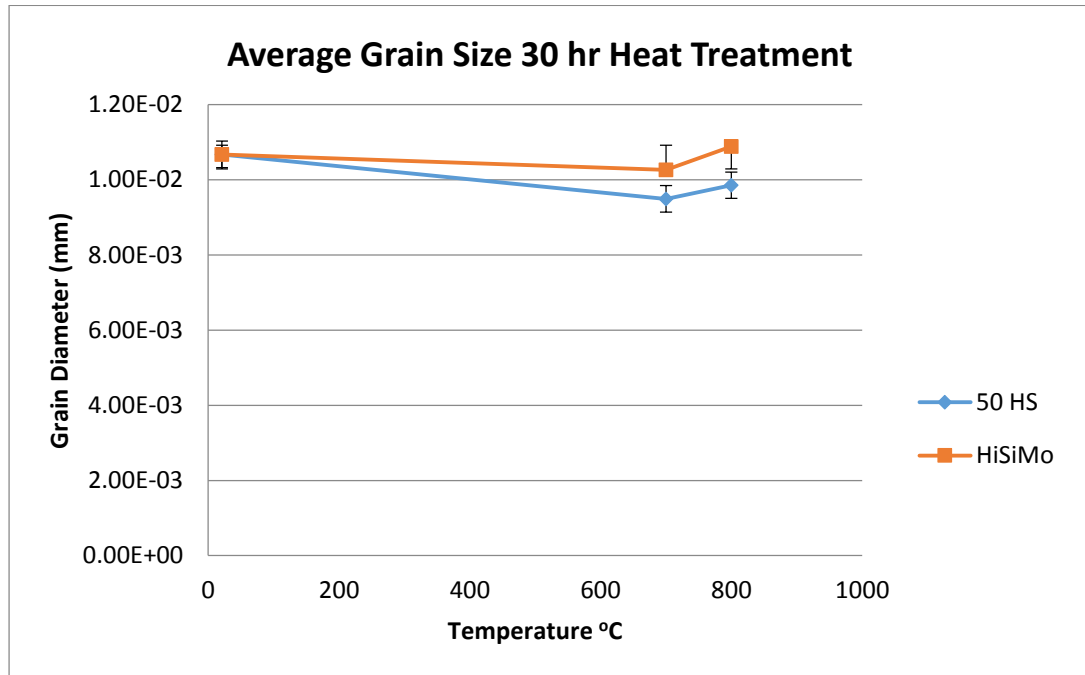


Figure 36. Grain sizing of (a) 50HS 700 °C Heat Cycle and (b) HSM 700 °C Heat Cycle

Table 7. 30 Hour Heat Treatment Grain Size

30 Hour Heat Treatment				
	50HS		HSM	
Temp °C	Avg. Grain Dia (in)	ASTM Grain Size	Avg. Grain Dia (in)	ASTM Grain Size
21	4.20E-04	12.0	4.20E-04	12.0
700	3.74E-04	12.3	4.04E-04	12.3
800	3.88E-04	12.3	4.28E-04	12.0

**Figure 37. Average Grain Diameter after 30 Hour Heat Treatment****Table 8. 30 Minute Heat Cycle Grain Size**

30 Minute Heat Treatment				
	50HS		HSM	
Temp °C	Avg. Grain Dia (in)	ASTM Grain Size	Avg. Grain Dia (in)	ASTM Grain Size
21	4.20E-04	12.0	4.20E-04	12.0
600	5.28E-04	12.0	5.80E-04	11.5
700	5.24E-04	12.0	5.50E-04	12.0
800	5.53E-04	12.0	6.00E-04	11.5

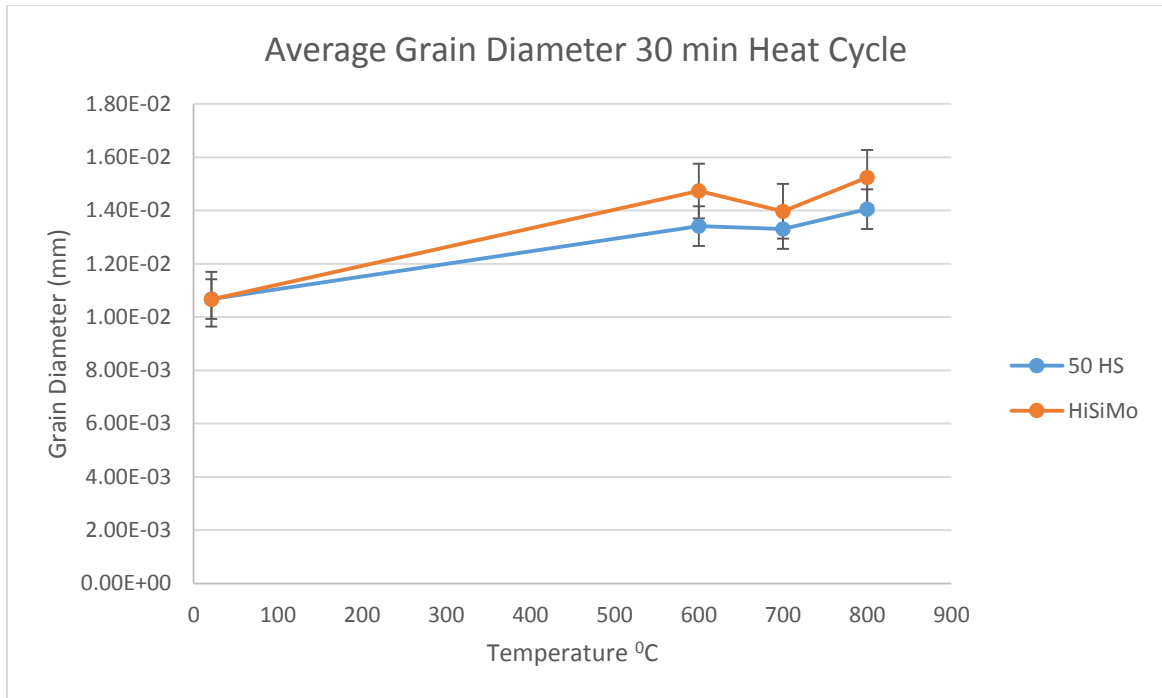


Figure 38. Average Grain Diameter after 30 Minute Heat Cycle Treatment

4.4 Ultrasonic testing

Three different moduli, Young's Modulus (E), Bulk Modulus (G), Shear Modulus (K), and Poisson's ratio (ν), were determined for the alloys using nondestructive ultrasonic testing, and the results are shown in Tables 9 and 10. The most important of the three moduli are Young's and shear, as they will provide an indication of how the sample will react while under load during the fatigue portion of the research. From these initial nondestructive results it was anticipated that the alloys will have different slopes on the stress/strain curve and different yield points when transformation from elastic to plastic deformation occurs. It should be noted that the time used in the calculations is based on the thickness of the sample used. The values used in the determination of the above stated moduli are shown below.

Table 9. Values used in Ultrasonic Testing

	50HS				HSM			
	Δt_L (μs)	Δt_S (μs)	V_L (mm/ μs)	V_S (mm/ μs)	Δt_L (μs)	Δt_S (μs)	V_L (mm/ μs)	V_S (mm/ μs)
Test 1	4.985	9.134	5.673	3.098	2.225	4.095	5.716	3.106
Test 2	4.990	9.130	5.669	3.093	2.220	4.080	5.730	3.116
Test 3	4.990	9.132	5.670	3.095	2.230	4.085	5.704	3.116

The value of the elastic modulus calculated from this ultrasonic testing are within the literature values of 160 to 180 GPA.

Table 10. Results of ultrasonic examination of cast samples

(Values in the yellow cells are entered, values in the green cells are calculated)		
	Hi-Si-Mo	50 HS
Sample thickness (m)	0.00636	0.01413
ΔT_L (seconds)	2.23E-06	4.99E-06
V_L (m/s)	5.72E+03	5.67E+03
ΔT_S (seconds)	4.10E-06	9.13E-06
V_S (m/s)	3.11E+03	3.09E+03
density (kg/m ³)	7083	7040.33
Sample:		
E (Gpa)	176.4	173.6
ν	0.2906	0.2879
G (Gpa)	68.3	67.4
K (Gpa)	140.4	136.4

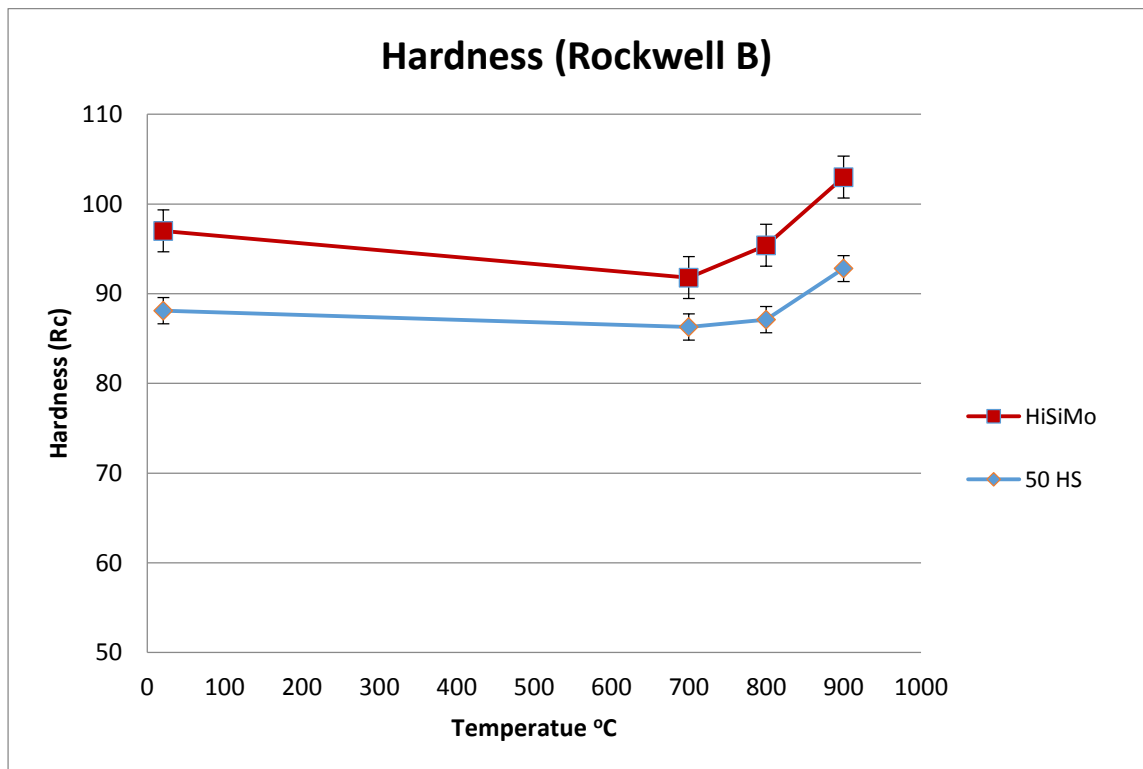
Young's Modulus	$E = \rho v_s^2 (3 v_L^2 - 4 v_s^2) / (v_L^2 - v_s^2)$			
Poisson's Ratio	$\nu = [1 - 2 (v_s/v_L)^2] / [2 - 2 (v_s/v_L)^2]$			
Shear Modulus	$G = v_s^2 \rho$			
Bulk Modulus	$K = \rho [v_L^2 - (4/3) v_s^2]$			
V is velocity,				
ρ is density				
ΔT is the time between successive echoes				
L is the longitudinal polarized wave				
S is the shear polarized wave				

4.5 Hardness testing

Results from hardness tests performed on samples from the 30 hour isothermal heat treatment are shown below in Table 11 and Figure 39. As the samples went through the various heat treatments, the values for the two alloys began to differ. The change in values can be attributed to either the change in microstructure as the samples underwent heat treatment, or the location of the indenter on the sample (placement over a nodule can result in slightly lower hardness values).

Table 11. Values of hardness measurements

Rockwell B Hardness Values								
	HSM				50HS			
Temp	Untreated	700° C	800° C	900° C	Untreated	700° C	800° C	900° C
Trial 1	93.2	92.2	96	102	90	84.5	86.5	92.5
Trial 2	97.5	90.8	95.5	103	85.8	86.2	88	93
Trial 3	98.8	93	95.2	103.8	87.5	86.4	86.8	92.4
Trial 4	98.6	91	95	103	89.2	88.2	87	93.2
Average	97	91.8	95.4	103	88.1	86.3	87.1	92.8

**Figure 39. Hardness Values after 30 Hour Heat Treatment**

An estimation of tensile strength based on hardness can be made, based on Figure 40 below [1].

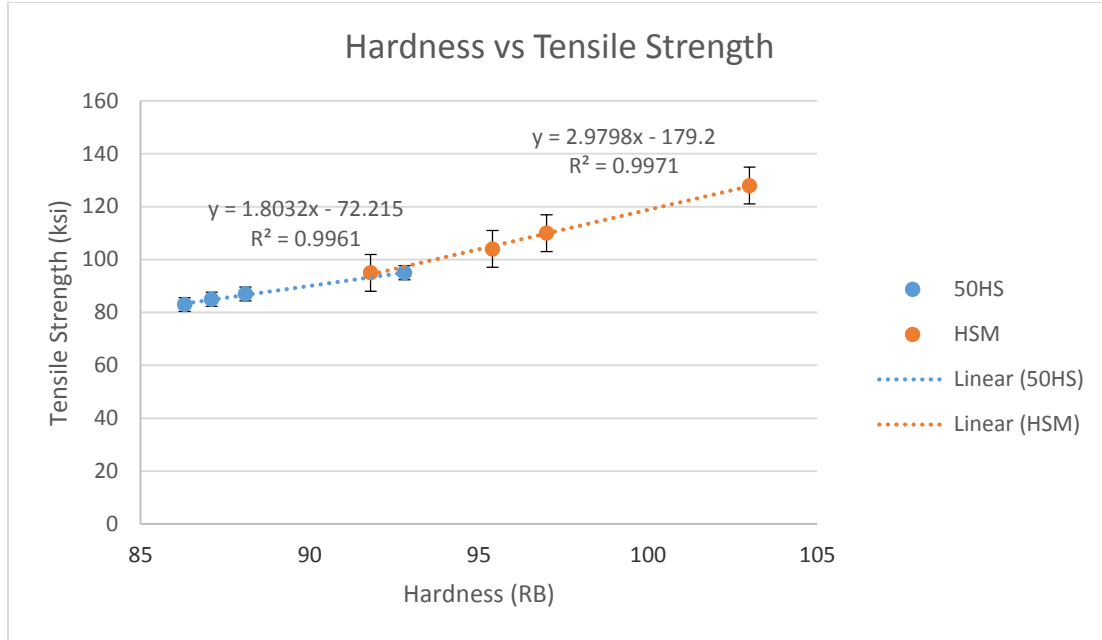


Figure 40. Hardness vs. Average Tensile Strength

4.6 Tensile test results

Tensile tests for the alloys were conducted according to ASTM E 08-04. The samples were machined from raw stock per Figure 1 – Subsize Specimen from the ASTM above. The nominal dimensions for the specimens are shown below in Table 12. A typical tensile sample is shown in Figure 41.

Table 12. Dimensions of Tensile Specimens

Dimension	Length (in)
L	3.29
B	1
G	1

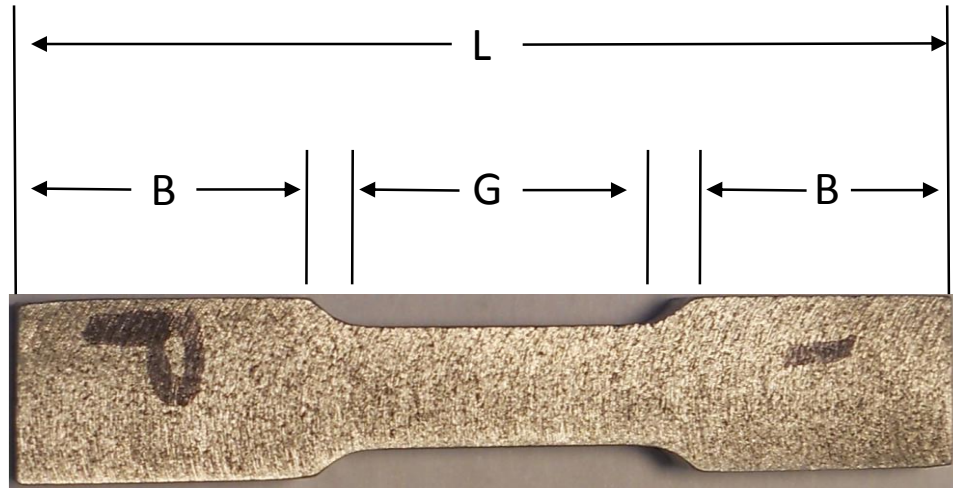


Figure 41. *Picture of a Tensile Specimen*

All tensile tests were conducted with an Instron 5969, electrodynamic testing system. The rate of movement for the crosshead of the machine was 0.01 inches per second until failure. For the 50HS alloy, all samples failed in the center of the gauge section. For the HSM alloy, the failures all occurred near one end of the gauge section (Fig 42). There appeared to be no particular reason for the change of failure location.



Figure 42. *Picture of Tensile Specimens after Failure*

The results of the three tensile tests for each alloy are shown in Figures 43 and 44 (the straight lines on both graphs – angled and horizontal were the lines used for the yield determination). Of note, the HSM alloy showed very little necking prior to failure, which is typical for most cast irons, unlike the 50HS alloy which did show a certain degree of necking. For all the alloy tests there is a slight lag in the linear extension phase, (as seen in the lower left hand of the graphs below) which is probably a result of the grips biting into the sample before the extension phase commenced. In determining the slope of the linear extension phase, this initial non-linear portion is ignored.

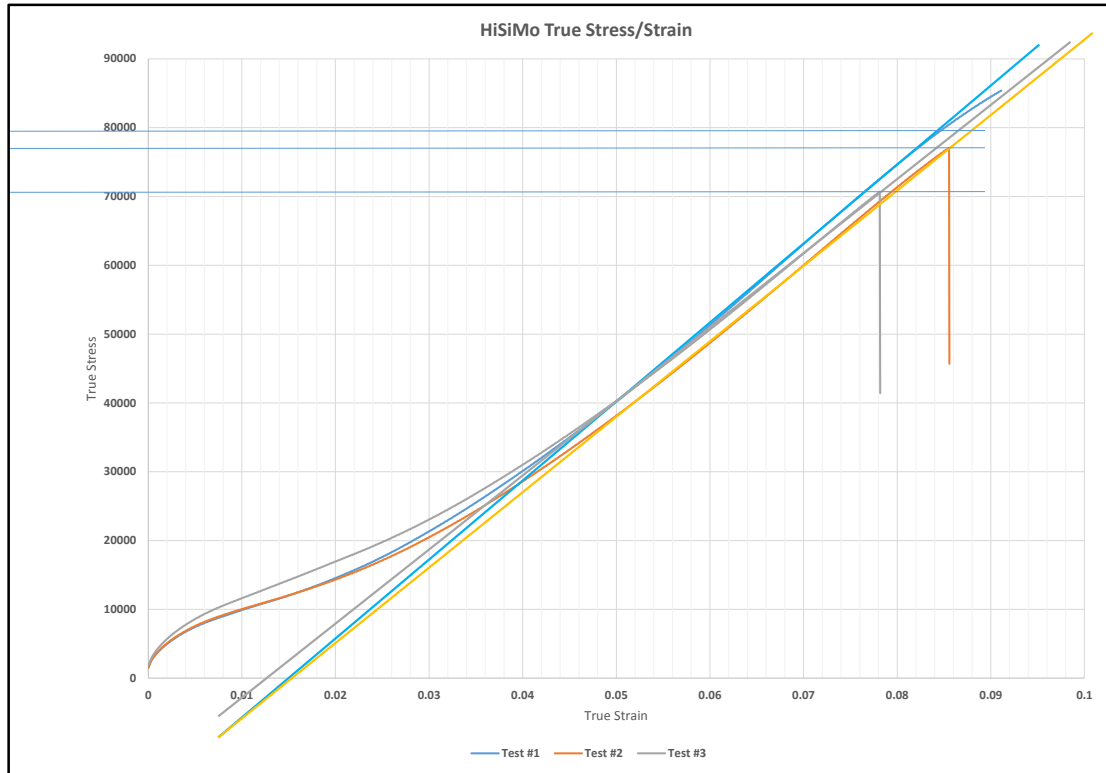


Figure 43. Tensile test results for HSM alloy

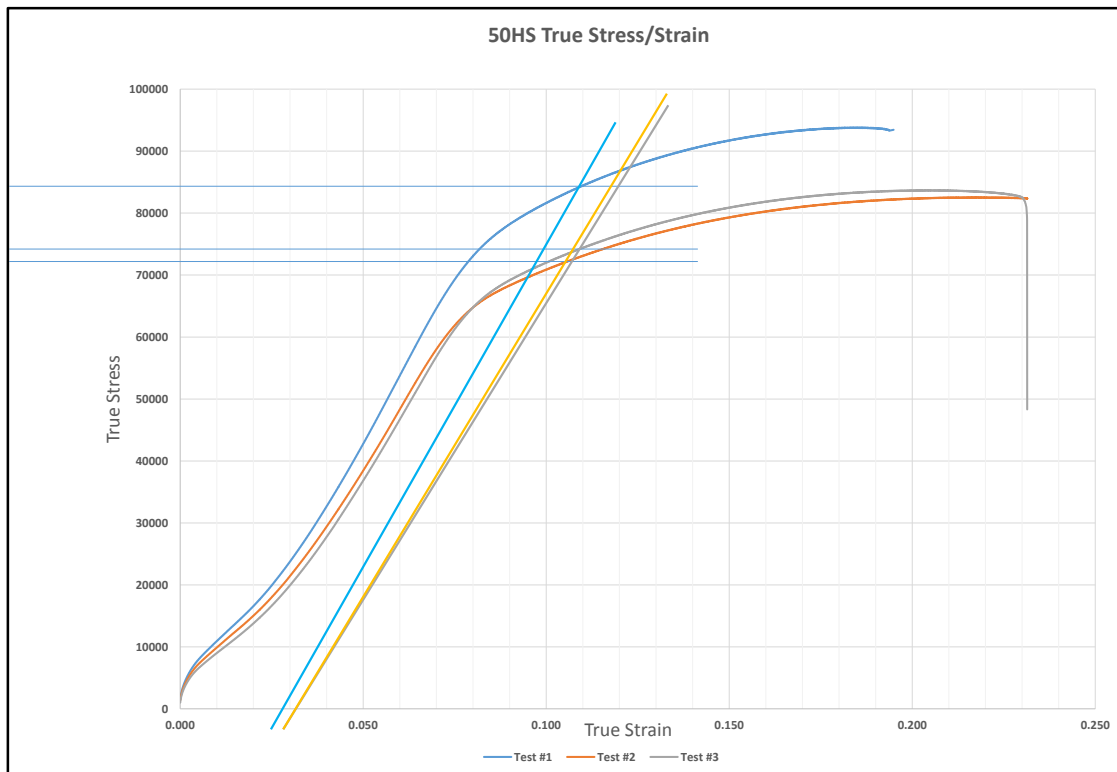


Figure 44. Tensile test results for 50HS alloy

Since there was little or no necking in the HSM alloy the point of failure was taken as the Yield Strength for that alloy. For the 50HS alloy, a 0.2 % offset was used to determine the Yield Strength, as prescribed in ASTM E 08-04. The results of the Yield Strength tests are shown below in Table 13. For the fatigue work, the average of the tests for each alloy was used in load calculations.

Table 13. *Yield Strength of Alloys*

Alloy	Test #	Yield Stress (ksi)
HSM	1	79.75
HSM	2	76.67
HSM	3	70.64
Average		75.69
50HS	1	84.15
50HS	2	72.73
50HS	3	73.86
Average		76.91

4.7 Fatigue data analysis

All the fatigue work performed during this study, both at room temperature and at high temperature, was done at constant load. As briefly mentioned in section 3.7, there were issues with the sensitivity of the system with regards to position location. It was determined that the system could not maintain such small displacements needed for this work, therefore it was required that the system operate in “Load Control”, where the required loads were approximately 50% of the load cell capacity, and provided much greater control of the load frame during operation. To accurately monitor the change in position an external extensometer was used to record data. Because of this type of fatigue testing,

the data available for recording and further analysis was limited to change in position versus a constant load. Analysis of the data is broken into three subsections: behavior at specific temperature; calculations of flexural stress, flexural strain, and flexural modulus; and fitting the data available to a potential model. Any uncertainty in the data is related to the accuracy of the load cell and extensometer used. The load cell was calibrated to within +/- 1 % accuracy (1124.045 lbf), and the extensometer (Range +/- 1 mm) was calibrated using an external micrometer prior to use.

4.7.1 Temperature

At room temperature (22 °C) each of the alloys exhibited no real change in the modulus of the material, which was to be expected when no additional energy was input into the system. The change in displacement for each of the alloys was minimal after initial cycles. In the plot of the HSM data the average change in displacement over time (cycles), (Figure 45, remains constant. However, in looking at a similar plot for the 50HS alloy, it can be seen that the alloy exhibited a slightly irregular behavior from approximately 60,000 cycles to 80,000 cycles (Figure 46). If the data is examined at a smaller range of the Y axis (Figure 47), these irregularities become even more pronounced.

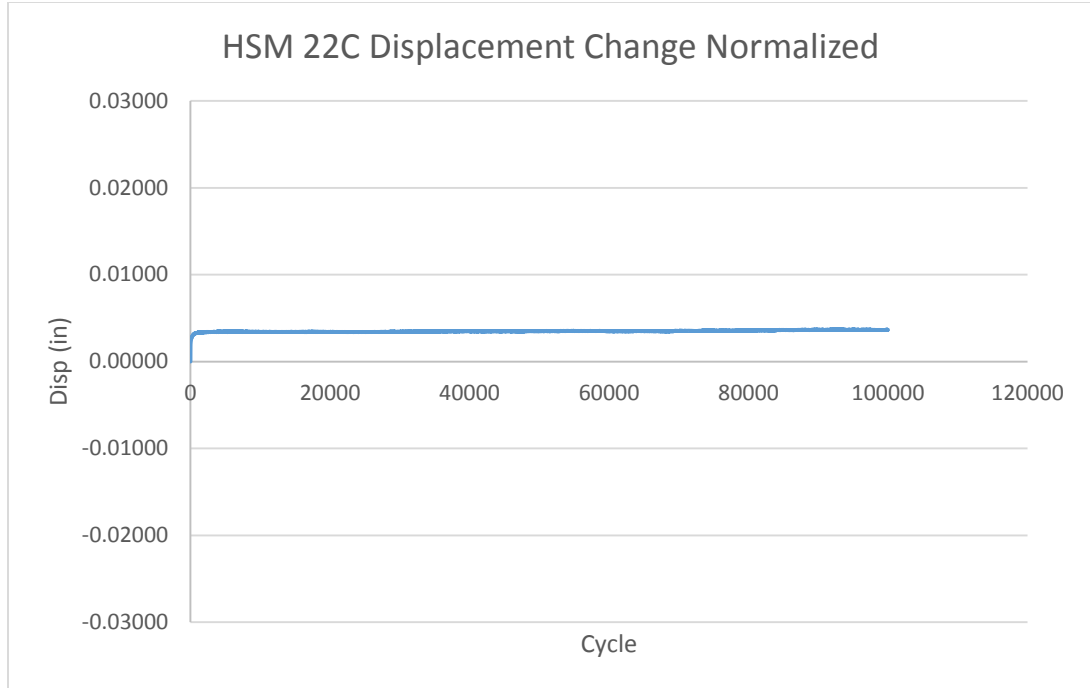


Figure 45. HSM displacement change over time at 22 °C

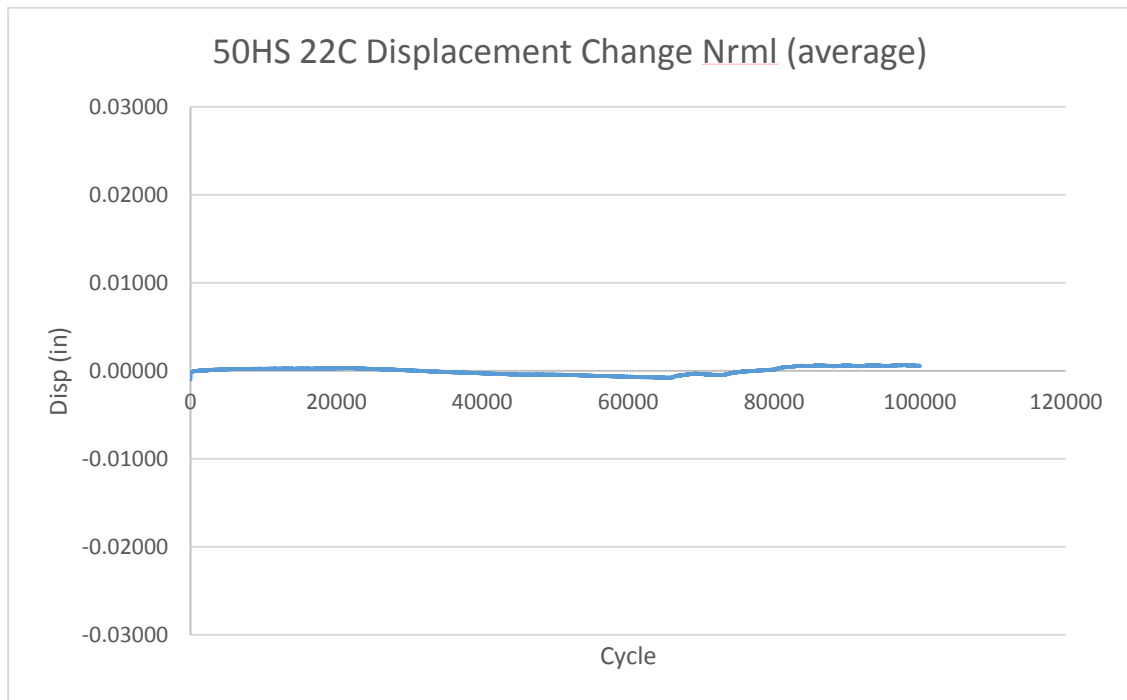


Figure 46. 50HS displacement change over time at 22 °C

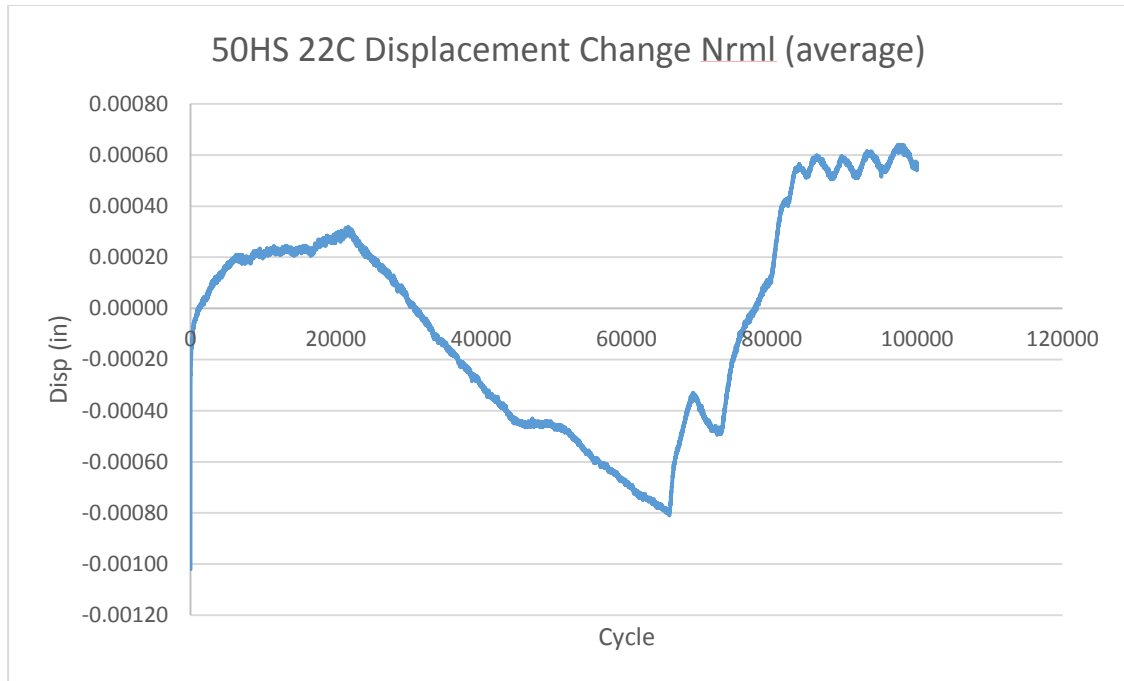


Figure 47. Dislocation change average at a smaller scale

As discussed in Chapter 3, one of the most noticeable differences between the two alloys is the presence of pearlite in the HSM sample. It is clear from comparing Figures 48 and 49 that the HSM alloy has greater amounts of pearlite than the 50HS alloy. Apart from this difference, the alloys are similar in the shape and size of nodules. Due to this test being at room temperature, there is no noticeable scale build-up on the outer edge of either sample.

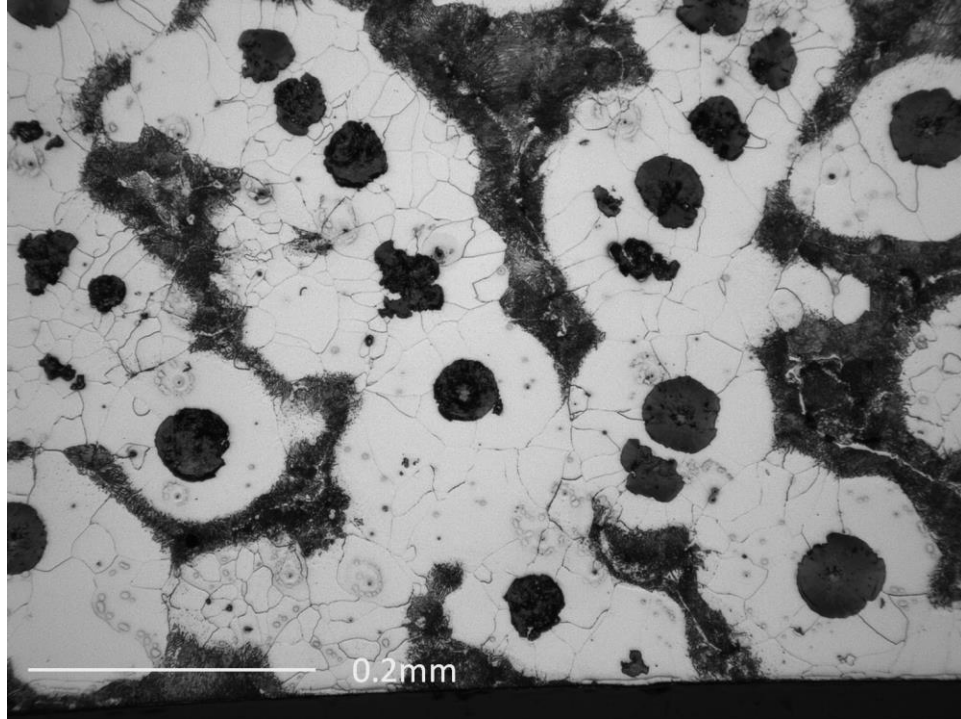


Figure 48. *HSM 22°C 200X Center of sample*

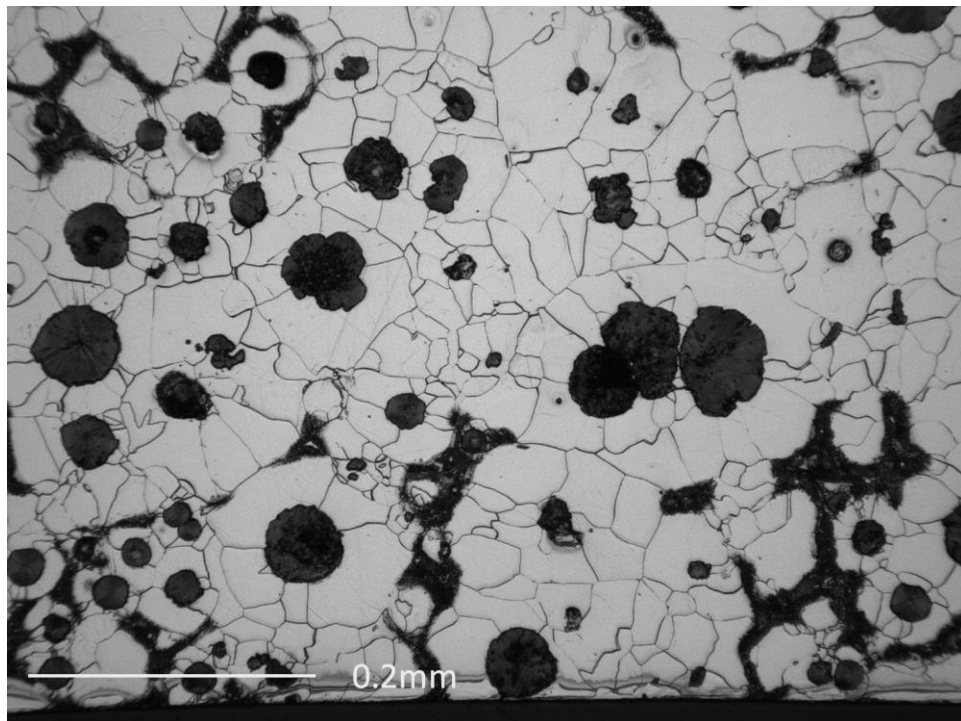


Figure 49. *50HS 22°C 200X Center of sample*

For each alloy, fatigue at 400 °C exhibited what appears to be a combination of hardening and possibly a slight amount of thermal expansion, due to the position of the actuator moving downward while the system remains at a constant minimum and maximum load. In looking at the two figures below (Figures 50 and 51) the overall assumption is that after the instantaneous change in the position ceased, the materials exhibited a linear response for the remainder of the testing process.

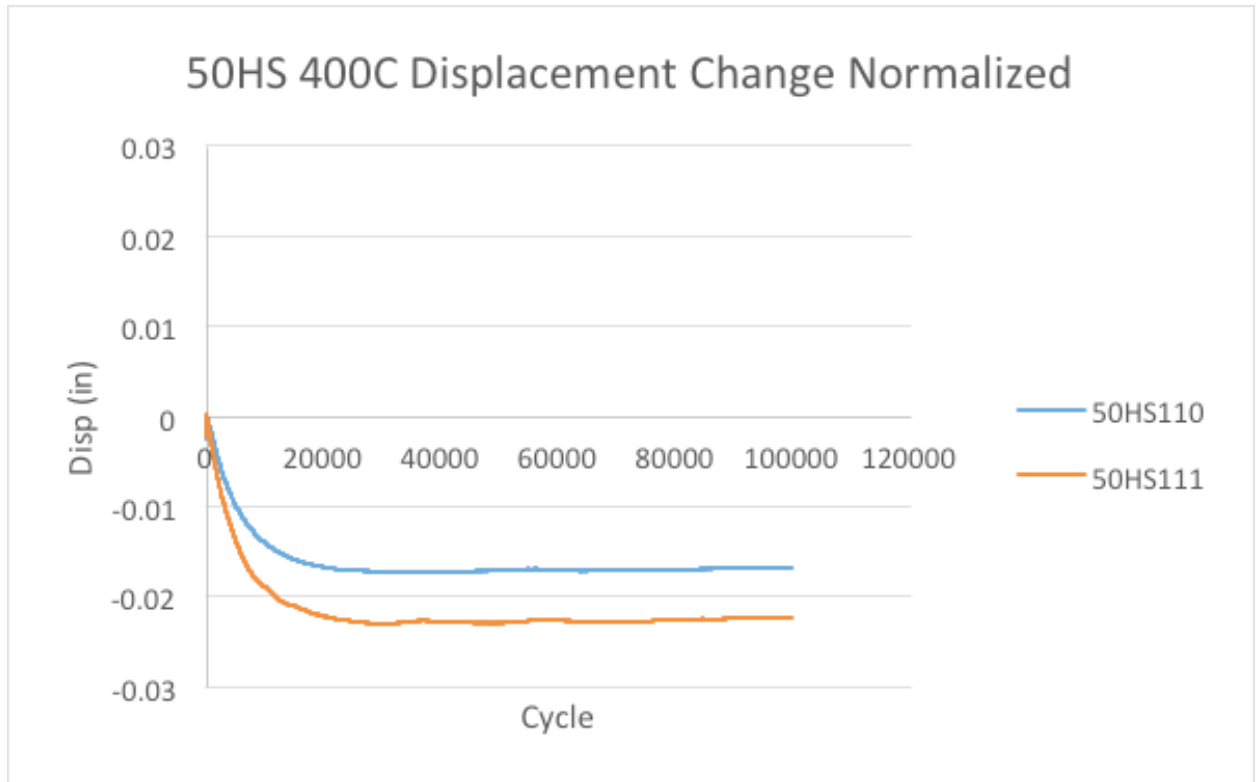


Figure 50. 50HS displacement change over time at 400 °C

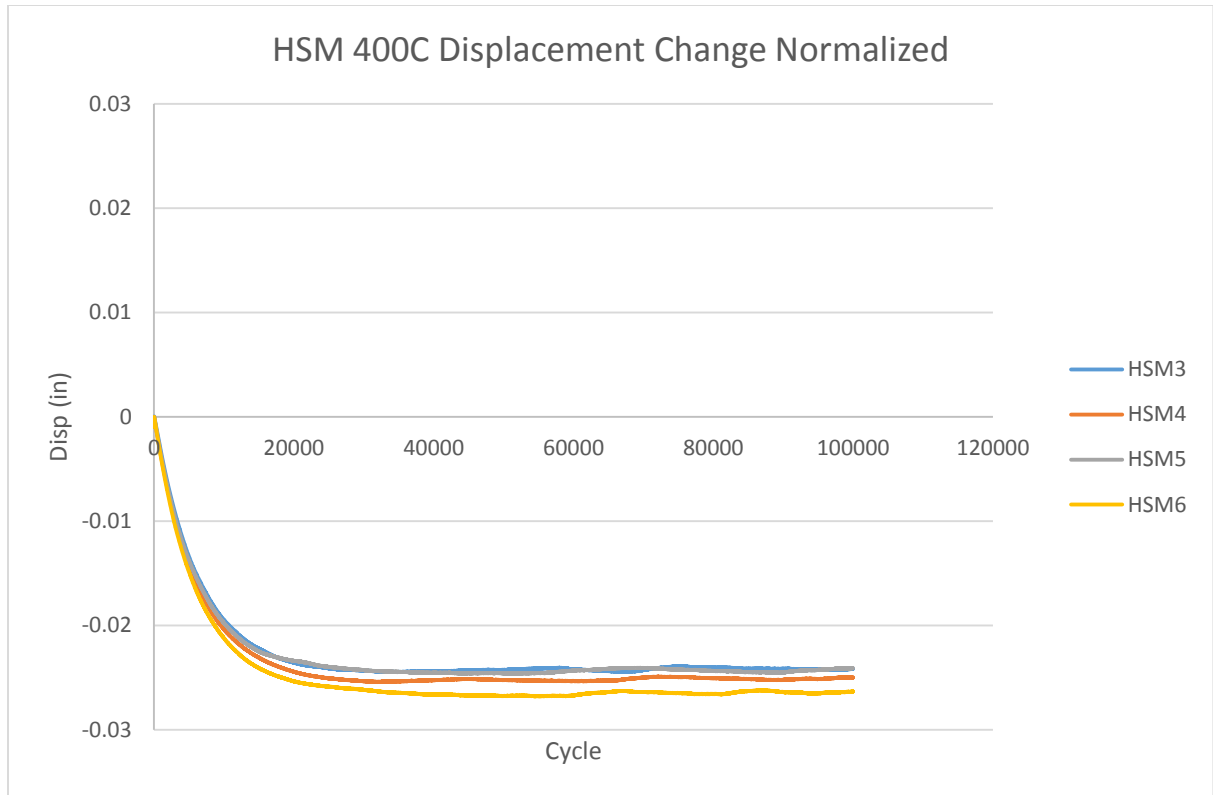


Figure 51. HSM displacement change over time at 400 °C

Even though both alloys show evidence of an initial change in displacement during the first one fourth of the tests, the geometry of the samples is assumed to have remained consistent during the fatigue process, i.e. there was no dimensional change visible at the conclusion of the fatigue testing period. Similarly, the microstructure of the alloys remained unique to each alloy. The 50HS alloy shows better grain boundary definition than the HSM alloy, but the nodules of 50HS are less uniform. As discussed in the literature review, one factor leading to failure of cast iron is the irregular shape of the nodules. Although both samples (Figures 52 and 53) were fatigued for almost seven hours, neither showed signs of creep, either in the plots of the displacement or in the micrographs.

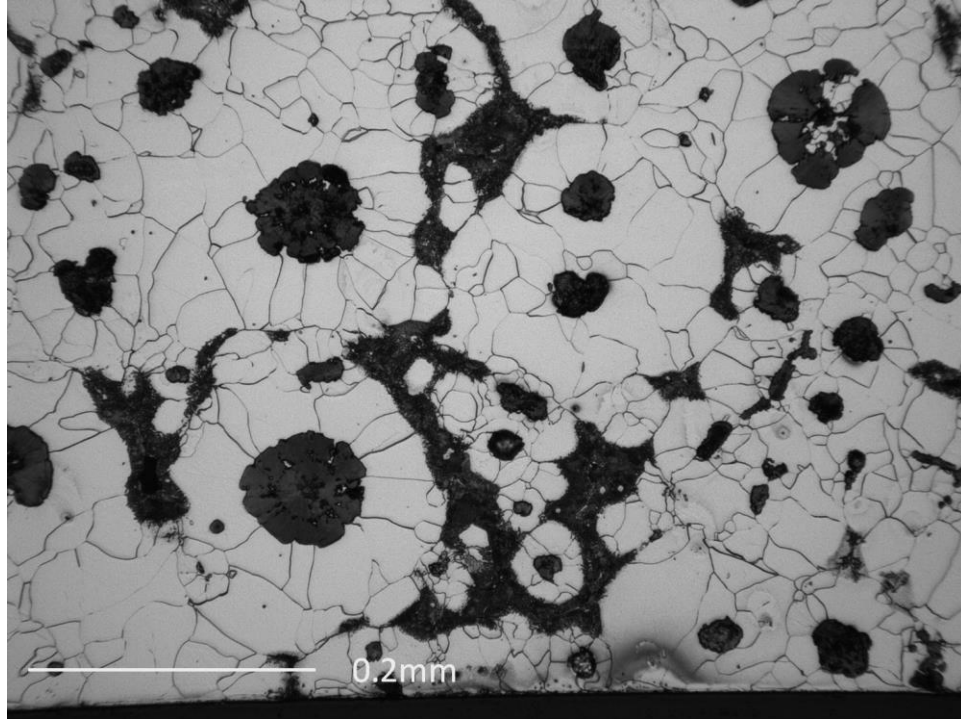


Figure 52. 50HS110 200X Center 400 °C

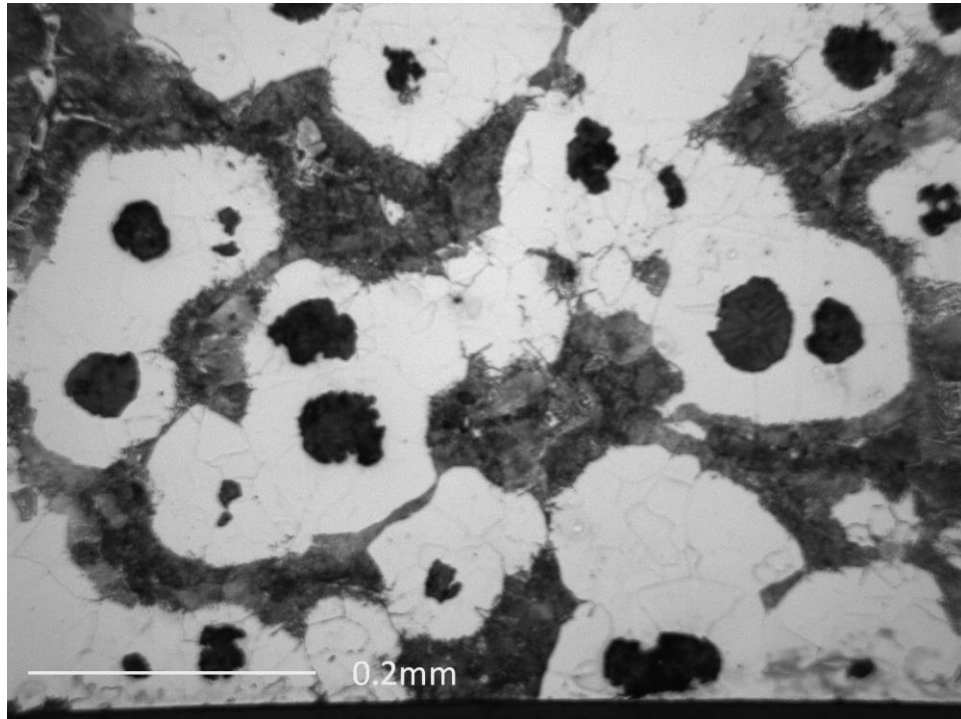


Figure 53. HSM3 200X Center 400 °C

The 50HS alloy's behavior at 600 °C varies markedly from its behavior at lower temperatures while the HSM does tend to display behavior similar to its lower testing temperature. In looking Figure 54 below, both samples show evidence of creep after approximately 20% of the test has been run. Creep was suspected since, in looking at the change in displacement of the actuator after the 20,000 cycle mark, it can be seen that the actuator is consistently moving upwards in order to maintain the same consistent cyclic load. After examination of one of the samples after fatiguing, (Figure 55) there is clear evidence of deformation at temperature while under load over a long period of time. Estimates of the yield strength at 600 °C give a value of 58.5 ksi, which is well above the stress placed on the material during the test. Thus, creep is the only mechanism that can account for the observed deformation. Samples 50HS112 showed a small amount of hardening before creep which is evidenced by the downward slope of the curve in the initial portion of the test (Figure 54), while sample 50HS113 showed only a steady state before the onset of creep.

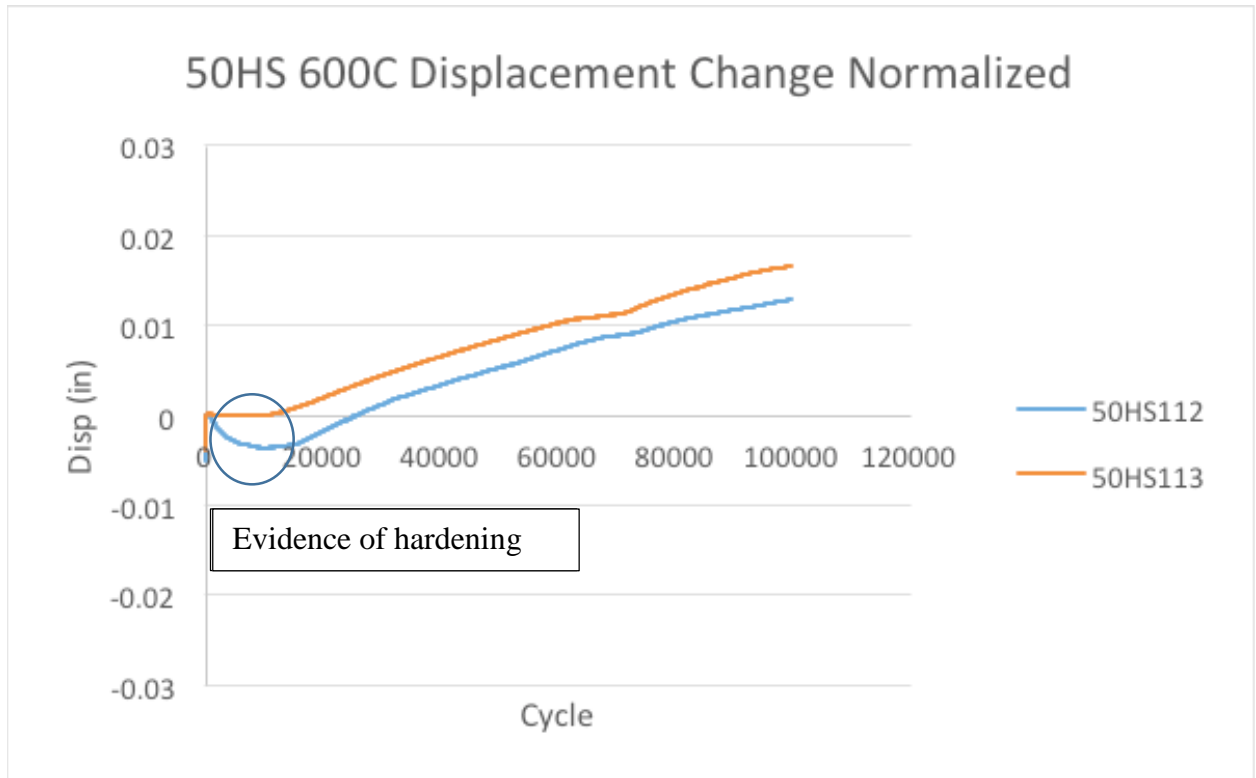


Figure 54. 50HS displacement change over time at 600 °C

As can be seen below in Figure 55 and from the displacement change in Figure 54, the exposure to a constant load for a long period of time has caused deformation of the sample 50HS113 to approximately 1.3 mm.

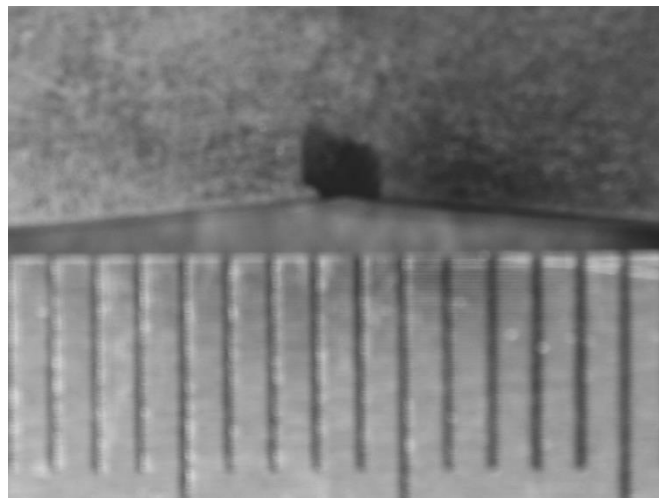


Figure 55. Deflection of 50HS sample after fatiguing (scale in mm)

For the HSM alloy samples behavior during the testing process was similar to that of the 400 °C fatigue tests. It appears that there is an amount of hardening in the initial portion of the fatigue process, although the extent is not to the same level of the 400 °C test due to the onset of creep, as evidenced in Figure 57, which shows a slight deformation. One of the samples from this alloy set had failure occur around 53,000 cycles.

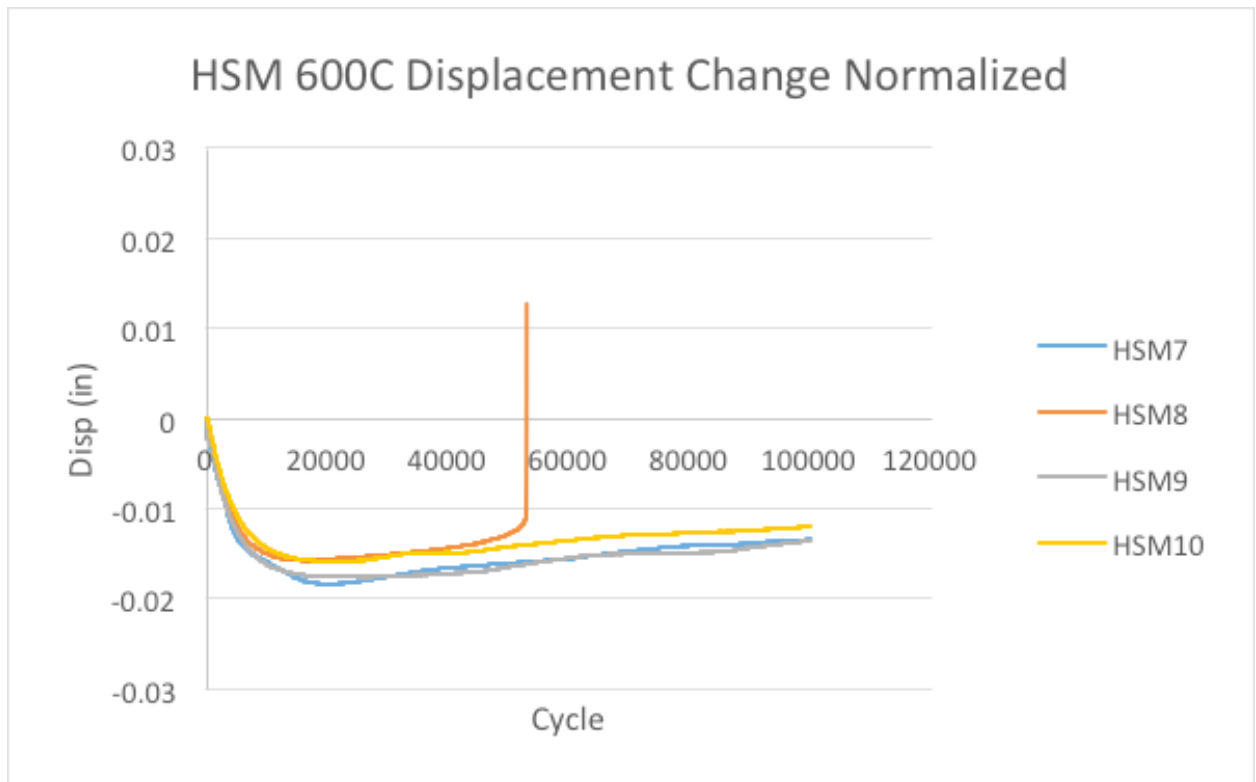


Figure 56. HSM displacement change over time at 600 °C

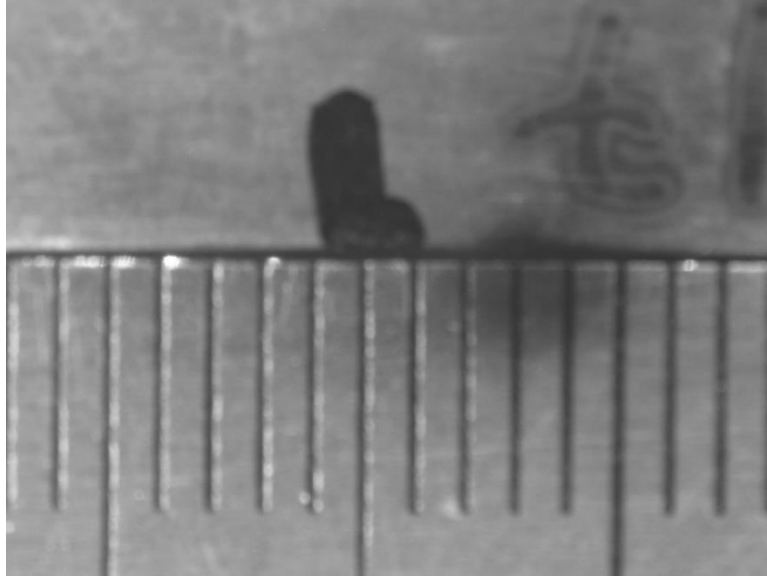


Figure 57. Slight deflection of HSM sample after fatiguing (scale in in mm)

The slight variation noted between the microstructures of the two alloys is also beginning to increase and become more apparent (Figures 58 and 59). The 50HS alloy is starting to form pearlite in between the grains, while the HSM alloy shows sign of what might be an intermetallic, such as a molybdenum carbide, forming as a result of the increased molybdenum or silicon content (102, 103, 111, 112). The micrograph for the 50HS alloys also shows an elongation of some of the grains, along with an elongation of some of the graphite nodules.

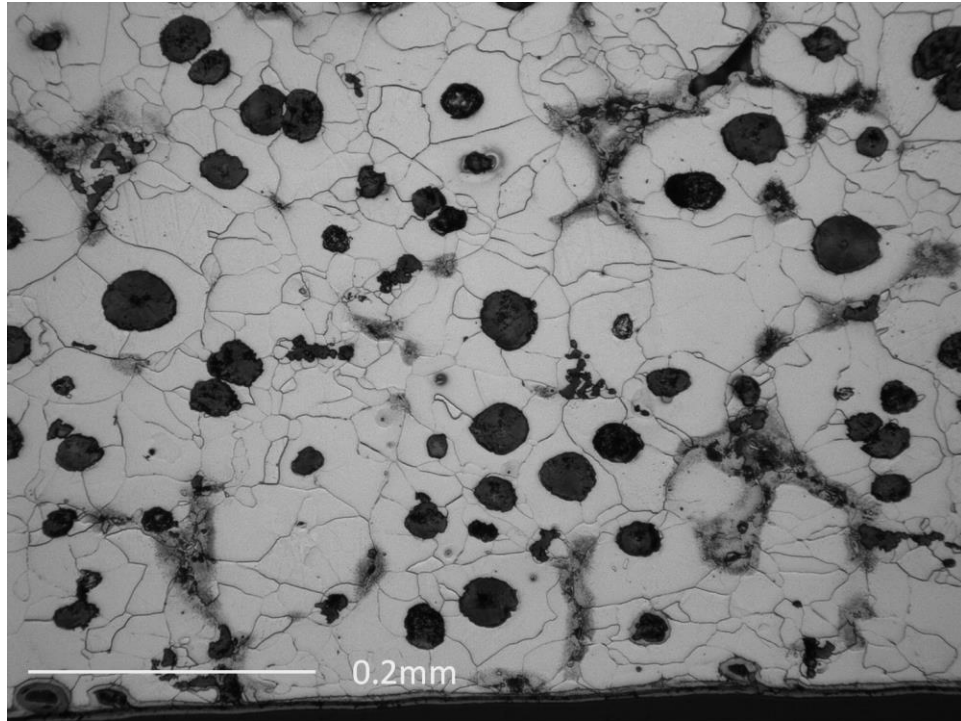


Figure 58. 50HS112 200X Center 600 °C

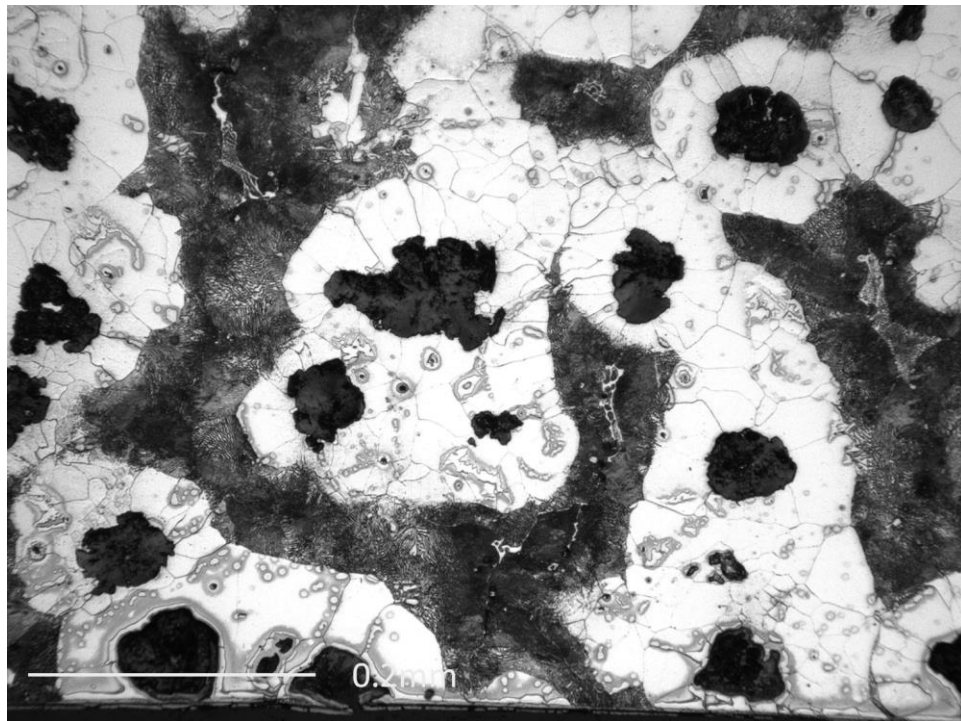


Figure 59. HSM7 200X Center 600 °C

In the HSM alloy pearlite can be seen surrounding the now irregularly shaped graphite nodules is starting to breakdown.

Data collected from this final temperature of 700° C temperature was appears different from the lower temperature test. As can be seen from the displacement figures (Figures 60 and 61), a large amount of displacement occurs at the beginning of the fatigue tests. Based on estimations of decrease in yield strength at 700 °C, to 34.1 ksi, (below the value used for the test) this deformation seems reasonable. For the 50HS samples, the change in displacement was so great that it is believed the sample deformed up to the point that the ends of the sample were actually touching the upper bend fixture, and what was recorded was actually the displacement of the upper bend fixture pushing into the sample. For the HSM alloy, the deformation is not quite to the extent of the 50HS, but when comparing the two alloys (Figs 62 and 63) from 0 to 10,000 cycles, one can see that the plastic flow for HSM is only slightly less than for the 50HS alloy. This deflection is illustrated in Figures 64 and 65 below. The actual amount of deflection was approximately 2.7 mm for both alloys.

The position of the curves in the graphs of Figures 60 and 61 are correlated with the position of the external extensometer used during the testing to monitor the position displacement. At this high temperature, the amount of movement of the actuator at the beginning of the testing process nearly exceeded the travel of the extensometer. To create a better representation for the movement of the sample during testing, the data for this temperature was set to a zero point which correlates to the initial point of data collection. This

“normalization” can result in some of the data appearing negative. This may appear confusing, but it is really only a reflection of the position of the extensometer, where it has a range of travel of positive and negative 40 thousandths of an inch. For the 50HS alloy, this resulted in the experimental curves for the two samples tested coinciding nicely. For two samples of the HSM alloy (HSM 16 and 17) the system captured an amount of yielding prior to the sample making contact with the upper bend fixture. For sample HSM15 that yielding was not captured. Thus, the HSM sample data appears spread over a larger displacement range.

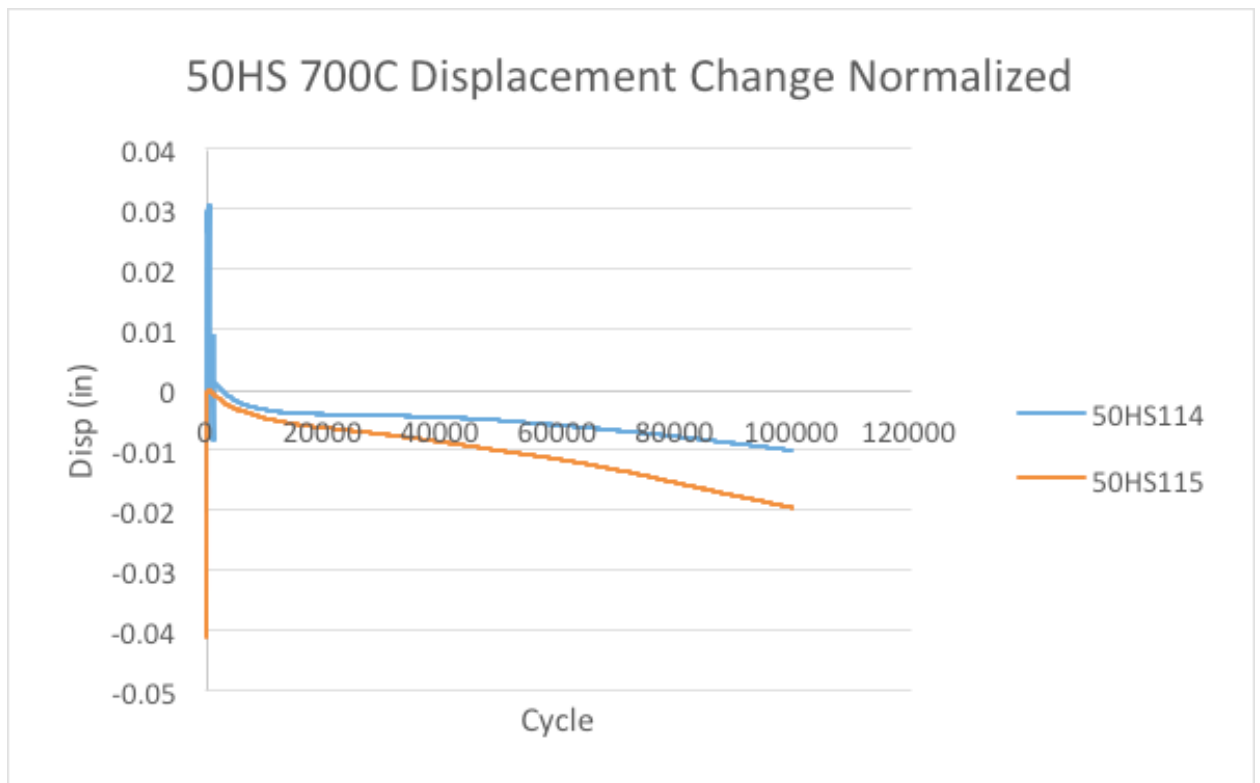


Figure 60. 50HS displacement change over time at 700 °C

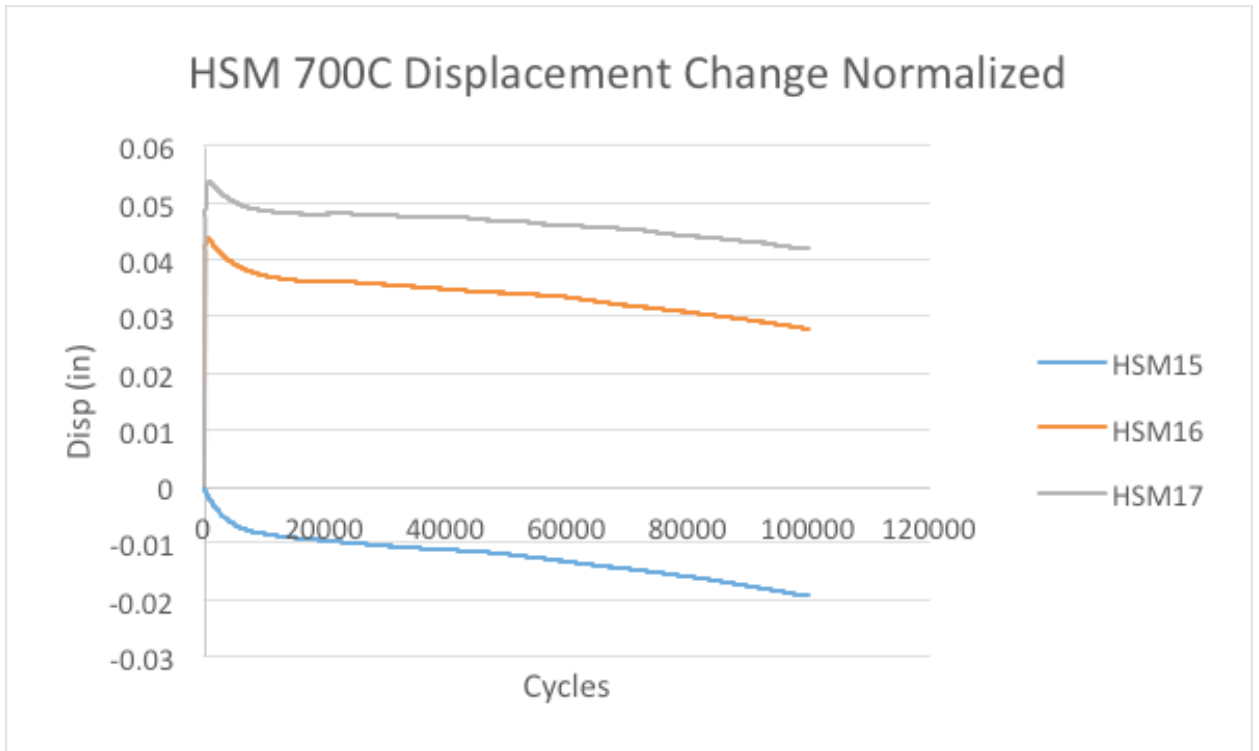


Figure 61. HSM displacement change over time at 700 °C

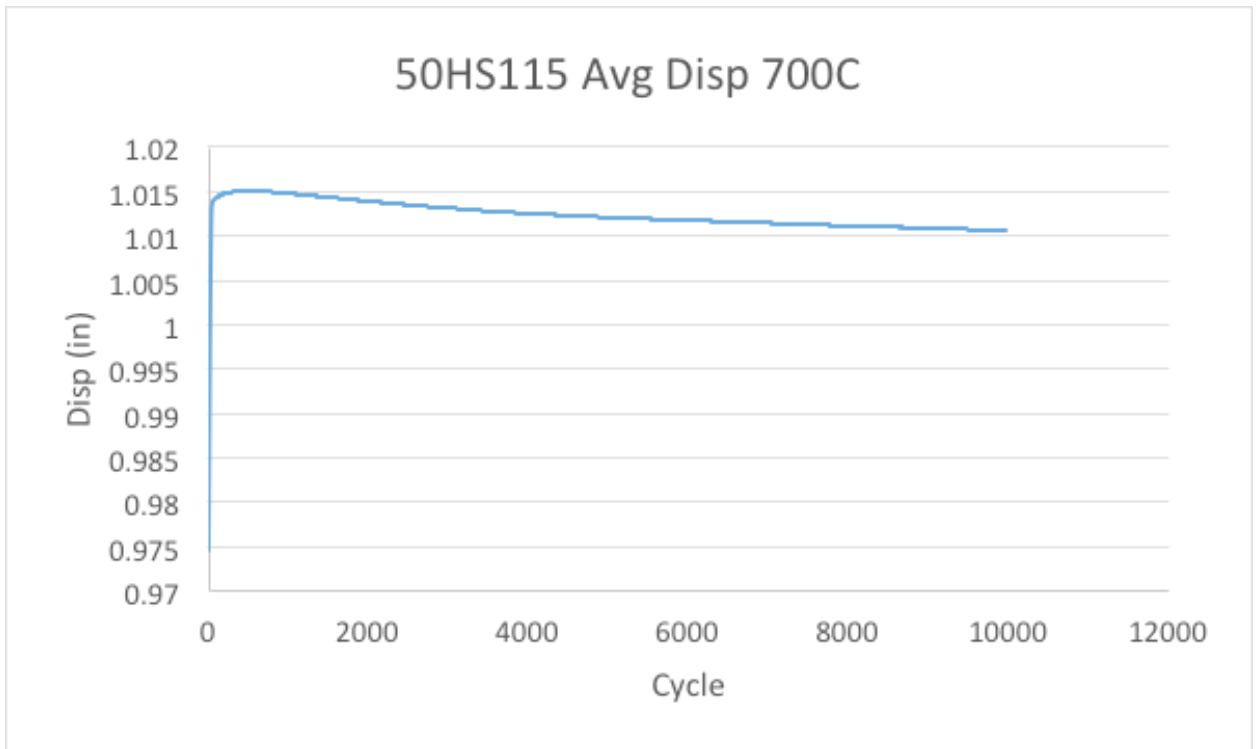


Figure 62. 50HS displacement change over time at 700 °C 10,000 cycles

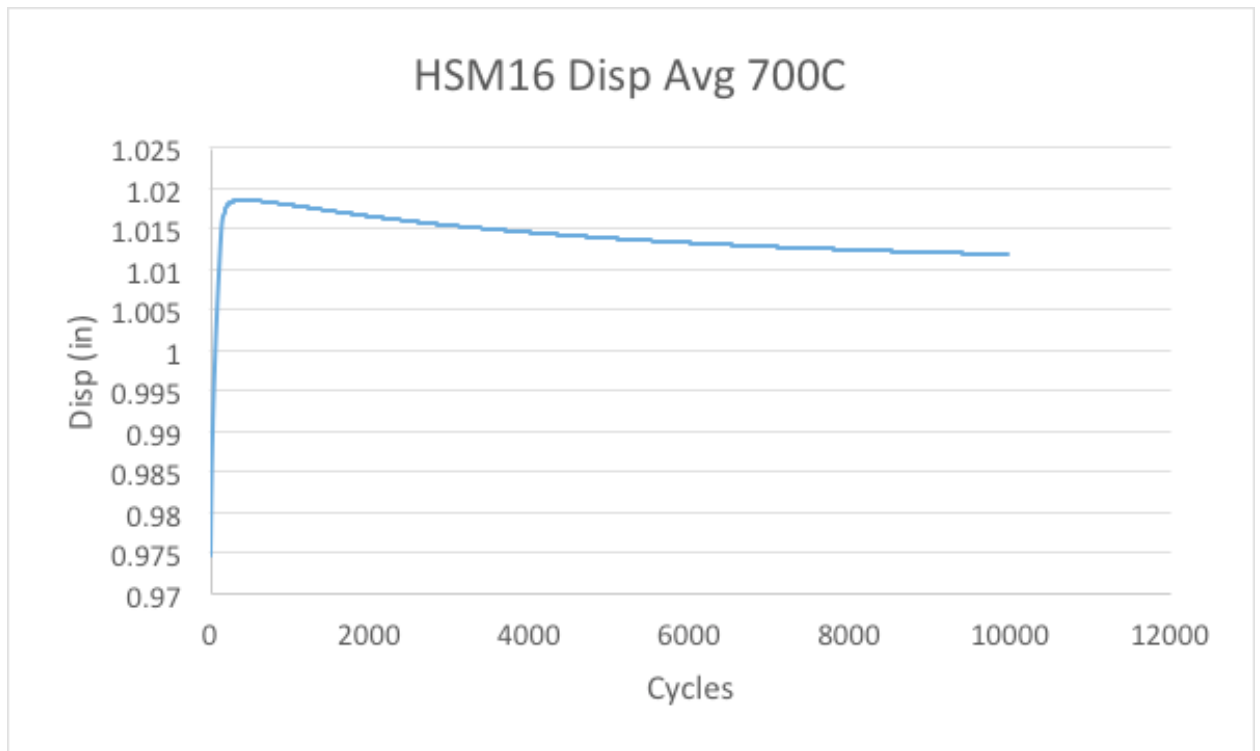


Figure 63. HSM displacement change over time at 700 °C 10,000 cycles

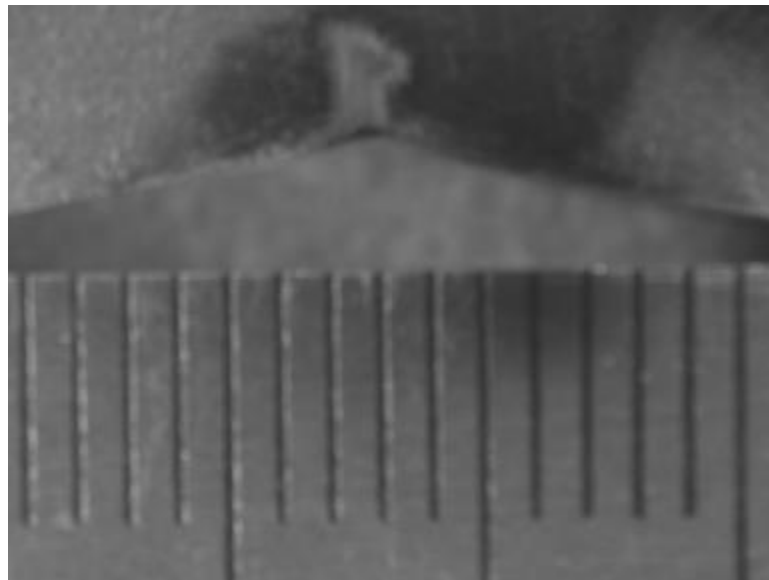


Figure 64. Deflection of 50HS 700 °C sample after fatiguing (scale is in mm)

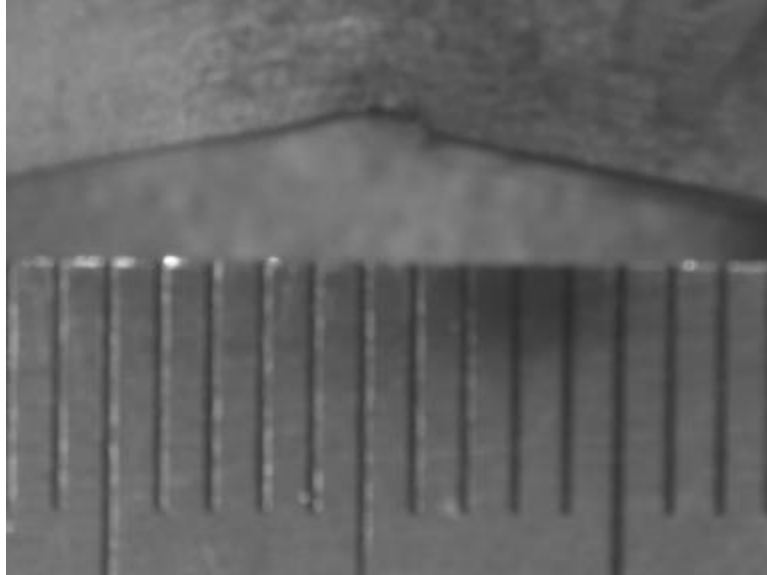


Figure 65. Deflection of HSM 700 °C sample after fatiguing (scale is in mm)

When looking at the microstructure of these two alloys there is clearly evidence of yielding, based on the shape of the grains and the nodules. Figure 66 below was taken at the center of the sample on the outer radius of the bend. There is a cigar shape to the graphite nodules, and to the grains closest to the bend. As mentioned in section 4.2, there is a certain amount of scale and oxidation on the outer edge of the sample, as evidence in the figure below.

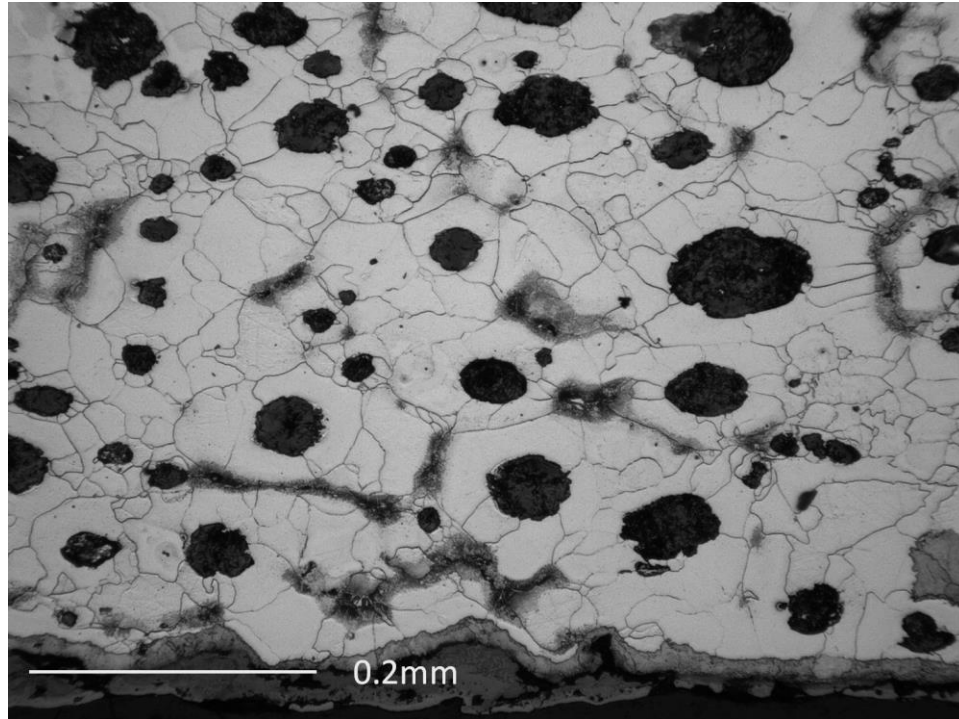


Figure 66. 50HS114 200X Center 700C. Bend location is at the bottom middle of the image

The microstructure of the HSM sample (Figure 67) also shows the elongation of the graphite nodules, and to a small degree, the grains. There is also an additional formation of a carbide phase developing in the microstructure, similar to what was observed in the 600 °C testing and also noted in section 4.2. Of interest is the formation of a crack in this sample, (magnified image in the lower right hand corner of the figure) which has been captured apparently shortly after initiation. It is believed that the crack initiation comes about due to the alignment of nodules. (A composite image of the HSM sample at 700 °C, taken from outer to inner radius of the bend can be found in Appendix C)

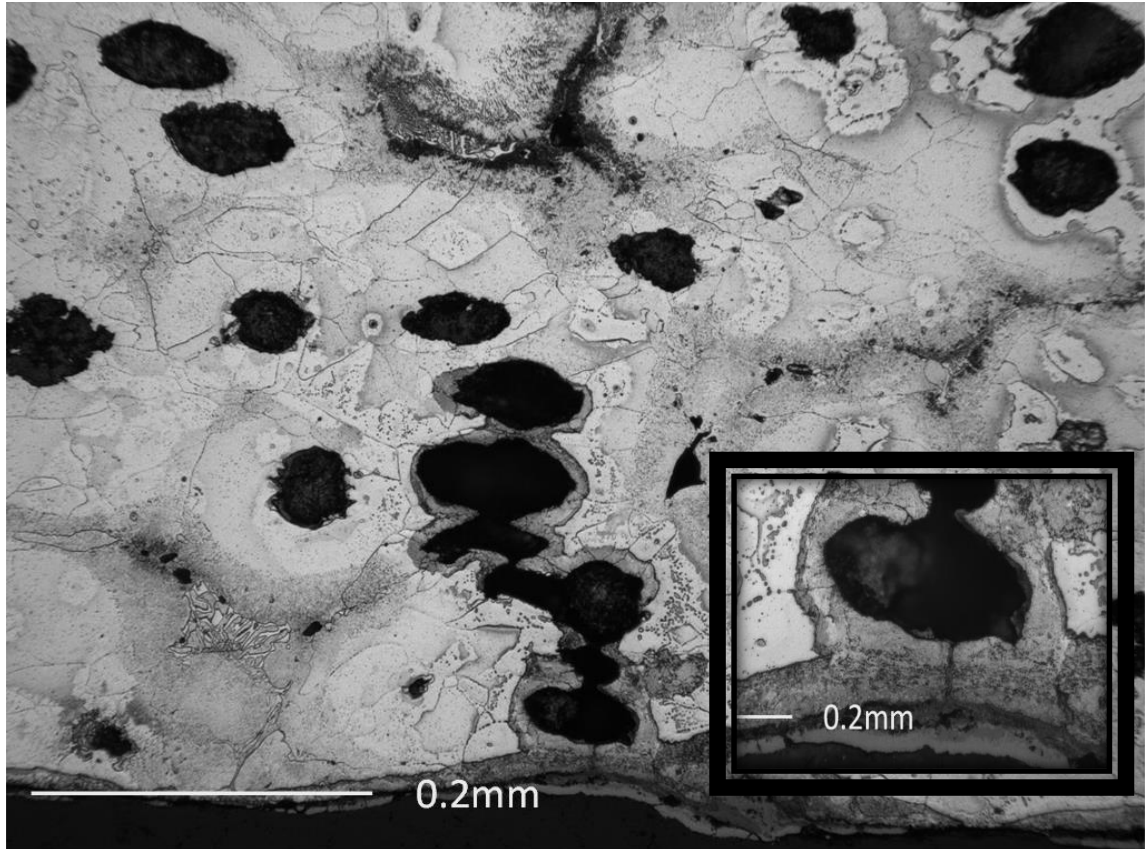


Figure 67. HSM14 200X Center 700C

Of special interest in the micrograph of HSM at 700 °C is a secondary layer surrounding the graphite nodules at the point of fracture (see close up in lower right hand corner of micrograph). As was discussed in Section 2.9, the formation of scale can form on the surface of the material. As the scale is continually cracked during cyclic loading, allowing the ingress of Fe_2O_3 to form on the grain boundaries, further weakening the material [102 – 106].

4.7.2 Flexural calculations

As mentioned at the beginning of this section, testing was not possible in the desired mode of “Position Control”. Operating in “Load Control” allowed for

the collection of the cycle count (time), the minimum and maximum position of the actuator, and the minimum and maximum load. From these limited measurements, it was possible to calculate the changes in flexural stress (Equation 12), the flexural strain (Equation 13) and the flexural Modulus (Equation 14) for each alloy at each of the four temperatures used.

$$\sigma_f = \frac{3FL}{2bd^2} \quad (12)$$

$$\epsilon_f = \frac{bDd}{L^2} \quad (13)$$

$$E_f = \frac{L^3m}{4bd^3} \quad (14)$$

σ_f = Stress, (MPa)

ϵ_f = Strain, (m/m)

E_f = flexural Modulus of elasticity,(MPa)

F = load at a given point on the load deflection curve, (N)

L = Support span, (m)

b = Width of test beam, (m)

d = Depth of tested beam, (m)

D = maximum deflection of the center of the beam, (m)

m = The gradient (i.e., slope) of the initial straight-line portion of the load deflection curve,(P/D), (N/m)

For each of the three equations above, calculations were made based on the experimental data collected and the results are shown plotted in the figures below. The data plotted represents one sample for each calculation for each of the alloys used.

The calculated flexural modulus for each alloy does exhibit a decrease in value as temperature increases as is expected. While the data was good at temperatures in the range 22°C to 600°C, at a temperature of 700 °C the

samples were seen to yield, resulting in plastic deformation and bending of the samples to the point where the ends of the sample are butted up against the upper bend fixture. This results in a much higher unrealistic value of the modulus than is evident for the three lower temperature fatigue tests and makes the data unsuitable for further calculations. In looking at the plot of the modulus for the 50HS alloy (Figures 68 and 69), it can be seen that the data for the 600 °C modulus places it in-between the data for the 22 °C and 400 °C lines. This was a result of the behavior of the material during the fatigue test as also evidenced in the plot of the flexural strain (Figure 74).

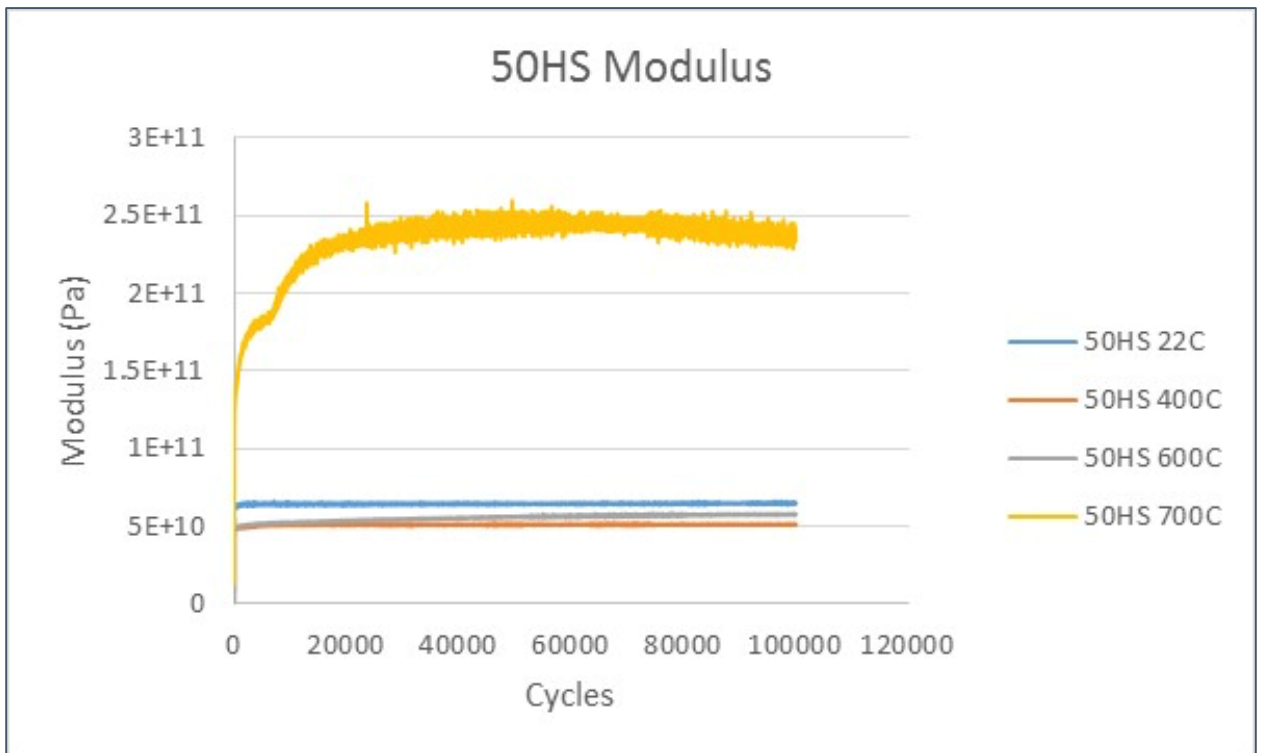


Figure 68. Flexural modulus for alloy 50HS at each of the four fatigue temperatures

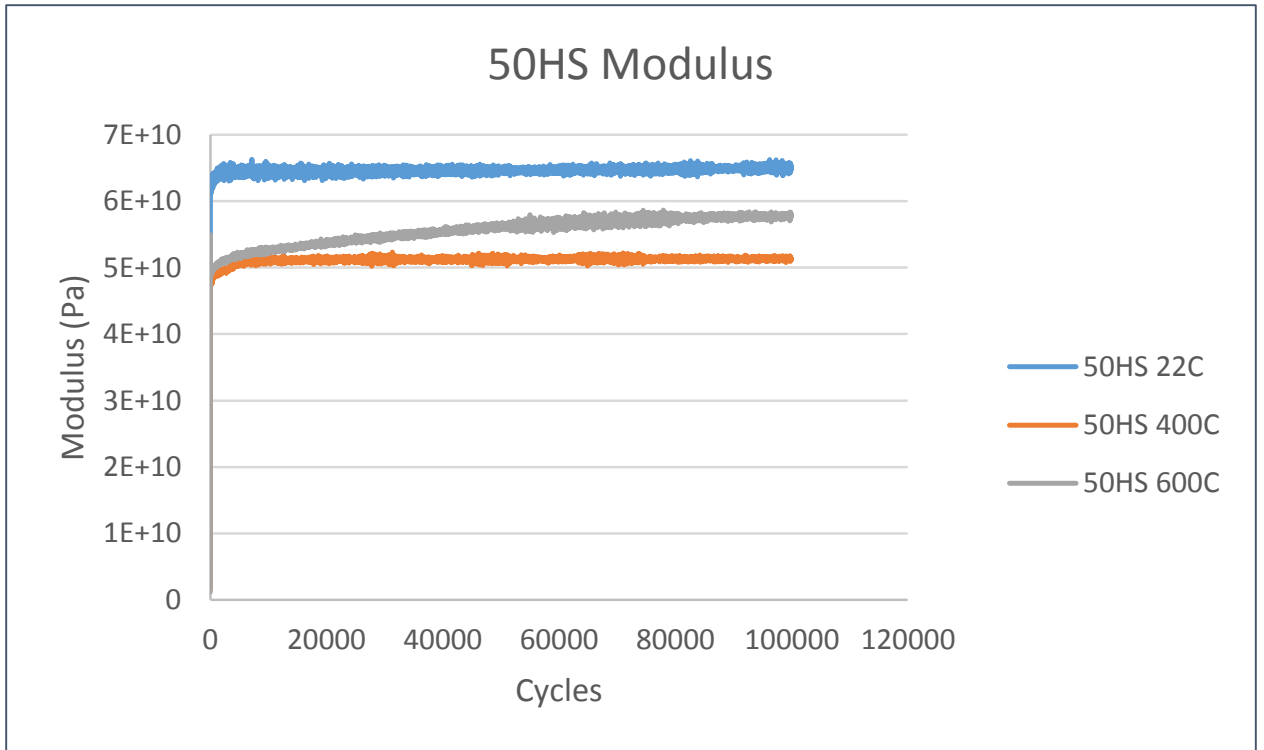


Figure 69. Flexural modulus for alloy 50HS at three of the fatigue temperatures

The effect of temperature on the change of the modulus for the HSM alloy is more evident than for the 50HS alloy, as seen in Figures 70 and 71. While the issue of the 700 °C data remains, there is a nice definition between the different moduli for the three lower temperature tests, showing the decrease in value as temperature increased.

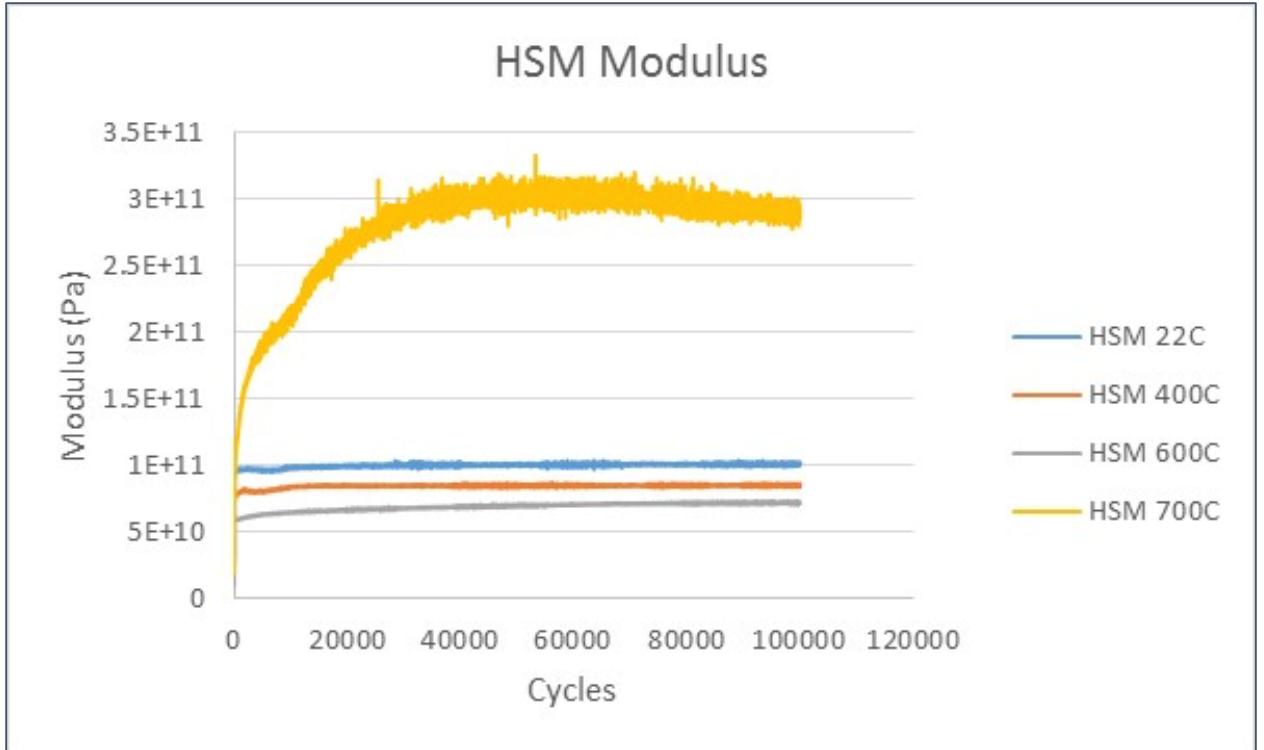


Figure 70. Flexural modulus for alloy HSM at each of the four fatigue temperatures

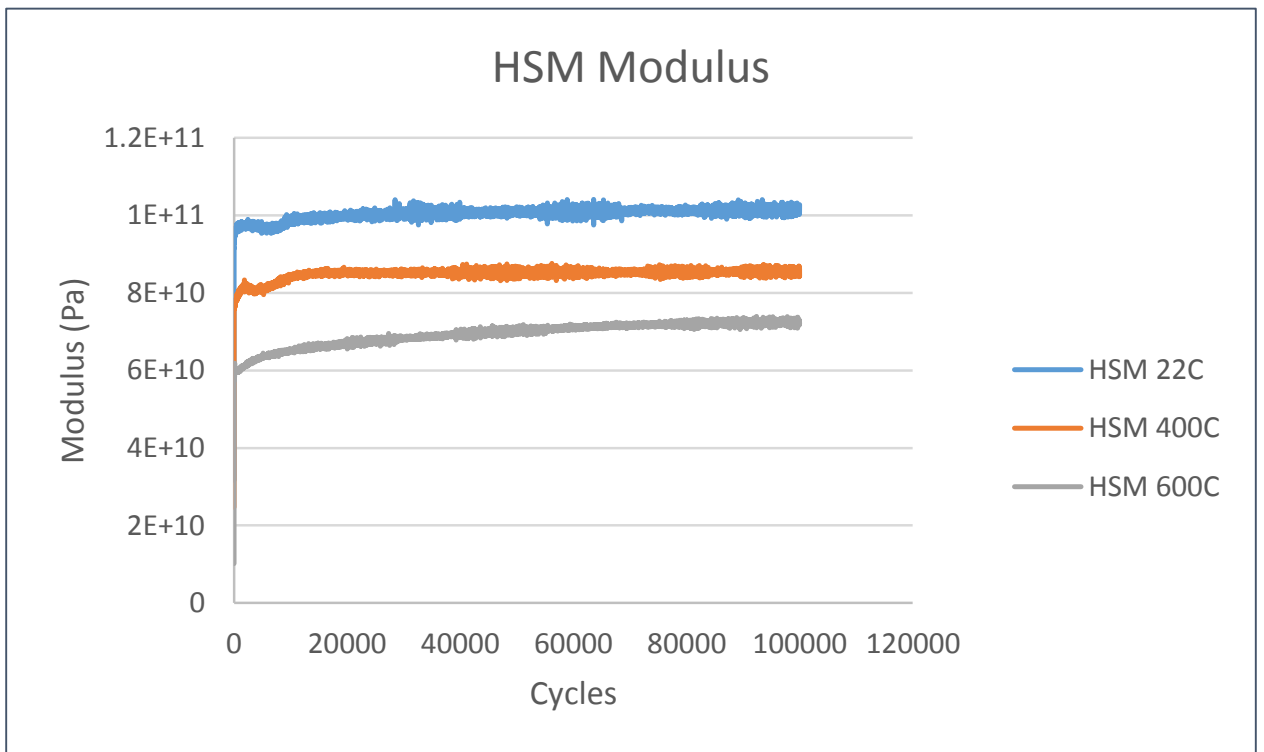


Figure 71. Flexural modulus for alloy HSM at three of the fatigue temperatures

In comparing the moduli values between the two alloys, it can be seen that the HSM alloy has a higher modulus, which is in line with all the other experimental work done.

Because all of the tests were run with constant minimum and maximum load, the stress values for each of the four temperatures was constant for that alloy's calculated mean and amplitude loads. Since the only variable in Equation [12] is load, it is within reason to assume that the stress would remain constant throughout the testing phase. This is represented in Figures 72 and 73 below.

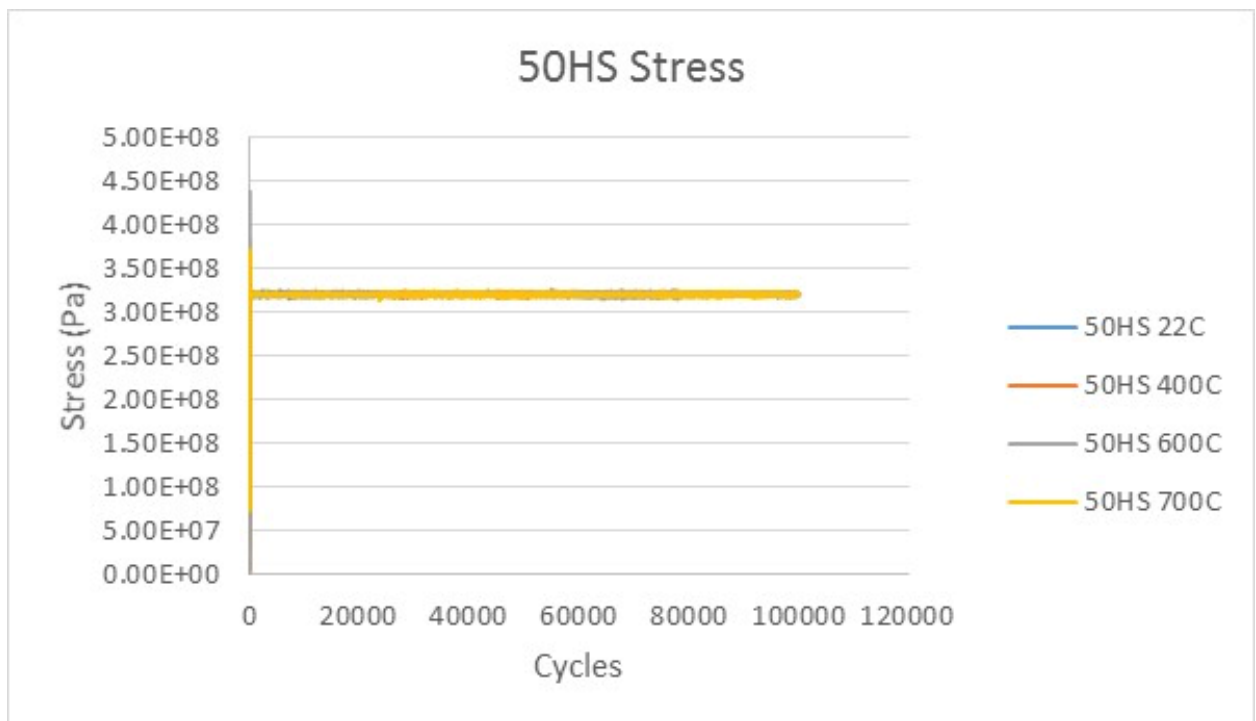


Figure 72. Flexural stress for alloy 50HS at each of the four fatigue temperatures

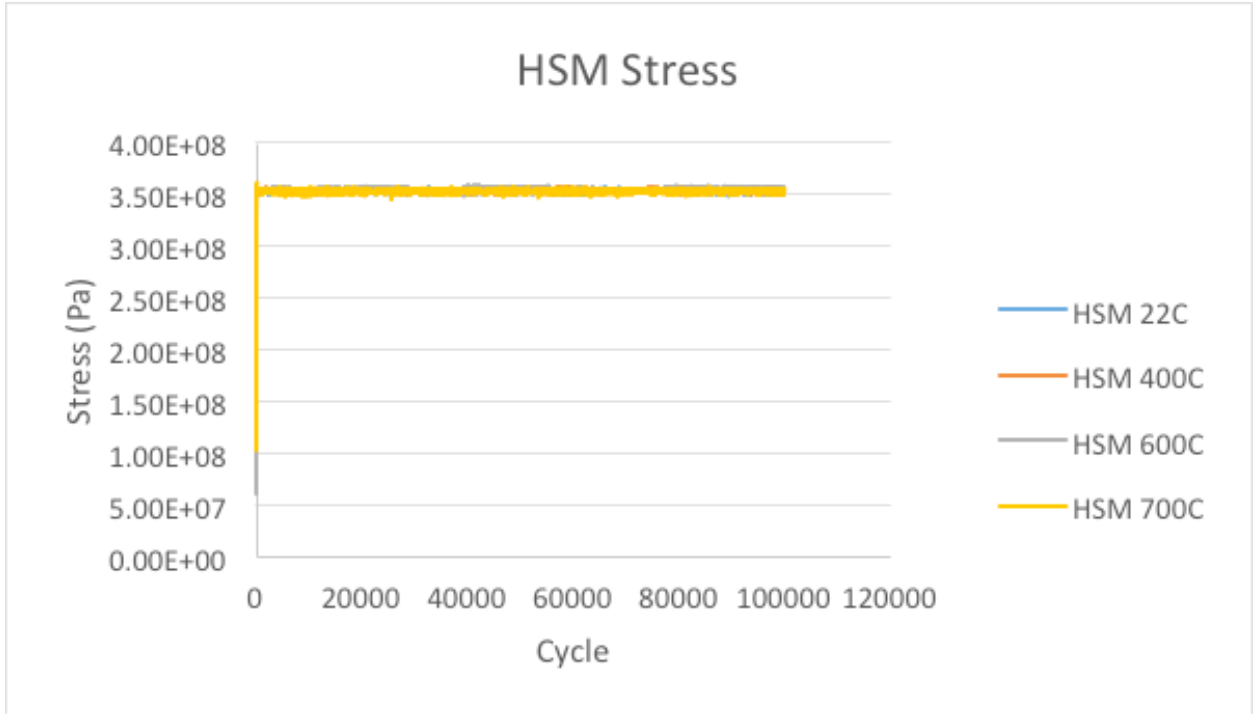


Figure 73. Flexural stress for alloy HSM at each of the four fatigue temperatures

The values of the strain for the alloys corresponds to the change in position of the actuator. As can be seen in the Figure 74 for the 50HS alloy, the values for strain are increasing with temperature, particularly for the 22 °C and the 400 °C temperatures. The values of the 600 °C and 700 °C strain are effected by the creep and yield that occurred at these temperatures respectively during the test. For the 600 °C test for 50HS, the initiation of creep did not occur immediately, but shortly after the 10,000 cycle mark.

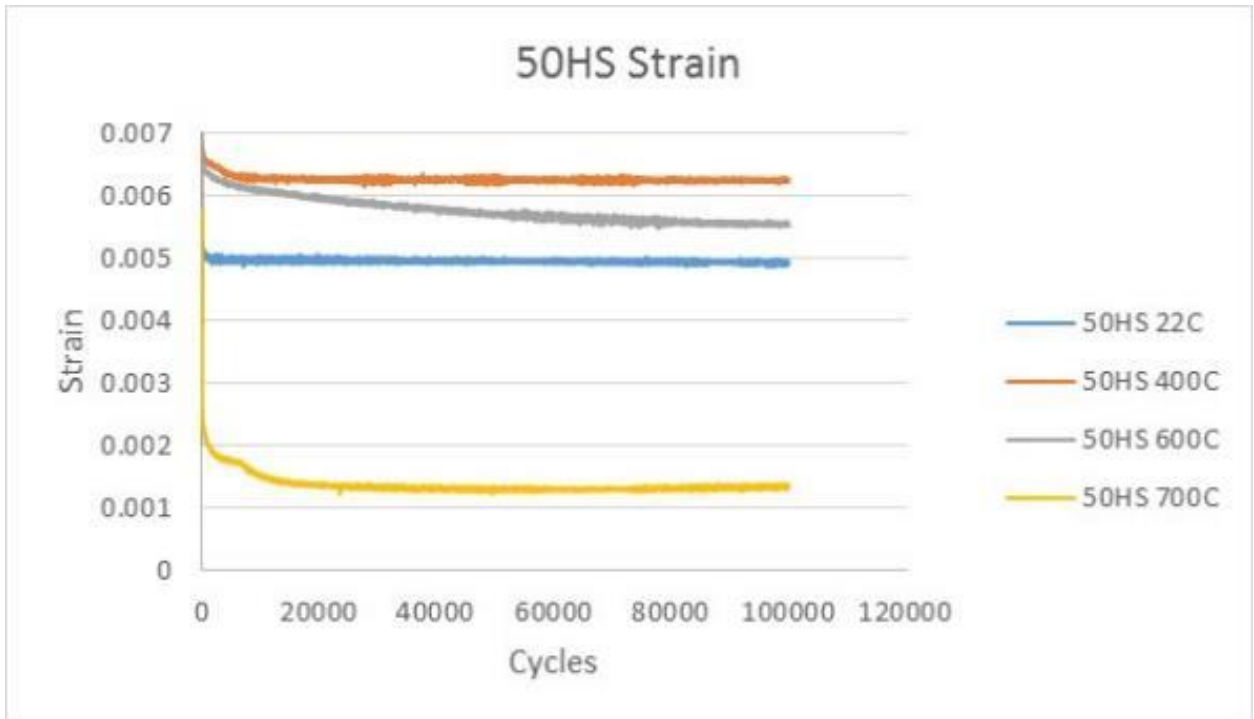


Figure 74. Flexural strain for alloy 50HS at each of the four fatigue temperatures

The strain for alloy HSM was consistent with what is expected after looking at the flexural modulus figures previously. As seen in Figure 75 below, for each of the three lower temperatures, the amount of strain is increasing with temperature. Although the 600 °C temperature did experience the onset of creep somewhere between 15,000 and 20,000 cycles, it was not to the extent of the 50HS alloy.

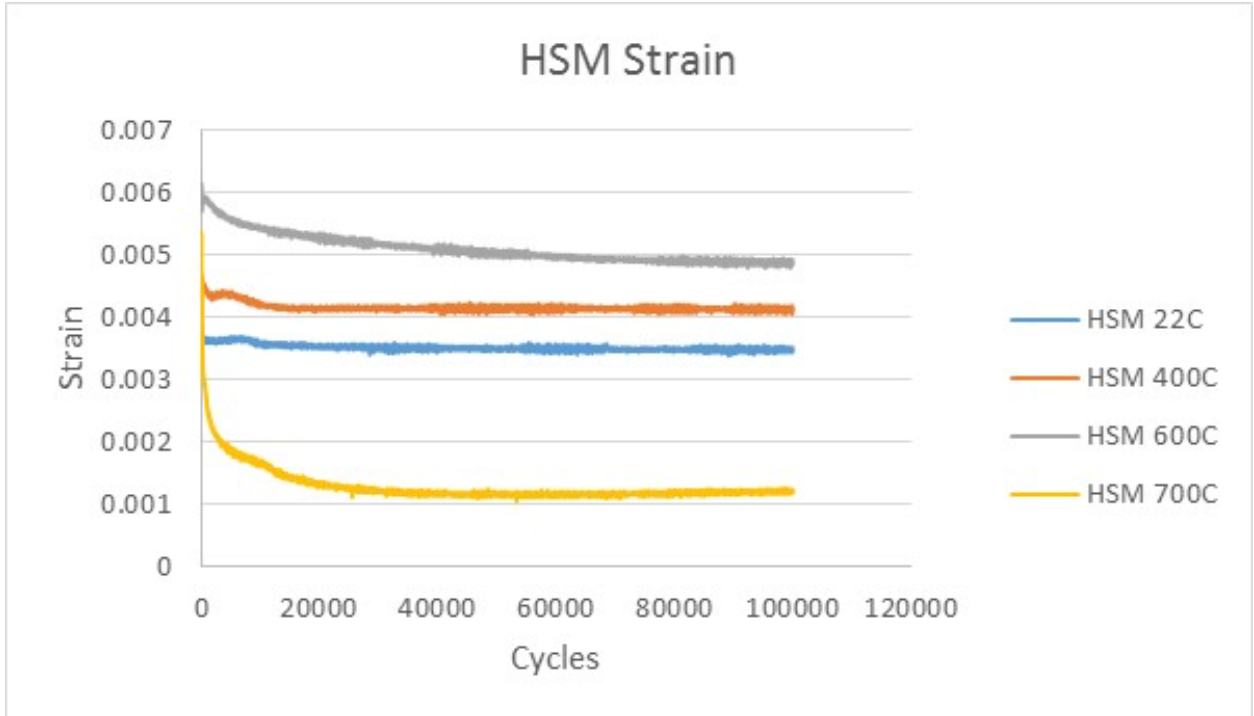


Figure 75. Flexural strain for alloy HSM at each of the four fatigue temperatures

4.7.3 Model curve fit

A general curve fitting model was used which attempts to fit curves for the fatigue of cast iron while under load at various temperatures from this experimental work. For the purposes of model fitting, only the three lower fatigue temperatures were considered.

In order to fit the moduli for each of the alloys, a least squares method of fit was used. There were no constraints required for these fits, as the equation required was basically an exponential curve fit.

$$M = M_o \left(1 - e^{-\frac{t}{\tau}} \right) \quad (15)$$

Where M_o represents the amplitude of the modulus change and τ is the time constant over which it changes. The parameters were fit using Matlab and the least squares non-linear function [lsqcurvefit] without constraints; the parameters M_o and τ were assigned to the Matlab workspace variables $x(0)$ and $x(1)$ respectively.

The trials were carried out by applying a sinusoidally varying stress with fixed (compressive) stress offset. The amplitude of the stress variation is less than the offset value, meaning that the specimen is always under compression. By looking at the variation in strain (i.e. the strain difference) with respect to the applied stress, one is able to obtain values of the flexural modulus that really correspond to the absolute state of the material. In this way, the need to take derivatives is circumvented as values of stress and strain can be used directly.

Two separate and distinct cases can be considered when evaluating modulus values. In the first case the instantaneous response of the specimen to the applied stress is considered. In looking at the instantaneous response, the data represents how the material properties are changing, in absolute terms, with the application of cyclic stress. For the 50HS data it can be inferred that the fit for the 22 °C and the 600 °C data only require a linear fit. For the 400 °C data, an exponential fit was used. The variation of the curves at the beginning of the plots shown in Figures 76 and 77 are the result of the calculations of the displacement variable used in the flexural calculations for strain and modulus. The variations represents the rate of change between the initial deflection, and subsequent deflection values when compared to the initial value.

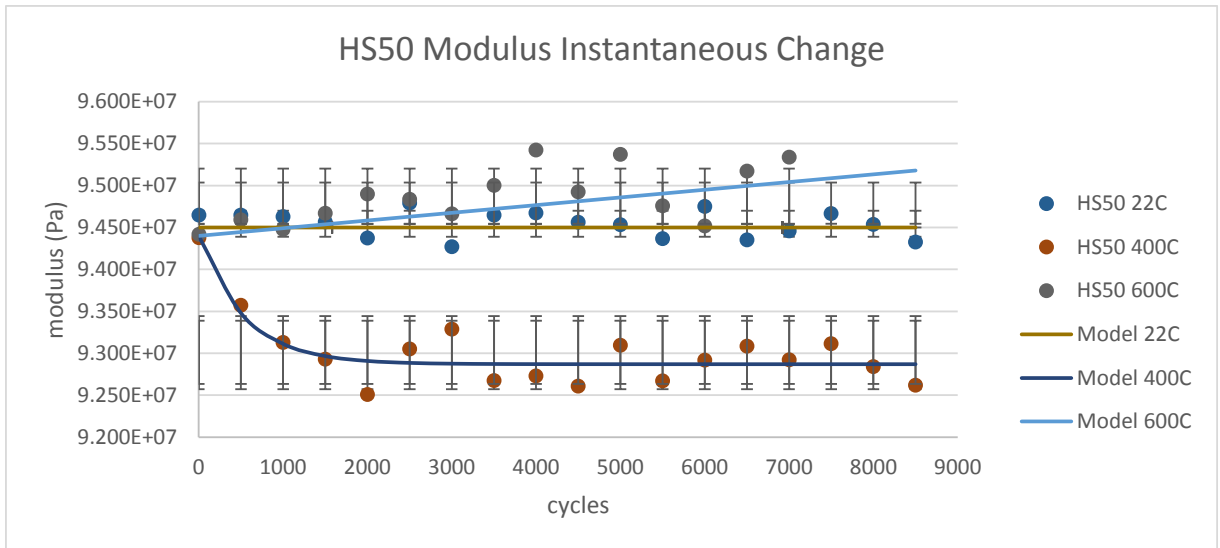


Figure 76. Instantaneous change curve for 50HS

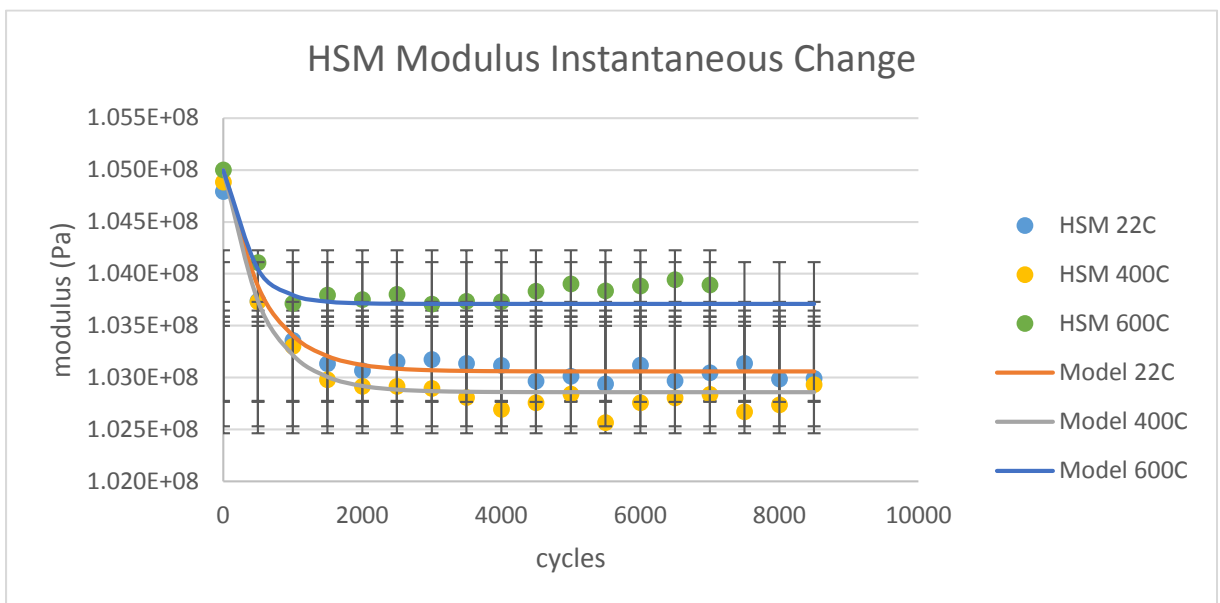


Figure 77. Instantaneous change curve for HSM

In the second approach, the average strain values are used in the modulus calculations; essentially this means that the modulus values will reflect some historical materials data, i.e. the approach is more sensitive to long-term material creep.

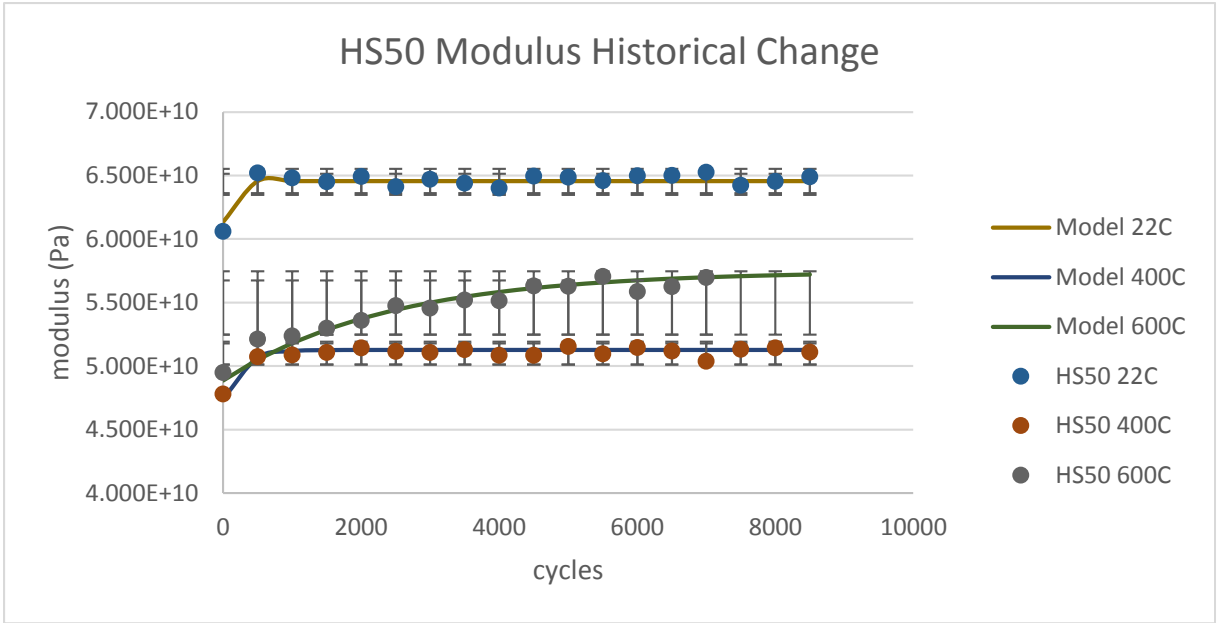


Figure 78. Historical average fit for the 50HS alloy

Figure 78 shows an expected linear response for the 22C and the 400C data, with the exception of the initial cycles. The 600C data is affected by the by creep, as discussed earlier

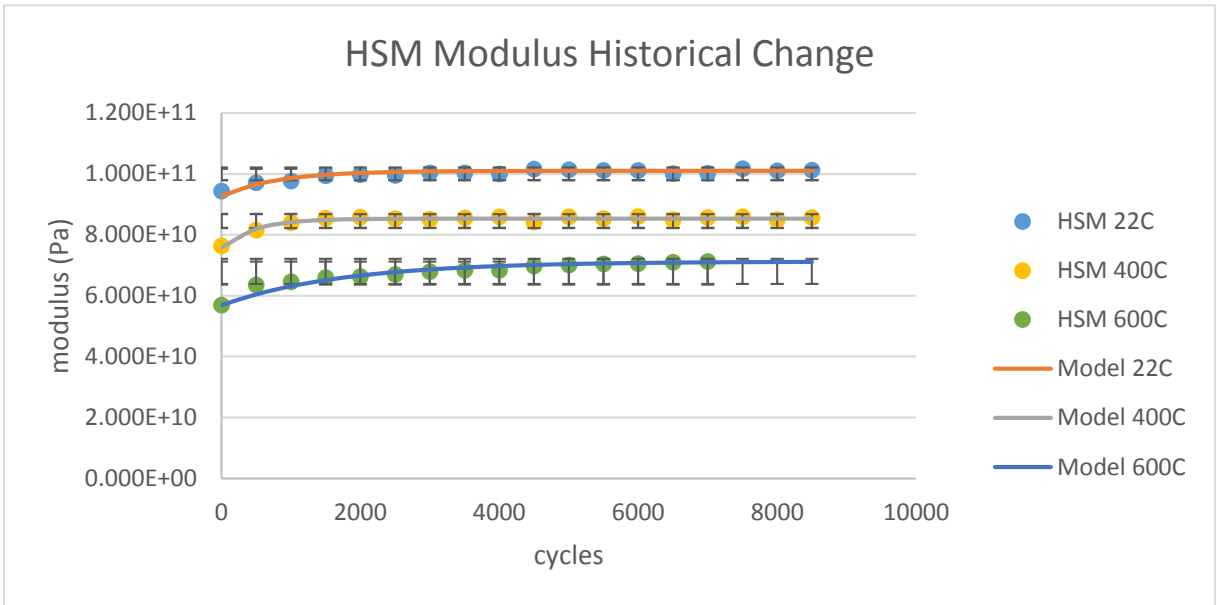


Figure 79. Historical average fit for the HSM alloy

From Figures 78 and 79 above it can be seen that the rate of change in modulus is much faster at the higher temperatures, and this is clearly reflected in the time constant values (τ) of the fitted-parameters, Table 14. Physically, it can be inferred from this that at lower temperatures the action of cyclic fatigue takes longer to affect the material properties. Conversely, at higher temperatures, changes are occurring far more quickly. From what is intuitively known about material properties, these results seem reasonable.

Below in Table 14 are the variables used in the fit of the equation to the theoretical and experimental instantaneous data.

Table 14. Variables used in the curve fit

HSM Historical		HSM Instantaneous		50HS Historical		50HS Instantaneous	
M_o	τ	M_o	τ	M_o	τ	M_o	τ
1.94	582	8.29	814	3.26	68	$y=5.74 \times 10^{10}$	
2.14	561	9.52	487	3.869	269	1.53	544
1.29	370	14.33	1764	8.595	2403	$Y=9.44 \times 10^7$	

CHAPTER 5

DISCUSSION OF RESULTS

In discussion of the results it must be remembered that the material in question, namely, nodular cast iron, can be heterogeneous in microstructure, making it difficult to characterize under the best conditions. The samples received for this work were provided from the keel section of two different casting geometries, which can have several inherent issues such as porosity and inconsistencies within the material due to different cooling rates. In machining samples for this work, porosity was a concern, as several samples were found to have visible porosity. To avoid problems samples used for fatigue studies were examined by radiography to try and ensure uniformity. Along with the inconsistencies found within the samples, there were several issues with the dynamic testing equipment used for the fatiguing process that limited the amount of data available for analysis. Chiefly among them was the inability to conduct the fatigue tests in position or “stroke” control. When working with the manufacturer of the load frame to try and solve this problem, the decision was made to run the system in load control, with an external extensometer mounted to both the load frame and actuator to provide a very accurate recoding of the displacement during the testing process. The restriction to operate in Load control limited the amount of information available for analysis, primarily differing load amounts corresponding with different displacements. The data that was available, minimum and maximum load, minimum and maximum displacement

and cycle count provided for some very useful information about the condition of the material while undergoing high temperature fatigue. In order to develop any sort of model to predict the change in material properties as it undergoes fatigue at high temperature, there must first be an understanding of the basic properties of that material. A considerable amount of background work was completed prior to the fatigue processing, which was necessary in order to better predict the behavior of the material while under load and at high temperatures.

5.1 Effects of the addition Mo and Si to the cast iron matrix

Knowing the chemical composition of the two alloys is important if one is going to predict the behavior of the alloys while under stress. This is especially true for the fatigue work for this research since it was done at high temperatures, a very difficult feat in and of itself. A common way of predicting behavior in steel alloys is by determining the carbon equivalency (CE) of each alloy. This equivalency is used to take into account contributions of alloying elements with respect to their contributions to the properties generally created by carbon. There are essentially three ways to determine carbon equivalence for cast iron based on simple percent calculations shown in Table 15 [120].

Table 15. Formulas used for CE Determination

Formula #1	$CE = \%C + 0.33(\%Si) + 0.33(\%P) - 0.027(\%Mn) + 0.4(\%S)$
Formula #2	$CE = \%C + 0.33(\%Si)$
Formula #3	$CE = \%C + 0.33(\%Si + \%P)$

For determination of the CE, knowledge of certain element percentages was required. For this study the elemental contribution is shown in Table 16.

Table 16. Elements required for CE Determination

	%C	%Si	%P	%Mn	%S
50HS	2.885	3.642	0.025	0.260	0.002
HSM	2.490	4.319	0.021	0.218	0.004

Although each of the three formulas for CE calculation is slightly different, the results based on the percentage of the alloying elements is very similar as can be seen in Table 17.

Table 17. Results of CE Determination

	Formula #1	Formula #2	Formula #3
50HS CE %=	4.089	4.087	4.095
HSM CE %=	3.918	3.915	3.922

Cast irons with a value below 4.3% (hypoeutectic) are considered higher in strength due to the size and shape of the graphite nodules and a more refined grain structure. Based on the results shown in Table 17, it was expected that the HSM alloy would have a higher tensile strength, with its CE value being lower than that of the 50HS. Alloys with a higher CE value tend to have a reduction in strength, larger amounts of coarse graphite nodules and more ferrite is expected. Given the results of the testing done, this matches the expected results. We saw this hold true in the high temperature work as well, given the microstructure shown in previous sections, and discussed later in this chapter.

A comparison of the hardness measurements as related to different microstructures is shown in Table 18. By looking at this table, it can be concluded that the HSM alloy has more pearlite in it than the 50HS, based on its hardness values. This agrees with the results seen in section 4.3, where micrographs were presented showing the HSM alloy, with greater amounts of Mo and Si, contain more pearlite and intermetallic, and less ferrite than the 50HS alloy.

Table 18. Comparison of Microstructure to Hardness Values (RB) (Typical grade refers to the type of cast iron)

<u>Typical Rockwell B Hardness for Ductile Iron*</u>		
<u>*www.Mid-AtlanticCasting.com</u>		
<u>Matrix Structure</u>	<u>Rockwell B</u>	<u>Typical Grade</u>
<u>Ferrite</u>	<u>81 - 91</u>	<u>60-40-18</u>
<u>Ferrite + Pearlite</u>	<u>87 - 95</u>	<u>65-45-12</u>
<u>Pearlite + Ferrite</u>	<u>91 - 102</u>	<u>80-55-06</u>
<u>Pearlite</u>	<u>96 - 104</u>	<u>100-70-03</u>
<u>Acicular or Banite</u>	<u>103 - 110</u>	<u>120-90-02</u>
<u>Tempered Martensite</u>	<u>110 - 120</u>	<u>120-90-02</u>
<u>Austenite</u>	<u>78 - 84</u>	<u>High Alloy</u>

Along with the microstructure estimations, there are also estimations of the tensile strength based on the determined hardness values [121]. Table 11 and Figure 39 shown earlier illustrate the comparative anticipated tensile strengths based on the initial hardness values experimentally determined. Based on Table 11 and Figure 39 it was anticipated that the HSM alloy would have a greater tensile strength and a higher yield value for the fatigue process due to the addition of Mo, which proved to be the case. This relationship is, however, dependent on the shape of the graphite nodules which is aided by the addition of

Si, and whether there is the formation of carbides, which Mo has a tendency to do at higher temperatures. Table 19 below shows a relationship between hardness values and average tensile values.

Table 19. Comparison of Hardness to Tensile Strength*

*<http://www.mwsco.com/kb/articles/19990630e.htm>

Typical Tensile Strength for Rockwell Hardness (RB)				
	50HS		HSM	
<u>Temp</u>	<u>Hardness (RB)</u>	<u>Tensile (ksi)</u>	<u>Hardness (RB)</u>	<u>Tensile (ksi)</u>
<u>RT</u>	<u>88.1</u>	<u>87</u>	<u>97</u>	<u>110</u>
<u>700</u>	<u>86.3</u>	<u>83</u>	<u>91.8</u>	<u>95</u>
<u>800</u>	<u>87.1</u>	<u>85</u>	<u>95.4</u>	<u>104</u>
<u>900</u>	<u>92.8</u>	<u>95</u>	<u>103</u>	<u>128</u>

Although the final grain size was not identical for both heat treatments, both alloys showed a similar trend of an increase in grain size due to the addition of Si. What is notable about the size of the grains is that as the temperature increases there seems to be a general increase in the grain size up to 800 °C, apart from the 700 °C temperature. At 700 °C there is a decrease in the grain size for both heat treatments. This seems unusual since one expects the size of the grain to increase with increased temperature. Since 723 °C is a transition line between phases according to our phase diagram, the samples may have been close to this point in the heat treatment, which could account for the grain size effect. For the 900 °C heat treatment for both alloys, the amount of pearlite formed precludes the determination of actual grain size for that temperature.

As was discussed in Section 2.4, the formation of oxides or scale is dependent on the contribution of the alloying elements in the matrix. The amount

of scale formed on the samples shown in Section 4.2 shows evidence that the greater amount of silicon added to the HSM sample reduced the amount of scale produced during both types of heat treatments. This scale formation was also evident in examination of the microstructure taken from the temperature fatigued samples. The HSM alloy had an almost 17 percent increase in the amount of silicon added to that alloy. The amount of chromium added to the 50HS alloy was approximately 25% greater, which may explain the formation of a greater amount of outer scale in the 50HS samples than on the HSM alloy. On an overall comparison of the two alloys over the different heat treatments done in the study, 50HS had an average scale three times thicker than seen for the HSM alloy.

One of silicon's primary contributions after oxidation resistance is in the forming of graphite nodules. In looking at the number and size of the nodule formation, visually it can be seen that the HSM alloy has fewer and smaller nodules, than the 50HS alloy. There are a number of factors that might provide reasons for this, such as mold size, amount of time spent in the mold while cooling, and the elemental composition. In looking at the size of the samples (Fig. 7) the 50HS samples were much thinner than the HSM samples, which may have resulted in a higher cooling rate. It is important is to examine the change in nodule size and number as the temperature of the heat treatments increased. For the HSM alloy, as the temperature increased the size of the nodules generally increased and the number of nodules decreased. This indicates that there is diffusion of the carbon from the smaller nodules to coalesce into larger nodules (this was shown in the previous chapter for the HSM 700 °C image).

This reduction in nodule number would lead us to an interpretation of higher strength due to the lower number of the softer graphite nodules. For the 50HS alloy, there does not seem to be the same trend as seen for the HSM alloy. As the temperature increased for 50HS, the relative size of the nodules did not change drastically, nor did the nodule shape differ from spherical as much as was observed for HSM. This greater number of nodules should lead to a prediction of lower material strength, and greater ductility. This was also evidenced in looking at the fatigue results of the alloys. The HSM alloy had one sample failure at the 600 °C temperature, and the initiation of a crack at the 700 °C temperature. The Hall-Petch equation addresses the refinement of grain size leading to stronger materials [122] and it appears that the same relationship might apply to this material as well. The comparison of nodule sizes can be seen in Table 20.

Table 20. Nodule size relative to temperature

HSM				50HS			
Temperature (°C)	Size (µm)		Size (µm)	Temperature (°C)	Size (µm)		Size (µm)
22	38.39			22	14.73		
600	60.93			600	44.71		
700A	44.71	700AA	48.09	700A	40.33	700AA	30.81
800A	38.14	800AA	74.52	800A	30.68	800AA	34.57
900A	63.12	900AA	66.63	900A	35.32	900AA	24.98

The noticeable difference in nodule amount and size also correlates to the differences in velocity of both the longitudinal and shear waves measured during the ultrasonic tests.

5.2 Mechanical testing

Tensile tests done to determine the yield strength for the alloys (needed in the fatigue portion of the test) showed that the 50HS alloy had a lower yield point and lower tensile strength than the HSM alloy. This is primarily due to the addition of Mo, which aids in the strength of the material, particularly at higher temperatures. The 50HS alloy displayed necking during the plastic portion of the test, allowing for use of the standard 0.02 percent offset method in yield strength assessment. The HSM alloy exhibited little necking during the tensile test. This made the estimation of the strength needed for the fatigue testing challenging, and may have led to a lower estimation of the UTS, but the values determined and used still enabled successful fatigue tests to be carried out. It was noted that the HSM alloy fractured closer to the end of the gauge section than the 50HS alloy. There was no obvious reason for the different location of fracture.

In looking at the results of the fatigue tests from the aspect of temperature effects, it was observed that an increase in temperature results in an increase in creep of the samples at or above 600 °C. Evidence of creep is seen in the plots of the position data from Figure 80 below.

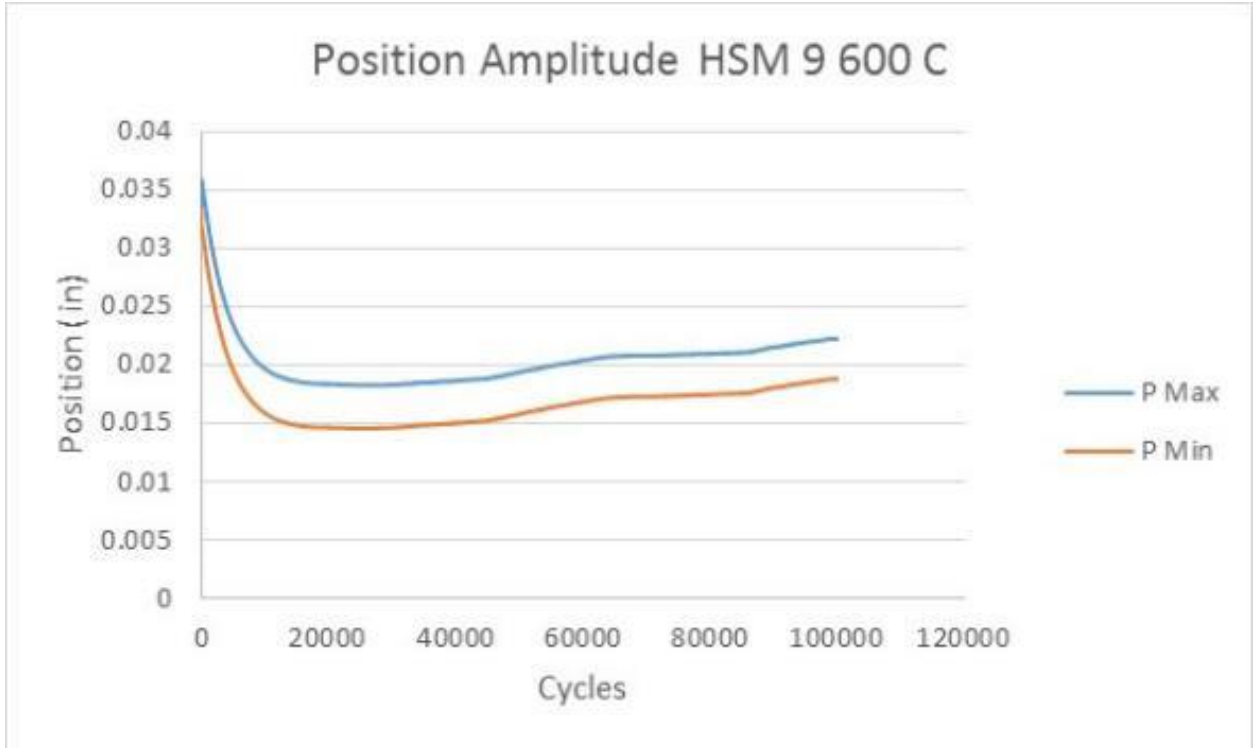


Figure 80. Position minimum and maximum for HSM9 at 600 °C

From Figure 80 it can be seen that there is an elastic spring-back in the minimum and maximum position of the actuator resulting from the minimum and maximum loads applied throughout the testing process. If there were yielding instead of creep, there would not be this elasticity in the sample as the load was applied and removed. This behavior was typical of all the samples fatigued. This was verified by examination of the microstructure of each fatigue sample. Those samples at the higher temperatures did show an elongation of the grains in the direction of the tensile load, but little effect was seen for the portion of the sample under compression (See Appendix C).

For the samples fatigued at 22 °C and 400 °C, there were some interesting differences in the alloys. The HSM sample performed well, with the amplitude of the position remaining constant throughout the testing process. However, the 50HS alloy showed several interesting points when looking at the data in a more narrow fashion. There are several different regions during the testing where different phenomenon may be occurring. Each of these regions is identified in Figure 47 below, and are addressed individually. In the latter half of the first region (1) there appears to be some sort of deformation, thought to be due to the pins in the bend fixture setting into the sample, particularly if this sample contained a region softer than the other samples tested. The second region of the test (2) indicates a stiffening of the material. In the third region of the test (3) there is resemblance to crack growth however there did not appear to be a visible crack on the outside of the sample when examined. The fourth region of the sample (4) looks reminiscent of low carbon steel yield point phenomenon in a tensile test, but one cannot be sure of the exact nature of the event. The author is confident that the drastic change in displacement is not due to clip gauge slip of the extensometer used to monitor position, but a real material effect.

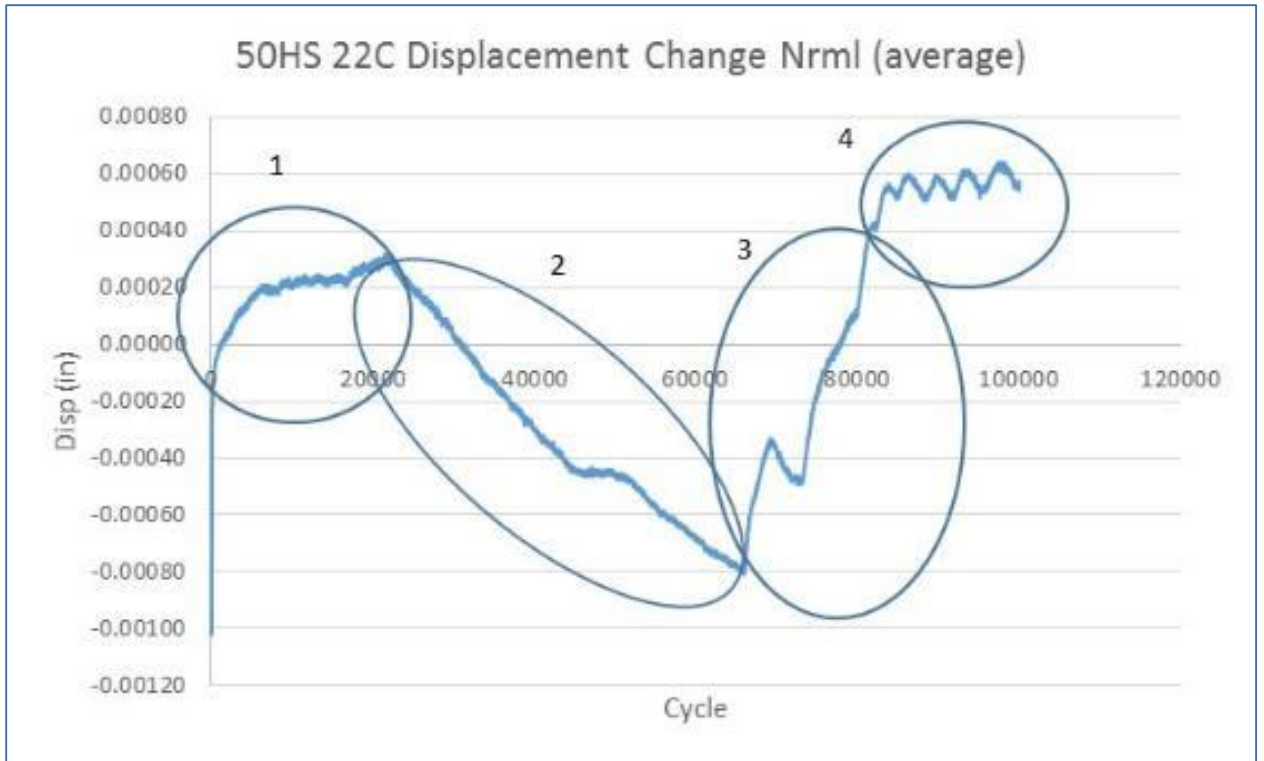


Figure 47. Dislocation change average at a smaller scale

The trend of samples fatigued at the 400 °C and 600 °C temperatures showed a decrease in the position of the actuator during the first 20,000 cycles of the tests. This is believed to be a combination of two factors: a small amount of hardening may be going on during this time, and there may be a bit of thermal expansion occurring during the initial portion of the tests. The hardening may be the result of precipitate hardening, such as Mo carbides. Molybdenum can form carbides at the grain boundaries and in pearlite at high temperatures [57, 73, 74], which when formed are stable and aid in strength of the matrix. In Figure 81 below there appears to be the formation of precipitates near the grain boundaries, and also intermixed in the pearlite.



Figure 81. Possible formation of Mo carbides in HSM after 600 °C fatigue test

The thermal expansion is thought to have been the result of the expansion of the Inconel 718 rods used inside the furnace to hold the bend fixtures. The process for the testing was to place a small load (approximately 20 pounds) on the sample to maintain contact with the sample during the time the furnace ramped up to desired temperature. Once the furnace reached the desired operating temperature, the fatigue process began. The amount of expansion for one Inconel 718 rod can be up to 0.064 inches (given a 12 inch rod). Since there were two rods inside the furnace, one inch in diameter, it is feasible that there

might have been a small amount of thermal expansion still occurring at the time when the testing began.

As mentioned earlier in this discussion, the results for the 700 °C work was not considered in any of the flexural calculations or fitting of the curves as each alloy showed an extensive amount of yielding at this high temperature. Because of the exhibition of yielding at 700 °C, no testing was carried out beyond this temperature. It was felt that no additional useful information would be gained, and it would not be worth the risk of possible damage to either the furnace or the load frame. Although the recorded data for each temperature did not appear to behave exactly as anticipated, it was noted that the data recorded was repeatable for the given temperature and alloy.

The values for the flexural modulus calculations showed that, at higher temperatures, the modulus for the alloys decreased. This is shown below in Table 21.

Table 21. *Calculated average Flexural Moduli as compared to Ultrasound and Literature Values*

	Experimental		Ultrasonic Estimation		Literature Values	
	50HS	HSM	50HS	HSM	50HS	HSM
22 C	64.6 GPa	100.4 Gpa	173.6 Gpa	176.4 Gpa	160 -180 Gpa	
400 C	51.2 Gpa	84.9 Gpa				
600 C	55.5 GPa	69.4 Gpa				
700 C	234.0 Gpa	278.8 Gpa				

The experimental values for the moduli for both alloys is less than literature values, and for those values experimentally determined in the ultrasonic tests, but are believed to be valid. Typical moduli values for cast iron range from

160 GPa to 180 GPa at room temperature. The best value for the modulus was with the HSM alloy, showing a value of approximately 100 GPa. It is believed that the reason for the difference from the literature values comes from the fact that experimental values were done in three point bend, where both a compression force and a tensile force is experienced by the sample. It is understood that literature values are derived in tension tests.

Although the values for the flexural modulus from Table 19 are not to the same magnitude as those of the ultrasonic measurements or literature values they do represent the anticipated trend of decreasing value as temperature was increased.

5.3 Model estimation

In determining the fitting of an equation for the curves for the modulus for each of the alloys, a Matlab program using a least squares non-linear function [lsqcurvefit] without constraints was employed to examine the curves for the moduli for the temperatures of 22 °C, 400 °C and 600 °C. For the experimental data the following were deduced: the rate of change in modulus is much faster at the higher temperatures, at lower temperatures the action of cyclic fatigue takes longer to affect the material properties, and at higher temperatures, changes are occurring far more quickly

If we look at a comparison of the Uniform Material Law for High Strength Steel (UMLHS) (Equation (5)) to the Uniform Material Law for Cast Iron (Equation (16) below), we can

$$\varepsilon_a = (\sigma'_f)/E * (2N)^b + (\varepsilon'_f) * (2N)^c \quad (5)$$

Where;

ε_a is the strain amplitude

(σ'_f) is the fatigue strength coefficient

E is Young's modulus

N is the number of cycles at endurance limit

b is the fatigue strength exponent

c the fatigue ductility exponent

(ε'_f) is the fatigue ductility constant

see that there are several generalizations made in the UMLCI:

n' an empirically determined value is set to 0.1 instead of being a function of b/c

(σ'_f) becomes a function of the ultimate tensile strength of the material.

(ε'_f) becomes an empirically determined constant

Essentially, the UMLCI simplifies the UMLHS down to three variables, modulus, tensile strength, and number of cycles (for a comparison of UML, UMLHS and UMLCI refer to Table 4). It does not take into consideration the issue of varying stress (the change in load) for a given situation, or temperature. In fact, the UMLCI is really geared towards predicting the lifetime of a component that is subject to standard operational conditions, and in this capacity could be quite useful. However, if one considers how the material properties (modulus) change with load, number of cycles and temperature, the UMLCI was suspected to be inadequate.

In order to determine the appropriateness of the UMCLI, it was necessary to calculate the value of UMLCI (Eq 16) for each cycle (N), using the values of

ultimate tensile strength (UTS) from the tensile test, and modulus calculated from experimental data (E), all taken at room temperature. The graph below in Figure 82 shows that the values calculated for the UMLCI at room temperature are much higher than the values derived from the experimental data. Conversely, assuming a 25 percent decrease in UTS at 400 °C (based on data taken for ductile iron [123]) the UMLCI shows values much lower than the experimental data.

$$\epsilon_a = \left(\frac{1.34*(UTS+208)}{E} \right) (2N)^{\frac{-\text{LOG}\left(\frac{1.34*(UTS+208)}{0.4*UTS}\right)}{6}} + 0.26(2N)^{-0.7} \quad (16)$$

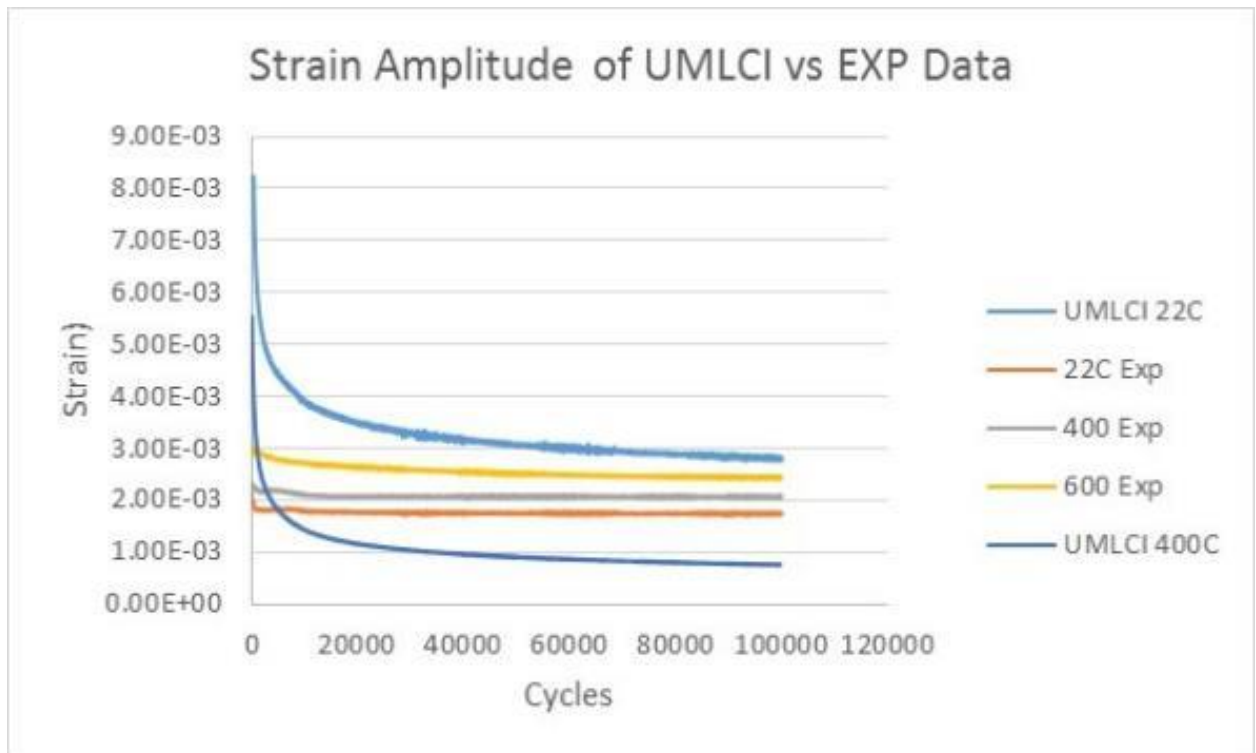


Figure 82. Calculated UMLCI strain amplitude versus experimental values

It can be seen from Figure 82 that when comparing the UMLCI to experimental data, as the temperature of the experimental data is increased, the value of the UMLCI comes closer to experimental data, but there are still issues with this model. With the value of N (number of cycles) combined into the equation it is shown that at low cycle count the calculated value of UMLCI is much higher than experimental values at room temperature. It is predicted that as N were to increase, say to values closer to 1×10^6 , the values of UMLCI would progress lower and fall below experimental values.

It is interesting that all of the experimental data does fall in between the calculated values for UMLCI. This is perhaps due to several factors. In the development of the ULMCI, a method of trial and error was used to determine the constants used in the calculations. If these constants were determined at room temperature, it is reasonable to deduce that they may not be appropriate for higher temperature work, given the decrease in modulus with temperature. The limited amount of literature on this law does not mention exactly how the law was proved to be appropriate for more than the two alloys mentioned in the article, therefore it is also reasonable to assume that it would not be entirely appropriate for the data collected in three point bend.

To try and make this theory more applicable, there are several factors that one needs to take into account:

- Modulus – how does this change with increased temperature? This might be determined experimentally, and then a multiplier be added into the equation where E is placed.
- Tensile Strength – how does this change with temperature? Most sources typically lower the value by approximately 25% for the temperature range used in this study. This too would be best done experimentally then a multiplier (x) be used with the room temperature value.
- Stress – this is not in the original equation, and it can have an effect based on change in temperature. Perhaps a multiplier like $\left(\frac{\sigma}{z*\sigma}\right)$ could be multiplied by the whole equation, with the value of (z) being temperature dependent as well.

This would give us three quantities in the equation that are temperature dependent; modulus (E), tensile strength (UTS) and stress (σ), all using the multipliers of x, y, and z respectively. There is one issue that is not resolved, and that is the value for the number of cycles (N). This is an independent variable difficult to resolve.

Factoring all this into the equation it could look something like what is shown below.

$$\epsilon_a = \left(\left(\frac{1.34 * ((y * UTS) + 208)}{(x * E)} \right) (2N)^{\frac{-\text{LOG} \left(\frac{1.34 * ((y * UTS) + 208)}{0.4 * (y * UTS)} \right)}{6}} + 0.26(2N)^{-0.7} \right) \left(\frac{\sigma}{z * \sigma} \right) \quad (17)$$

In modifying the equation UMLCI for temperature, as shown above it does not take into consideration the nodule factors. This should be taken into consideration since, for nodular cast iron the size and number of nodules can play a role in the fatigue properties of the material.

Given that it was not possible to apply the UMLCI to the experimental data, one then needs to ask the question “Are there any other models out there that this data can be applied to?” As was discussed in Section 2.8, there is very little work available on the fatigue of cast iron at high temperature. Those model that do exist, when broken down, are capable of accounting for one or at most a few of the aspects needing to be considered for high temperature fatigue, or for three point bend fatigue. In a short survey of methodologies that might be appropriate for work done for this study, there were several that may have merit. A brief description follows:

- Those that considered a defect equivalent to a crack

Tankas et al. [124] and El Haddad [125] developed equations regarding the crack tip impedance into grain boundaries, and crack length stress intensity factors. Neither of these is appropriate as they would require the use of micro or threshold stress intensity factors of a crack.

- That a defect is equivalent to a notch

Lukas et al. [126] developed a formula related to the geometric features which are related to the radius of a notch. This approach would require the consideration of the critical crack size of non-propagating cracks

- The use of geometric factors

In this approach Murckami [127], De Kazinczy [128] and Mitchell [129] developed equations relating hardness, area of the stress plane where defects are located, interior and exterior micro shrinkage and geometric features.

From this third approach Costa et al., [77] produced a model that does deal with the properties that are obtainable from a three point bend test, Eq 18.

$$\sigma_f = 1.25H_v(1 - 0.03\varphi_i) \quad (18)$$

Where φ is a normalization factor relating nodule size, frequency and proximity within a sample [130]. This model places emphasis on the location, size and shape of the nodules or casting defects by considering the size, proximity to one another, and the frequency of nodules within an area to derive a normalization

factor (ψ) used in Equation (18) What the model essentially does is examine the cross sectional area of a sample after it was fatigued for 1,000,000 cycles at room temperature. The sample is then cut in half, polished and etched, then the location, size and distance between nodules is recorded. Those values are then placed into the fatigue limit equation.

In looking at the data collected from this study, there are good indications that future continuation of this work could lead to confirmation of Costa's work. Figure 67, from Chapter 4, shows the importance of the effect of nodule size and relative proximity. In the higher inset image there can be seen the formation of a small crack within the cluster of graphite nodule closest to the outer edge of the sample. With some slight modification to the current testing equipment, and Costa's parameters can be made applicable for higher temperature fatigue life estimations. The data Costa used was acquired with a cycle count falling into the realm of high cycle fatigue, which was a factor of 10 higher than the data acquired for this study, with a testing frequency (Hertz) roughly 6 times greater than used for this study. Future continuation of this study would require testing times to be increased and the perhaps the testing frequency increased as well. This would allow for closer comparison to the conditions Costa used during his study. While all of the samples used in the Costa study generated cracking after the long cycle time, only one sample failed during this study with evidence of cracking in one other sample, the sample shown in Figure 79. If this study were modified to run for a longer cycle count, the chances of crack initiation would increase. The final modification to Costa's study would need to deal with the

temperature of the testing. Costa's was done only at room temperature, whereas this study was concerned with fatigue life estimated at high temperature. There may need to be modifications to Costa's work to account for changes in materials properties which, from this study, were seen to change at a faster rate at higher temperatures.

In order to repeat this study in hopes of replicating and validating Costa's work, it would be necessary to upgrade the current testing machine to make it reliable enough to run for several days continuously. In addition to reliability, updated software would be needed in order to be able to capture load values which could be correlated to position values, allowing for stress amplitude and strain amplitudes to be determined. It would also require a more definitive estimation for the decrease in tensile and yield limits for cast iron as temperatures increased. This could be accomplished with the addition of an induction furnace coupled with a load frame used for tensile testing. From this relationship of decrease in value with temperature, there could also be developed a relationship between flexural modulus and Young's modulus. This would allow for easier estimations of properties by means of simplified testing procedures.

CHAPTER 6

GENERAL SUMMARY AND CONCLUSIONS

In this body of work, keel blocks of two alloys of cast iron cut from castings of exhaust manifolds were examined. Elemental composition was determined for each alloy, designated 50HS (high silicon) and HSM (High silicon and molybdenum), and ultrasonic testing was done on the samples to determine the room temperature moduli values. Heat treatments were carried out and the microstructure examined to determine phase percentages as a function of time and temperature. Grain sizing and hardness testing was done for both alloys after each heat treatment, with the values used to make estimations on tensile strength. Tensile testing was performed on the alloys in order to determine a yield strength, which was then used in the fatigue portion of the study. Fatigue testing in three point bend was conducted at four different temperatures, 22 °C, 400 °C, 600 °C, and 700 °C, the first time this novel method has ever applied to cast irons. Samples fatigued at 600 °C showed evidence of creep, and at 700 °C showed yielding, as evidenced by the micrographs and plots of position change recorder during the fatigue tests. Calculations based on the data obtained from these studies allowed determination of flexural stress, strain and modulus, and the data for each alloy were examined in relation to the Uniform Material Law for Cast Iron. From the results of this study we can conclude the following

1. The as received alloys exhibited microstructures typical of cast irons with their compositions. The main phases were ferrite, pearlite, and graphite nodules and

the HSM alloy showed greater amounts of silicon and molybdenum than 50HS, as expected. The HSM alloy has a slightly higher Young's modulus than 50HS, but all values were within reported literature values.

2. The addition of Mo reduces the corrosion rate at high temperatures. This conclusion is based on the observation that the 50HS alloy showed the development of thicker oxide layers than the HSM alloy.

3. While Mo slows corrosion it does not necessarily slow grain growth due to diffusion. After each heat treatment slightly larger grains were found in the HSM alloy as compared to the 50HS.

4. The amount of pearlite found in the HSM alloy was greater than in the 50HS alloy. This is a result of the addition of Mo to the alloy, Molybdenum can act to slow the diffusion of carbon from the pearlite, which gives the matrix greater strength and fatigue resistance at higher temperatures.

5. While the moduli of both alloys decreased as a function of temperature, the 50HS alloy showed anomalous results above 400° where the modulus for the 600° testing was found to fall in between the 22° and 400° results, and rather than eventually becoming linear over time remained to increase throughout the time of the test, while the HSM continued to follow the observed trend. It is concluded that the presence of Mo forms carbides at grain boundaries at high temperatures that aid in precipitate hardening, which increase its tensile strength, thermal fatigue life and creep resistance.

6. The uniform material law for cast iron is not applicable for either alloy under all temperatures. To test the applicability of this law, data from the more stable alloy (HSM) of this study was inserted into the equation, where the predicted values of strain amplitude were much higher than experimental values for 22 °C, and values that were much lower when compared to the 400 °C experimental data. It was concluded that the second alloy would not be applicable if the more stable alloy did not fit the prediction.

7. Given that the UMLCI was not suitable for predicting behavior, curves were fit to the experimental data for the flexural modulus values, comparing both the historical and instantaneous data. In all cases the equations used for the fitting were either linear or exponential. From this one can conclude the behavior of the material, particularly the HSM alloy performed in a stable way up to 600 °C. The 50HS alloy performed in a stable way up to 400 °C, but did not exhibit stability beyond this temperature.

8. Throughout this work, one alloy, HSM, indicated more favorable traits which would lend itself to perform better at high temperature. It is concluded that the addition of silicon and molybdenum to cast iron can increase the stability of high temperature modulus, reduce the amount of oxidation found on the outer surface of the material, and maintain a greater amount of pearlite throughout temperatures to just over 600 °C.

Although the fatigue testing was not able to be performed as initially intended, and the intended model for this research was not applicable, an

important aspect was produced from the overall process. It was possible to successfully do high temperature – three point bend fatigue, and from these tests make calculations for the flexural stress, flexural strain and more importantly, the flexural modulus of the material. A recent review of literature has not indicated that this is something that has been done to date. The importance of this lies in the ability to determine material properties at high temperature in a less expensive, yet accurate fashion.

Further research is needed in the determination of the relationship between the flexural calculations, and those values obtained by more standard means. Given the successful of three point bend fatigue testing of cast iron at high temperature, there is promising evidence that an existing fatigue limit model could be modified and/or adapted to predict high temperature fatigue generated in three point bend, given the appropriate resources of time and financial support.

REFERENCES

1. Wagner, D. B. (1993). *Iron and steel in ancient China* (Vol. 9). Brill.
2. Imhoff, W. G. *Puddle Cinder as a Blast Furnace Iron Ore*, *Journal of the Cleveland Engineering Society* 1917, 9(5), Index (621.76): p.322-323.
3. Scoffern, J. *The useful metals and their alloys* (5th ed.), Houlston & Wright, London, 1857 p. 6.
4. Thomas J. M. *A Nation of Steel: The Making of Modern America, 1865–1925*.: Johns Hopkins University Press, Baltimore, 1995; p. 32–39
5. Rosato, V. (1989). *Comparative behavior of carbon in BCC and FCC iron*. *Acta Metallurgica*, 37(10), 2759-2763.
6. Cast Irons, Edited by J.R. Davis., ASM International. Handbook Committee, Materials Park, Ohio : ASM International 1996
7. Lucas, A. (2006). *Wind, water, work: ancient and medieval milling technology* (Vol. 8). Brill.
8. Misa, T. J. (1998). *A nation of steel: The making of modern America, 1865-1925* (Vol. 7). JHU Press.
9. Ihm, M., & Automotive, T. R. W. (2011). Introduction to gray cast iron brake rotor metallurgy. In *TRW Automotive, Seminar*.
10. William F. Smith, & Hashemi, J. (2006). *Foundations of materials science and engineering*. Mcgraw-Hill Publishing.
11. DeGarmo, E. P., Black, J. T., & Kohser, R. A. (2011). *DeGarmo's materials and processes in manufacturing*. John Wiley & Sons.
12. Understanding Cast Irons - White Iron, 2010, <http://www.atlasfdry.com/white-iron.htm>
13. Brown, J. R. (Ed.). (1994). *Foseco Foundryman's Handbook*. Butterworth-Heinemann.
14. Castings, M. I. (1960). Malleable Founders Society. *Cleveland, OH*.
15. Ductile Iron Data for Design Engineers [Online] <http://www.ductile.org/didata/Section2/2intro.htm>
16. Callister, W. D., & Rethwisch, D. G. (2007). *Materials science and engineering: an introduction* (Vol. 7, pp. 665-715). New York: Wiley.
17. Bain, E. C., & Paxton, H. W. (1966). Alloying elements in steel. 1966, 291 P. AMERICAN SOCIETY FOR METALS, METALS PARK, OHIO.
18. Gillespie, LaRoux K. (1988). *Troubleshooting manufacturing processes* (4th ed.). SME. p. 4-4
19. Craig, B., Introduction to Environmentally Induced Cracking, ASM Handbook (2003) Vol. 13A. ASM, Metals Park, OH, 383-389.
20. Evans, H. E., Hilton, D. A., Holm, R. A., & Webster, S. J. (1983). Influence of silicon additions on the oxidation resistance of a stainless steel. *Oxidation of Metals*, 19(1-2), 1-18.
21. Stott, F. H., Gabriel, G. J., Wei, F. I., & Wood, G. C. (1987). The development of silicon-containing oxides during the oxidation of iron-chromium-base alloys. *Materials and Corrosion*, 38(9), 521-531.
22. Caplan, D., & Cohen, M. (1965). Scaling of Fe-26Cr Alloys at 870°–1200° C. *Journal of The Electrochemical Society*, 112(5), 471-477.

23. Jones, D. E., & Stringer, J. (1975). The effect of small amounts of silicon on the oxidation of high-purity Co-25 wt. % Cr at elevated temperatures. *Oxidation of Metals*, 9(5), 409-413.
24. Evans, H. E. (1995). Stress effects in high temperature oxidation of metals. *International materials reviews*, 40(1), 1-40.
25. Douglass, D. L., & Armijo, J. S. (1970). The effect of silicon and manganese on the oxidation mechanism of Ni-20 Cr. *Oxidation of Metals*, 2(2), 207-231.
26. Li, B., & Gleeson, B. (2004). Effects of minor elements on the cyclic-oxidation behavior of commercial Fe-base 800-series alloys. *Oxidation of metals*, 62(1-2), 45-69.
27. Revesz, A. G., & Fehlner, F. P. (1981). The role of noncrystalline films in the oxidation and corrosion of metals. *Oxidation of metals*, 15(3-4), 297-321.
28. Bennett, M. J., Desport, J. A., & Labun, P. A. (1984). Analytical electron microscopy of a selective oxide scale formed on 20% Cr-25% Ni-Nb stainless steel. *Oxidation of metals*, 22(5-6), 291-306.
29. Y. Saito, T. Maruyama, and T. Amano, *Proceedings of the International Symposium on High Temperature Corrosion*, Marseille, France, p. 61 (1986).
30. Kumar, A., & Douglass, D. L. (1976). Modification of the oxidation behavior of high-purity austenitic Fe-14Cr-14Ni by the addition of silicon. *Oxidation of Metals*, 10(1), 1-22.
31. Young, D. J., & Gleeson, B. (2002). Alloy phase transformations driven by high temperature corrosion processes. *Corrosion Science*, 44(2), 345-357.
32. B. Gleeson, in *Corrosion and Environmental Degradation of Materials*, V.II: Materials Science and Technology V.19, Wiley-VCH, Weinheim, Germany, pp174-228 (2000).
33. Logani, R., & Smeltzer, W. W. (1969). Kinetics of wustite-fayalite scale formation on iron-silicon alloys. *Oxidation of metals*, 1(1), 3-21.
34. Logani, R. C., & Smeltzer, W. W. (1971). The growth of wustite-fayalite nodules on an iron-1.5 wt. % silicon alloy exposed to carbon dioxide-carbon monoxide atmospheres. *Oxidation of Metals*, 3(3), 279-290.
35. P. Kofstad and R. Bredesen, *Proceedings: 9th International Congress on Metallic Corrosion*, (National Research Council of Canada, Ottawa, June, 1984), p.12.
36. A. Rahmel, J. Tobolski, Influence of water vapour and carbon dioxide on the oxidation of iron-silicon alloys in oxygen at temperatures of 750 to 1050°C *Materials and Corrosion*, 16, 662 (1965).
37. Sheasby, J. S., Boggs, W. E., & Turkdogan, E. T. (1984). Scale growth on steels at 1200 C: rationale of rate and morphology. *Metal Science*, 18(3), 127-136.
38. Lee, V. H. J., Gleeson, B., & Young, D. J. (2005). Scaling of carbon steel in simulated reheat furnace atmospheres. *Oxidation of metals*, 63(1-2), 15-31.
39. Hsu, H. S. (1986). The formation of multilayer scales on pure metals. *Oxidation of metals*, 26(5-6), 315-332. Wellman, R. G., & Nicholls, J. R.

- (2004). High temperature erosion–oxidation mechanisms, maps and models. *Wear*, 256(9), 907-917.
40. Wellman, R. G., & Nicholls, J. R. (2004). High temperature erosion–oxidation mechanisms, maps and models. *Wear*, 256(9), 907-917.
 41. Schütze, M. (1993). Mechanical aspects of high-temperature oxidation. *Corrosion science*, 35(5), 955-963.
 42. Nagl, M. M., & Evans, W. T. (1993). The mechanical failure of oxide scales under tensile or compressive load. *Journal of Materials Science*, 28(23), 6247-6260.
 43. Hancock, P., & Nicholls, J. R. (1994). Failure of oxide scales. *Materials at high temperatures*, 12(2-3), 209-218.
 44. Hancock, P., & Nicholls, J. R. (1988). Application of fracture mechanics to failure of surface oxide scales. *Materials science and technology*, 4(5), 398-406.
 45. J P Wilber, J. R Nichols and M.J Bennet, in Microscopy of Oxidation 3, S.B. Newcomb and J.A. Little (Eds), The Institute of Materials Book 675, London, 1997.
 46. Stephenson, D. J., & Nicholls, J. R. (1995). Modelling the influence of surface oxidation on high temperature erosion. *Wear*, 186, 284-290.
 47. Tuck, C. W., Odgers, M., & Sachs, K. (1969). The oxidation of iron at 950 C in oxygen/water vapour mixtures. *Corrosion Science*, 9(4), 271-285.
 48. Rahmel, A., & Tobolski, J. (1965). Einfluss von wasserdampf und kohlendioxid auf die oxydation von eisen in sauerstoff bei hohen temperaturen. *Corrosion Science*, 5(5), 333-346.
 49. Saunders, S. R. J., Monteiro, M., & Rizzo, F. (2008). The oxidation behaviour of metals and alloys at high temperatures in atmospheres containing water vapour: A review. *Progress in Materials Science*, 53(5), 775-837.
 50. Central Electricity Research Laboratories, & Armitt, J. (1978). *The Spalling of Steam-grown Oxide from Superheater and Reheater Tube Steels: Final Report*. Electric Power Research Institute.
 51. Nishimura, N., Komai, N., Hirayama, Y., & Masuyama, F. (2005). Japanese experience with steam oxidation of advanced heat-resistant steel tubes in power boilers. *Materials at High Temperatures*, 22(1-2), 3-10.
 52. Höschler, K., Bischof, J., & Koschel, W. (2002). Thermo-mechanical analysis of an automotive diesel engine exhaust manifold. *European Structural Integrity Society*, 29, 299-308.
 53. Zeytin, H. K., Kubilay, C., Aydin, H., Ebrinc, A. A., & Aydemir, B. (2009). Effect of microstructure on exhaust manifold cracks produced from SiMo ductile iron. *Journal of Iron and Steel Research, International*, 16(3), 32-36.
 54. Antolovich, S. D., & Saxena, A. (2002). Thermomechanical fatigue: mechanisms and practical life analysis. *Materials Park, OH: ASM International*, 2002, 738-748.
 55. Ting, J. C., & Lawrence, F. V. (1993). MODELING THE LONG-LIFE FATIGUE BEHAVIOR OF A CAST ALUMINUM ALLOY. *Fatigue & Fracture of Engineering Materials & Structures*, 16(6), 631-647.

56. Skallerud, B., Iveland, T., & Härkegård, G. (1993). Fatigue life assessment of aluminum alloys with casting defects. *Engineering Fracture Mechanics*, 44(6), 857-874.
57. Zeytin, H. K., Kubilay, C., Aydin, H., Ebrinc, A. A., & Aydemir, B. (2009). Effect of microstructure on exhaust manifold cracks produced from SiMo ductile iron. *Journal of Iron and Steel Research, International*, 16(3), 32-36.
58. Davis, J. R. (Ed.). (1996). *ASM specialty handbook: cast irons*. ASM international.
59. Shirani, M., & Härkegård, G. (2011). Fatigue life distribution and size effect in ductile cast iron for wind turbine components. *Engineering Failure Analysis*, 18(1), 12-24.
60. Mourujärvi, A., Widell, K., Saukkonen, T., & Hänninen, H. (2009). Influence of chunky graphite on mechanical and fatigue properties of heavy-section cast iron. *Fatigue & Fracture of Engineering Materials & Structures*, 32(5), 379-390.
61. Iwabuchi, Y., Narita, H., & Tsumura, O. (2003). Toughness and ductility of heavy-walled ferritic spheroidal-graphite iron castings. *Research Reports Kushiro National College*, 37, 1-9.
62. Nilsson, K. F., & Vokál, V. (2009). Analysis of ductile cast iron tensile tests to relate ductility variation to casting defects and material microstructure. *Materials Science and Engineering: A*, 502(1), 54-63.
63. Clement, P., Angeli, J. P., & Pineau, A. (1984). Short crack behaviour in nodular cast iron. *Fatigue & Fracture of Engineering Materials & Structures*, 7(4), 251-265.
64. Guillemer-Neel, C., Bobet, V., & Clavel, M. (1999). Cyclic deformation behaviour and Bauschinger effect in ductile cast iron. *Materials Science and Engineering: A*, 272(2), 431-442.
65. Stokes, B., Gao, N., & Reed, P. A. S. (2007). Effects of graphite nodules on crack growth behaviour of austempered ductile iron. *Materials Science and Engineering: A*, 445, 374-385.
66. Minnebo, P., Nilsson, K. F., & Blagoeva, D. (2007). Tensile, compression and fracture properties of thick-walled ductile cast iron components. *Journal of materials engineering and performance*, 16(1), 35-45.
67. Xue, H. Q., Bayraktar, E., & Bathias, C. (2008). Damage mechanism of a nodular cast iron under the very high cycle fatigue regime. *Journal of materials processing technology*, 202(1), 216-223.
68. Guillemer-Neel, C., Feaugas, X., & Clavel, M. (2000). Mechanical behavior and damage kinetics in nodular cast iron: Part I. Damage mechanisms. *Metallurgical and Materials Transactions A*, 31(12), 3063-3074.
69. Ferro, P., Lazzarin, P., & Berto, F. (2012). Fatigue properties of ductile cast iron containing chunky graphite. *Materials Science and Engineering: A*, 554, 122-128.
70. K Karsay, S. I., & Campomanes, E. (1970). Control of graphite structure in heavy ductile iron castings. *MOD CAST--AFS TRANS--*, 58(1), 85-92.

71. Källbom, R., Hamberg, K., & Björkegren, L. E. (2005). Chunky Graphite formation and influence on Mechanical Properties in Ductile Cast Iron. In *Component Design by Castings, VTT Symposium 237*.
72. Mellouli, D., Haddar, N., Köster, A., & Toure, A. M. L. (2011). Thermal fatigue of cast irons for automotive application. *Materials & Design*, 32(3), 1508-1514.
73. Black, B., Burger, G., Logan, R., Perrin, R., & Gundlach, R. (2002). *Microstructure and dimensional stability in Si-Mo ductile irons for elevated temperature applications* (No. 2002-01-2115). SAE Technical Paper.
74. Li, D., Perrin, R., Burger, G., McFarlan, D., Black, B., Logan, R., & Williams, R. (2004). *Solidification behavior, microstructure, mechanical properties, hot oxidation and thermal fatigue resistance of high silicon SiMo nodular cast irons* (No. 2004-01-0792). SAE Technical Paper.
75. Fatemi, A., & Yang, L. (1998). Cumulative fatigue damage and life prediction theories: a survey of the state of the art for homogeneous materials. *International journal of fatigue*, 20(1), 9-34.
76. Li, C. S., Yu, H. L., Deng, G. Y., Liu, X. H., & Wang, G. D. (2007). Numerical simulation of temperature field and thermal stress field of work roll during hot strip rolling. *Journal of Iron and Steel Research, International*, 14(5), 18-21.
77. Costa, N., Machado, N., & Silva, F. S. (2010). A new method for prediction of nodular cast iron fatigue limit. *International Journal of Fatigue*, 32(7), 988-995.
78. Seifert, T., Maier, G., Uihlein, A., Lang, K. H., & Riedel, H. (2010). Mechanism-based thermomechanical fatigue life prediction of cast iron. Part II: Comparison of model predictions with experiments. *International Journal of Fatigue*, 32(8), 1368-1377.
79. Damir, A. N., Elkhatib, A., & Nassef, G. (2007). Prediction of fatigue life using modal analysis for grey and ductile cast iron. *International Journal of Fatigue*, 29(3), 499-507.
80. Germann, H., Starke, P., Kerscher, E., & Eifler, D. (2010). Fatigue behaviour and lifetime calculation of the cast irons EN-GJL-250, EN-GJS-600 and EN-GJV-400. *Procedia Engineering*, 2(1), 1087-1094.
81. Metzger, M., Nieweg, B., Schweizer, C., & Seifert, T. (2013). Lifetime prediction of cast iron materials under combined thermomechanical fatigue and high cycle fatigue loading using a mechanism-based model. *International Journal of Fatigue*, 53, 58-66.
82. Laflen, J. R., & Cook, T. S. (1982). Equivalent damage: A critical assessment.
83. Golos, K., & Ellyin, F. (1987). Generalization of cumulative damage criterion to multilevel cyclic loading. *Theoretical and Applied Fracture Mechanics*, 7(3), 169-176.
84. French, H. J. (1933). Fatigue and the Hardening of Steels. *Trans. ASST*, 21, 899-946.

85. Lim, L. C., Tay, Y. K., & Fong, H. S. (1990). Fatigue damage and crack nucleation mechanisms at intermediate strain amplitudes. *Acta Metallurgica et Materialia*, 38(4), 595-601.
86. Kommers, J. B. (1938). The effect of overstressing and understressing in fatigue. In *Proc. American Society for Testing and Materials* (Vol. 38, pp. 249-268).
87. Miller, K. J. (1970). An experimental linear cumulative-damage law. *The Journal of Strain Analysis for Engineering Design*, 5(3), 177-184.
88. Baldwin, E. E., Sokol, G. J., & Coffin, L. F. (1957). *Cyclic strain fatigue studies on AISI type 347 stainless steel* (No. KAPL-M-EEB-16). Knolls Atomic Power Lab., Schenectady, NY.
89. Ekström, M., & Jonsson, S. (2014). High-temperature mechanical-and fatigue properties of cast alloys intended for use in exhaust manifolds. *Materials Science and Engineering: A*, 616, 78-87.
90. Basquin O.H.: The experimental law of endurance test, Proceedings of ASTM, Philadelphia, Vol. 10, 1910, pp. 625–630
91. Coffin, L. F. Jr., " A Study of the Effects of Cyclic Thermal Stresses on a Ductile Metal," TRANS. ASME, vol. 76, 1954, pp. 931- 949
92. Hollomon, JH, 1945. Tensile deformation. Trans. AIME 162, p. 268-290.
93. Dieter, G.E., Mechanical Metallurgy, 3rd ed., McGraw-Hill Book Co., London, 1988, pp. 387–94.
94. Boller, C., & Seeger, T. (1990). *Materials Data for Cyclic Loading: Low-alloy Steels*. Elsevier.
95. Korkmaz, S. (2011). A methodology to predict fatigue life of cast iron: uniform material law for cast iron. *Journal of Iron and Steel Research, International*, 18(8), 42-45.
96. Antolovich, S. D., & Saxena, A. (2002). Thermomechanical fatigue: mechanisms and practical life analysis. *Materials Park, OH: ASM International*, 2002, 738-748.
97. Kim, Y. J., Jang, H., & Oh, Y. J. (2009). High-temperature low-cycle fatigue property of heat-resistant ductile-cast irons. *Metallurgical and Materials Transactions A*, 40(9), 2087-2097.
98. Dieter, G.E., Mechanical Metallurgy, SI Metric Editions, McGraw-Hill Book Co., London (1988) 310-313
99. Meyers, M. A., Chawala, K. K., Mechanical Behavior of Materials, Prentice-Hall Inc., New Jersey (1999) 240-243
100. Young, D. J., & Gleeson, B. (2002). Alloy phase transformations driven by high temperature corrosion processes. *Corrosion Science*, 44(2), 345-357.
101. Gleeson, B. : Corrosion and Environmental Degradation of Materials, V.II: Materials Science and Technology V.19, 1st ed., Wiley-VCH, Weinheim, Germany, 2000, pp. 174–228.
102. Li, D., Perrin, R., Burger, G., McFarlan, D., Black, B., Logan, R., & Williams, R. (2004). *Solidification behavior, microstructure, mechanical properties, hot oxidation and thermal fatigue resistance of high silicon SiMo nodular cast irons* (No. 2004-01-0792). SAE Technical Paper.

103. Park, S. H., Kim, J. M., Kim, H. J., Ko, S. J., Park, H. S., & Lim, J. D. (2005). *Development of a heat resistant cast iron alloy for engine exhaust manifolds* (No. 2005-01-1688). SAE Technical Paper.
104. Tholence, F., & Norell, M. (2005). Nitride precipitation during high temperature corrosion of ductile cast irons in synthetic exhaust gases. *Journal of Physics and Chemistry of Solids*, 66(2), 530-534.
105. Tholence, F., & Norell, M. (2002). AES characterization of oxide grains formed on ductile cast irons in exhaust environments. *Surface and interface analysis*, 34(1), 535-539.
106. Tholence, F., & Norell, M. (2008). High temperature corrosion of cast alloys in exhaust environments I-ductile cast irons. *Oxidation of Metals*, 69(1-2), 13-36.
107. Čanžar, P., Tonković, Z., & Kodvanj, J. (2012). Microstructure influence on fatigue behaviour of nodular cast iron. *Materials Science and Engineering: A*, 556, 88-99.
108. Ferro, P., Lazzarin, P., & Berto, F. (2012). Fatigue properties of ductile cast iron containing chunky graphite. *Materials Science and Engineering: A*, 554, 122-128.
109. Era, H., Kishitake, K., Nagai, K., & Zhang, Z. Z. (1992). Elastic modulus and continuous yielding behaviour of ferritic spheroidal graphite cast iron. *Materials science and technology*, 8(3), 257-262.
110. Park, S. H., Kim, J. M., Kim, H. J., Ko, S. J., Park, H. S., & Lim, J. D. (2005). *Development of a heat resistant cast iron alloy for engine exhaust manifolds* (No. 2005-01-1688). SAE Technical Paper.
111. Dodd, J. (1979). Gray and Nodular Alloyed and High-Strength Irons. *BCIRA*, 24.
112. Fairhurst, W., & Rohrig, K. (1979). High-silicon nodular irons. *Foundry Trade Journal*, 146(3159), 657-681.
113. Chijiwa, K., Hayashi, M. (1979) *Journal of The Faculty of Engineering, The University of Tokyo (B)*, Vol. 35, No.2, pp.205-230
114. Black, B., Burger, G., Logan, R., Perrin, R., & Gundlach, R. (2002). *Microstructure and dimensional stability in Si-Mo ductile irons for elevated temperature applications* (No. 2002-01-2115). SAE Technical Paper.
115. Fujita, N., Ohmura, K., & Yamamoto, A. (2003). Changes of microstructures and high temperature properties during high temperature service of Niobium added ferritic stainless steels. *Materials Science and Engineering: A*, 351(1), 272-281.
116. Yoon, S. S., Lee, K. O., Lee, S. B., & Park, K. H. (2004). Thermal stress and fatigue analysis of exhaust manifold. *Key engineering materials*, 261, 1203-1208.
117. Loveday, M. S., (1982), High temperature and time dependent mechanical testing: an historical introduction, Measurement of high temperature mechanical properties of materials, London, HMSO, pp. 1-9
118. Suresh, S. (2004). *Fatigue of materials*. Cambridge university press, 152-154.

119. Murakami, Y. (2012). Material defects as the basis of fatigue design. *International Journal of Fatigue*, 41, 2-10.
120. Rudnev, V., Loveless, D., Cook, R. L., & Black, M. (2002). Handbook of induction heating. CRC Press.
121. Tensile Strength to Hardness Conversion Chart [Online]
<https://www.mwsc.com/kb/articles/19990630e.htm>
122. Callister, William D., Materials science and engineering: an introduction, John Wiley & Sons, 2000.
123. Lyons, William C. and Plisga, Gary J. (eds.) Standard Handbook of Petroleum & Natural Gas Engineering, Elsevier, 2006
124. Tanaka, K., Y. Nakai, and M. Yamashita. "Fatigue growth threshold of small cracks." *International Journal of fracture* 17.5 (1981): 519-533.
125. El Haddad, M. H., T. H. Topper, and K. N. Smith. "Prediction of non propagating cracks." *Engineering Fracture Mechanics* 11.3 (1979): 573-584.
126. Lukáš, P., et al. "NON-DAMAGING NOTCHES IN FATIGUE*." *Fatigue & fracture of engineering materials & structures* 9.3 (1986): 195-204.
127. Murakami, Yukitaka. Metal fatigue: effects of small defects and nonmetallic inclusions: effects of small defects and nonmetallic inclusions. Elsevier, 2002.
128. Dekazinczy, F. "Effect of small defects on the fatigue properties of medium-strength cast steel." *J IRON STEEL INST.* 208.9 (1970): 851-855.
129. Mitchell, M. R. "Review of the mechanical properties of cast steels with emphasis on fatigue behavior and the influence of microdiscontinuities." *Journal of Engineering Materials and Technology* 99.4 (1977): 329-343.
130. Costa, Nuno, Nuno Machado, and Filipe Samuel Silva. "Influence of graphite nodules geometrical features on fatigue life of high-strength nodular cast iron." *Journal of Materials Engineering and Performance* 17.3 (2008): 352-362.

APPENDIX A

THEORIES OF FATIGUE ESTIMATIONS

Table A1. Summary of theories on fatigue damage prior to 1970

Model	Model developer	Year	Physical basis ^a	Expression	Characteristics ^b	Ref.
Miner LDR	Miner	1945	Constant energy absorption per cycle (CON)	$D = \sum n_i/N_i = \sum r_i$	LDE, nLLD, nLIA, nSC, many Appl (popular), S	2
Machlin theory (metallurgic LDR)	Machlin	1949	Constant dislocation generation per cycle (CON)	$D = \sum n_i \int_0^{r_i} R_{pl} dt$	LDE, nLLD, nLIA, nSC, nAppl, C	208
Strain version of LDR	Coffin	1956	Directly converted from stress version	$D = \frac{\sum n_i (\Delta \epsilon_p)^{2/r}}{C^{1/r}}$	LDE, nLLD, nLIA, nSC, some Appl, G	18
Marco–Starkey theory	Marco and Starkey	1954	Conceptual (CON)	$D = \sum r_i, x_i > 1$	nLDE, LLD, nLIA, nAppl, S	23
Henry theory	Henry	1955	Endurance limit change (PHE)	$D = \frac{\sigma_{co} - \sigma_c}{\sigma_{co}} = \sum \frac{r_i}{1 + (1 - r_i) \gamma_i}$	nLDE, LLD, nLIA, SC, few Appl, G	22
Gatts theory	Gatts	1961	Endurance limit change (PHE)	$\gamma_c = \frac{\sigma_c}{\sigma_{co}} = \gamma_o \left[1 - \frac{1}{\gamma_o - 1} \frac{1}{\gamma_o - 1} (1 - r) \right]$	nLDE, LLD, nLIA, SC, few Appl, C	27
Bluhm's hypothesis	Bluhm	1961	Endurance limit change (CON)	$d_n = \gamma_{on} - \gamma_{on-1} $	nLDE, LLD, nLIA, SC, nAppl, C	29
Corten–Dolon model	Corten and Dolon	1956	Number of damage nuclei (CON)	$D = \sum m_i p_i n_i$	nLDE, LLD, LIA, SC, few Appl, G	30
Frudenthal–Heller theory	Frudenthal and Heller	1959	Fictitious life curve, probabilistic analysis (sANA)	$D = \sum \left(\frac{n_i \omega_i}{N_i} \right)$ where ω_i is an interaction factor	nLDE, LLD, LIA, nSC, some Appl, G	31
Grover's two-stage damage theory	Grover	1960	Crack initiation and crack propagation, two-stage linear evolution (CON)	$\sum \frac{n_i}{\alpha_i N_i} = 1$ for initiation stage $\sum \frac{m_i}{(1 - \alpha_i) N_i} = 1$ for propagation stage	Two-stage LDE, LLD, nLIA, nSC, few Appl, S	36
Double linear damage rule (DLDR)	Manson <i>et al.</i>	1966	Crack initiation and crack	$\sum \frac{n_i}{N_{i,i}} = \sum \frac{n_i}{N_i - p N_i^{0.6}} = 1$ for phase I	Two-stage LDE, LLD, nLIA, SC, some Appl, S	37
		1967	propagation, two-stage linear evolution (EMP)	$\sum \frac{m_i}{N_{i,i}} = \sum \frac{m_i}{p N_i^{0.6}} = 1$ for phase II		
Shanley theory	Shanley	1952	Crack growth, crack length as damage measure (PHE)	$D = \sum \left(\frac{a_n}{a_c} \right)^{1/r}$	nLDE, LLD, nLIA, nSC, few Appl, G	40
Valluri theory	Valluri	1961	Crack growth and dislocation, fracture mechanics (sANA)	$\frac{da}{dN} = C f(\sigma) a$	nLDE, LLD, some Appl, G	41
Scharton–Crandall theory	Scharton and Crandall	1966	Crack growth fracture mechanics (sANA)	$\frac{da}{dN} = a^{m+1} f(\sigma)$	nLDE, LLD, some Appl, G	43

^aCON, conceptual; PHE, phenomenological; EXP, experimental; EMP, empirical; ANA, analytical; sANA, semi analytical

^bLDE, linear damage evolution; LLD, load level dependent; LIA, load interaction accountable; SC, small amplitude cycle damage accountable; Appl, application(s); S, simple; G, general; C, complicated; the suffix 'n' stands for 'not' or 'non'

Table A2. Cumulative fatigue damage theories: DCA, refined DLDR and DDCA

Model	Model developer	Year	Physical basis ^a	Expression	Characteristics ^b	Ref.
Damage curve approach (DCA) ^c	Manson and Halford	1981	Effective microcrack growth (PHF)	$D = \sum r_i$ with $q = (N_i/N_i)^{\beta}$ and $\beta = 0.4$	nLDE, LLD, nLIA, nSC, some Appl, G	44, 12
Refined DLDR ^c	Manson and Halford	1981	Based on DCA and linearization (EMP)	$D_i = \sum (n_i/N_i)$, $N_i = N - N_{ii}$ $B = 0.65$ $D_{ii} = \sum (n_{ii}/N_{ii})$, $N_{ii} = BN(N_i/N_i)^{\alpha}$ $\alpha = 0.25$	Two stage LDE, LLD, nSC, nLIA, many Appl, S	44, 12
Double damage curve approach (DDCA) ^c	Manson and Halford	1986	Based on both DCA and refined DLDR (EMP)	$D = \sum [(pr)_i + (1 - p_i)r_{ke}]^m$, $A = 0.35$, $k = 5$, $p = A(N_i/N_i)^{\alpha}[1 - B(N_i/N_i)^{\alpha}]$, $B = 0.65$, $\alpha = 0.25$, $\beta = 0.4$	nLDE, LLD, nLIA, nSC, some Appl, C	12

^aCON, conceptual; PHE, phenomenological; EXP, experimental; EMP, empirical; ANA, analytical; sANA, semi analytical
^bLDE, linear damage evolution; LLD, load level dependent; LIA, load interaction accountable; SC, small amplitude cycle damage accountable; Appl, application(s); S, simple; G, general; C, complicated; the suffix 'n' stands for 'not' or 'non'
^cThe constants were obtained based on experiments with Maraging 300CVM steel, SAE 4130 steel, and Ti-6Al-4V alloy

Table A3. Summary of fatigue damage hybrid theories

Model	Model developer	Year	Physical basis ^a	Expression	Characteristics ^b	Ref.
Stress version ^c	Bui-Quoc <i>et al.</i>	1971	Hybridization, endurance limit change (sANA)	$D = \frac{1 - \gamma_c}{1 - \gamma_{cc}} = \sum \frac{r_i}{\left(r_i + (1 - r_i) \frac{\gamma_i - (\gamma_i/\gamma_c)_m}{\gamma_i - 1} \right)}$ $m = 8$	nLDE, LLD, nLIA, SC, some Appl, C	209
Strain version ^c	Bui-Quoc <i>et al.</i>	1971	Transplanted from the stress version (sANA)	$D = \frac{1 - \lambda_c}{1 - \lambda_{cc}} = \sum \frac{r_i}{r_i + (1 - r_i) \frac{\lambda_i - (\lambda_i/\lambda_c)_m}{\lambda_i - 1}}$ $m = 8$	nLDE, LLD, nLIA, SC, some Appl, C	52
Fictitious load modification ^c	Bui-Quoc	1981	Endurance limit change, to account for load interaction effects (sANA)	$D = \sum \frac{r_i}{r_i + (1 - r_i) \frac{\lambda_i' - (\lambda_i'/\lambda_c)_m}{\lambda_i' - 1}}$ $m = 8$	nLDE, LLD, LIA, SC, few Appl, C	51, 55
Cycle-ratio modification ^c	Bui-Quoc	1982	Endurance limit change, to account for load interaction effects (sANA)	$D = \sum \frac{r_k}{r_k + (1 - r_k) \frac{\lambda_k - (\lambda_k/\lambda_c)_m}{\lambda_k - 1}}$ $m = 8$	nLDE, LLD, LIA, SC, some Appl, C	55, 56

^aCON, conceptual; PHE, phenomenological; EXP, experimental; EMP, empirical; ANA, analytical; sANA, semi analytical
^bLDE, linear damage evolution; LLD, load level dependent; LIA, load interaction accountable; SC, small amplitude cycle damage accountable; Appl, application(s); S, simple; G, general; C, complicated; the suffix 'n' stands for 'not' or 'non'
^cThe constant $m = 8$ was determined from experiments with A-201 and A-517 steels

Table A4. Summary of fatigue damage theories based on crack growth

Model	Model developer	Year	Physical basis ^a	Expression	Characteristics ^b	Ref.
Double exponential law (1st version)	Miller and Zachariah	1977	Two-stage crack growth (PHE)	$N_{1,2} = N_{r_1} \left(\frac{r_1 + r_2 - 1}{r_2} \right)$	nLDE, LLD, nLIA, nSC, a few Appl. C	91
Double exponential law (2nd version)	Ibrahim and Miller	1980 1981	Two-stage crack growth (PHE & EMP)	$r_2 = (1 - r_1) \left(\frac{1}{1 - r_{1,1}} \right) \ln \left(\frac{a_{1,1}}{a_i} \right) / \ln \left(\frac{a_0}{a_i} \right)$ $D = \frac{a}{a_i} = \left(\frac{a_i}{a_i} \right)^{2(1 - r_1)}$	nLDE, LLD, nLIA, nSC, some Appl. C	92 93
Short crack theory	Miller	1982	MSC, PSC, E-P fracture mechanics (sANA)	$\frac{da}{dN} = A(\Delta\gamma)^m (d - a)$ for MSCs: $a_0 \leq a \leq a_i$ $\frac{da}{dN} = B(\Delta\gamma)^m a - C$ for PSCs: $a_i \leq a \leq a_1$	Clear physical basis, it is difficult to determine the micro-parameters involved	95-99
Ma-Laird theory	Ma and Laird	1989	Crack population (PHE)	$D = \Sigma(P/P_{crit}) = K \Sigma n_i [(\Delta\gamma_i/2)^{\alpha_i} - (\Delta\gamma_i/2)_{lim}]$	LIA, few Appl, not universal, G	104
Vasek-Polak model	Vasek and Polak	1991	Microcrack kinetics equivalent crack length (PHE & sANA)	$D = 2D_0 r$ for initiation: $D \leq r \leq 1/2$ $D = D_c + \frac{D_c}{m} [e^{m2r} - 1]$ for propagation: $1/2 \leq r \leq 1$	Two-stage nLDE, LLD, nLIA, nSC, few Appl. C	105

^aCON, conceptual; PHE, phenomenological; EXP, experimental; EMP, empirical; ANA, analytical; sANA, semi analytical

^bLDE, linear damage evolution; LLD, load level dependent; LIA, load interaction accountable; SC, small amplitude cycle damage accountable; Appl, application(s); S, simple; G, general; C, complicated; the suffix 'n' stands for 'not' or 'non'

Table A5. Summary of fatigue damage theories based on modify life curves

Model	Model developer	Year	Physical basis ^a	Expression	Characteristics ^b	Ref.
Subramanyan model	Subramanyan	1976	Convergence to the knee-point (CON)	$r_i = 1 - (r_{i-1} + [r_{i-2} + \dots + (r_2 + r_1^n) r^{n-1}]^{1/n}, \dots, 1)_{i=0, \dots, i-1}$	LDE, LIA, nSC, some Appl. G	106
Hashin-Rotem theory	Hashin and Rotem	1978	Two types of convergence (CON)	Formulation based on static strength point, and formulation based on endurance limit point	LDE, LIA, nSC, some Appl. G	107
Bound theory	Ben-Amoz	1990	Upper and lower bounds of convergence lines (sANA)	Bounds formed by Miner rule and Subramanyan model; bounds formed by DLDR and Subramanyan model; and statistical bounds	LDE, LIA, nSC, few Appl. C	109-111
Leipholtz's approach	Leipholtz	1985	Experimental determination (EXP)	Modified life curve is obtained from repeated multi-level block tests	LDE, LIA, SC, a few Appl. G, E	112,113

^aCON, conceptual; PHE, phenomenological; EXP, experimental; EMP, empirical; ANA, analytical; sANA, semi analytical

^bLDE, linear damage evolution; LLD, load level dependent; LIA, load interaction accountable; SC, small amplitude cycle damage accountable; Appl, application(s); S, simple; G, general; C, complicated; the suffix 'n' stands for 'not' or 'non'

Table A6. Summary of fatigue damage energy based theories

Model	Model developer	Year	Physical basis ^a	Expression	Characteristics ^a	Ref.
Plastic strain energy (hysteresis energy)	Kujawski and Ellyin	1984	Convergence, plastic strain energy, (CON)	In the plastic strain energy vs life diagram, isodamage curves converge to the apparent fatigue limit, rather than to the original limit	LDE, LIA, SC, few Appl, G, E	124
Total strain energy	Golos and Ellyin	1987	Convergence, total strain energy, (sANA)	In the total strain energy vs life diagram, isodamage curves converge to the apparent fatigue limit, rather than to the original limit	LDE, LIA, SC, some Appl, G, E	11,126,127
Bui-Quoc model	Bui-Quoc	1973	Constant total plastic energy at failure (CON)	$W_f = \sum n_i \Delta W_i = \frac{2K' M_i^{n'+1}}{n'+1} \sum \epsilon_i N_i^{-(n'+1)}$	Energy version of LDR, few Appl, G	137
Radhakrishnan approach	Radhakrishnan	1978	Crack growth rate is related to plastic energy (CON)	$r_n = 1 - \sum_{i=1}^{n-1} \frac{W_i}{W_{tot}} \epsilon_i$	Another energy version of LDR, few Appl, G	138
Kliman Theory	Kliman	1984	Block spectrum, similar basis to the above (CON)	$D_b = \frac{W_b}{W_{gr}} = \frac{1}{W_{gr}} \sum \Delta W_i \theta_i$	Also energy version of LDR, a few Appl, G	140
Niu theory	Niu <i>et al.</i>	1987	Strain hardening and plastic strain energy (sANA)	$D = \Phi^{(2n_1)^{n_2} + n_3 + n_4} = \sum \epsilon_i^{(2n_1)^{n_2} + n_3}$	nLDE, LLD, LIA, SC, some Appl, C	135, 156
Leis model	Leis	1988	Related to two exponents in strain-life equation (CON)	$D = \frac{4\sigma'_f}{E} (2N_f)^{2n_1} + 4\sigma'_f \epsilon'_f (2N_f)^{n_2 + n_3}$	nLDE, LLD, LIA, SC, nAppl, G	133

^aCON, conceptual; PHE, phenomenological; EXP, experimental; EMP, empirical; ANA, analytical; sANA, semi analytical

^bLDE, linear damage evolution; LLD, load level dependent; LIA, load interaction accountable; SC, small amplitude cycle damage accountable; Appl, application(s); S, simple; G, general; C, complicated; the suffix 'n' stands for 'not' or 'non'

Table A7. Summary of continuum damage fatigue theories

Model	Model developer	Year	Physical basis ^a	Expression	Characteristics ^b	Ref.
Chaboche model	Chaboche	1974	All these models are based on the effective stress concept in CDM. The differences are the number of variables assumed in the damage rate equation and boundary conditions	$D = 1 - [1 - r^{(1+n)}]^{-1/(1+n)}$	All are in similar characteristics such as nLDE, LLD, potential to account for SC and LIA, increasing Appl. Convenience depends on the parameters used	158
Lemaitre-Plumtree model	Lemaitre and Plumtree	1979		$D = 1 - (1 - r)^{1/(1+n)}$		163
Lemaitre-Chaboche model	Lemaitre and Chaboche	1990		$D = \sum r_i^{1/(1+n)}$		145,162
		1992		$D = 1 - (1 - r)^{1/(1+n(n))}$		164
Wang model	Wang	1990		$D = D_c - (D_c - D_0)(1 - r)^{1/n}$		165
Wang-Lou model	Wang and Lou					
Li-Qian-Li model	Li <i>et al.</i>	1989	Besides above, a dislocation variable is involved (ANA)	$D = 1 - \left(\frac{\lambda_c}{\lambda_0} \right)^n r$	Similar characteristics to above, nAppl, C	166
Three-dimensional CDM model	Chow and Wei	1991	CDM approach in three-dimensional space (ANA)	A damage effective tensor was introduced and a generalized three-dimensional isotropic CDM model was proposed based on effective stress concept	Similar characteristics, nAppl, very C	171

^aCON, conceptual; PHE, phenomenological; EXP, experimental; EMP, empirical; ANA, analytical; sANA, semi-analytical

^bLDE, linear damage evolution; LLD, load level dependent; LIA, load interaction accountable; SC, small amplitude cycle damage accountable; Appl, application(s); S, simple; G, general; C, complicated; the suffix 'n' stands for 'not' or 'non'

Table A8. Summary of “other” approaches to fatigue damage

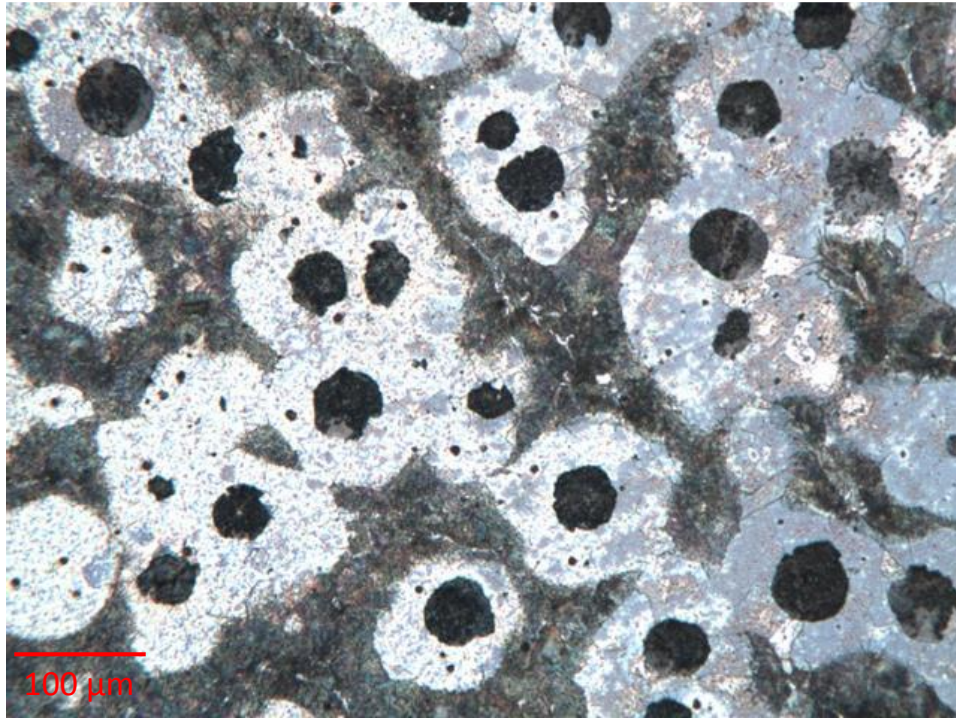
Model	Model developer	Year	Physical basis ^a	Expression	Characteristics ^b	Ref.
Surface layer stress approach	Kramer	1974	Surface layer stress change (PHE)	$D = \Sigma(\sigma_i/\sigma_i^*)$	LDE, LIA, SC, some Appl, G	172,173
ES-Miner rule	Ikai <i>et al.</i>	1989	Internal stress and effective stress evolutions (sANA)	Applied stress can be resolved into internal and effective stresses. The internal stress is representative of the fatigue resistance of a material while the effective stress is responsible for the fatigue damage	LDE, LIA, SC, few Appl, C, E	180–183
Overload damage model	Topper <i>et al.</i>	1990	Crack opening and closure (PHE)	$D = \Sigma D_{ol} + \Sigma D_{oc} + \Sigma D_{cl}$	LLD, LIA, SC, some Appl, G, E	191,192
Plastic strain evolution model	Azari <i>et al.</i>	1984	Plastic strain evolution and accumulation (PHE)	$D = \Sigma \left(\frac{\Delta \epsilon_p - \Delta \epsilon_{p,c}}{\Delta \epsilon_{p,t} - \Delta \epsilon_{p,c}} \right)_{t=1}^{i-1}$	nLDE, LLD, nLIA, nSC, few Appl, G	194
Fong theory	Fong	1982	Assuming a linear damage rate (CON)	$D = \Sigma(\epsilon_{k,i} - 1)/(\epsilon_k - 1)$ for $k \neq 0$	nLDE, LLD, few Appl, G	195
Landgraf model	Landgraf	1973	Strain version of LDR involving mean stress (CON)	$D/\text{reversal} = \frac{1}{2N_f} = \left[\frac{\sigma_f' - \sigma_m}{\epsilon_f' E} \left(\frac{\Delta \epsilon_p}{\Delta \epsilon_c} + \frac{\sigma_m}{\sigma_f'} \right) \right]_{\text{rev}}$	LDE, nLIA, nSC, σ_m involved, few Appl, G	196
Plastic work based damage model	Kurath <i>et al.</i>	1984	Plastic work, LDR, load interaction (CON)	$D_b = \sum_{i=1}^j \frac{2n_i}{(2N_f)_i} \left(\frac{\Delta \sigma_i}{\Delta \sigma_b} \right)_{i,j}$	LDE, LIA, nSC, few Appl, G	198
Unified approach	Pasic	1992	CDM and fracture mechanics (ANA)	This is an approach combining fracture mechanics with damage mechanics	Only conceptual nAppl, C	201
PSB version of LDR	Cordero <i>et al.</i>	1988	Persistent slip band density (PHE)	$\Sigma(n_i/N_i) = DS = 1 + D_2/D_1$	LDE, nLLD, few Appl, C	202
Micro-damage mechanics model	Inoue <i>et al.</i>	1987	Involving PSB parameter (ANA)	$D(\bar{N}, n) = [\Psi^*(\bar{N})/\Psi^*(\bar{N})_{\text{max}}](n/N_f)_{\text{inv}}$	nLDE, LLD, few Appl, C	203
A model based on resistance-to-flow and Halford	Abuefoutouh	1989	Change in resistance-to-flow (ANA)	$dX/dN = \pm J_{2+} \exp(cX + d)$	nLDE, LLD, LIA, SC, few Appl, C	204
A correction approach	Buch <i>et al.</i>	1982	Using correction factor C	$N^* = N_{\text{cal}}(N_{\text{cal}}/N_{\text{cal}}^*) = N_{\text{cal}}^* C$	Relying on experiment, some Appl	205,206

^aCON, conceptual; PHE, phenomenological; EXP, experimental; EMP, empirical; ANA, analytical; sANA, semi analytical

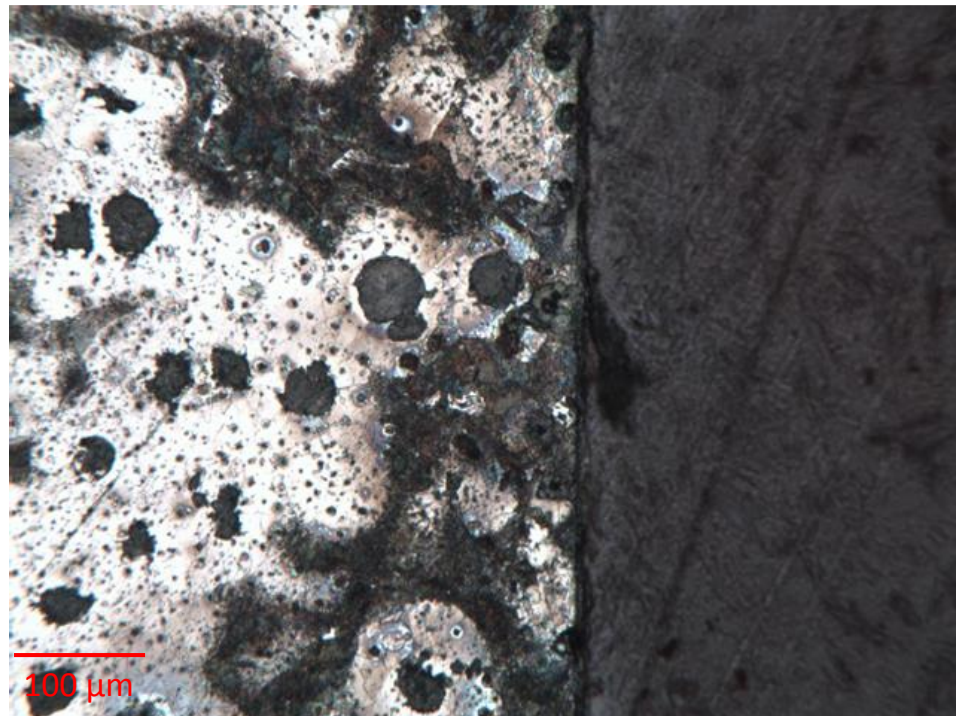
^bLDE, linear damage evolution; LLD, load level dependent; LIA, load interaction accountable; SC, small amplitude cycle damage accountable; Appl, application(s); S, simple; G, general; C, complicated; the suffix 'n' stands for 'not' or 'non'

APPENDIX B

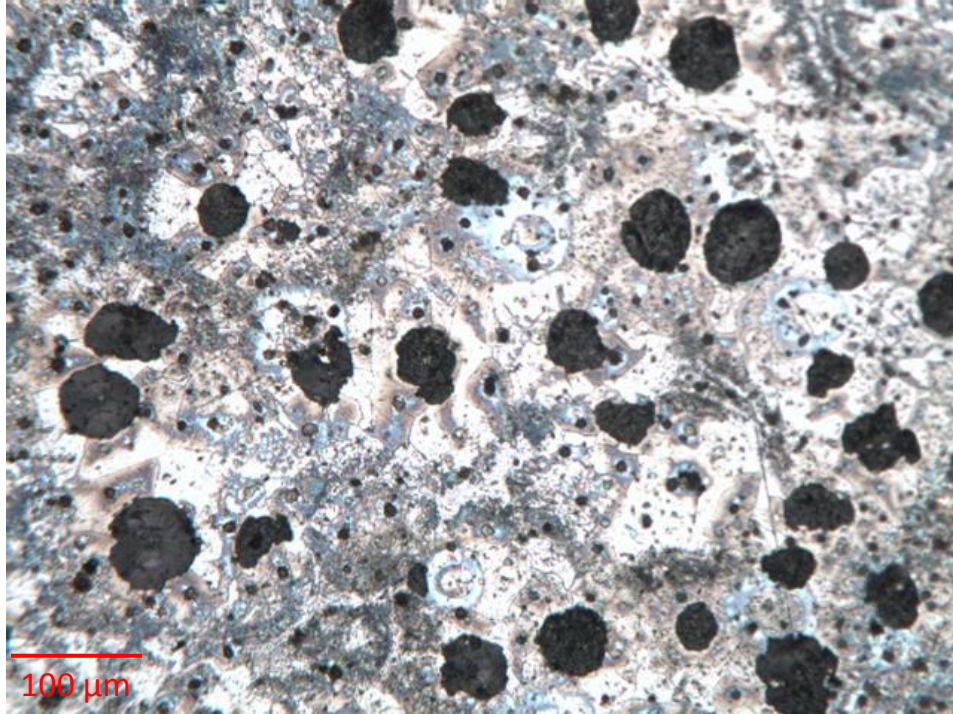
MICROSTRUCTURE IMAGES



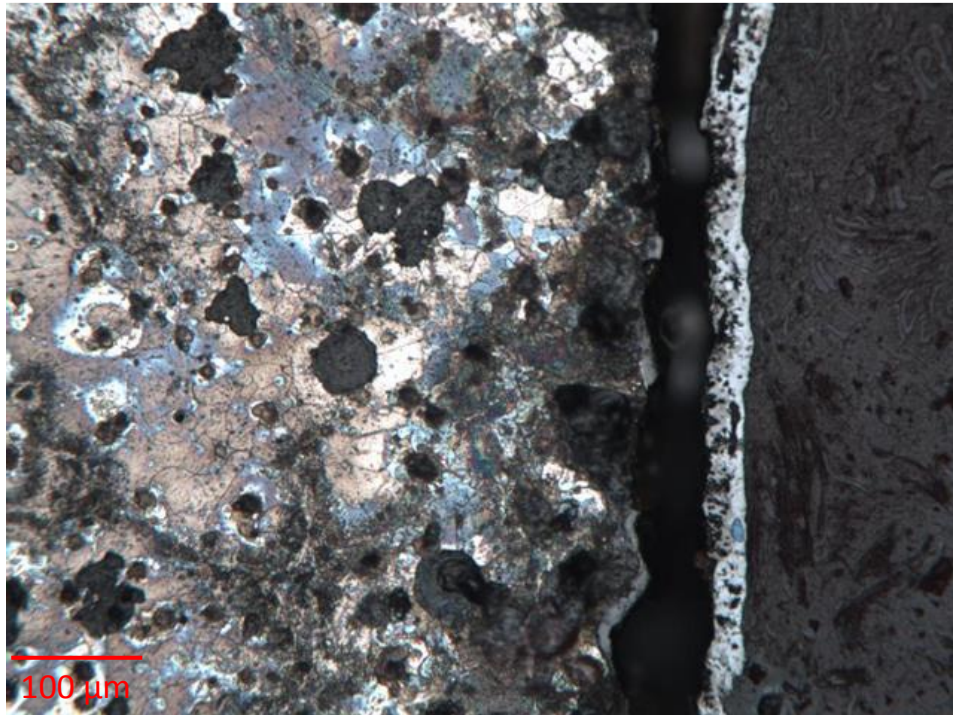
HSM Room 200X, Interior



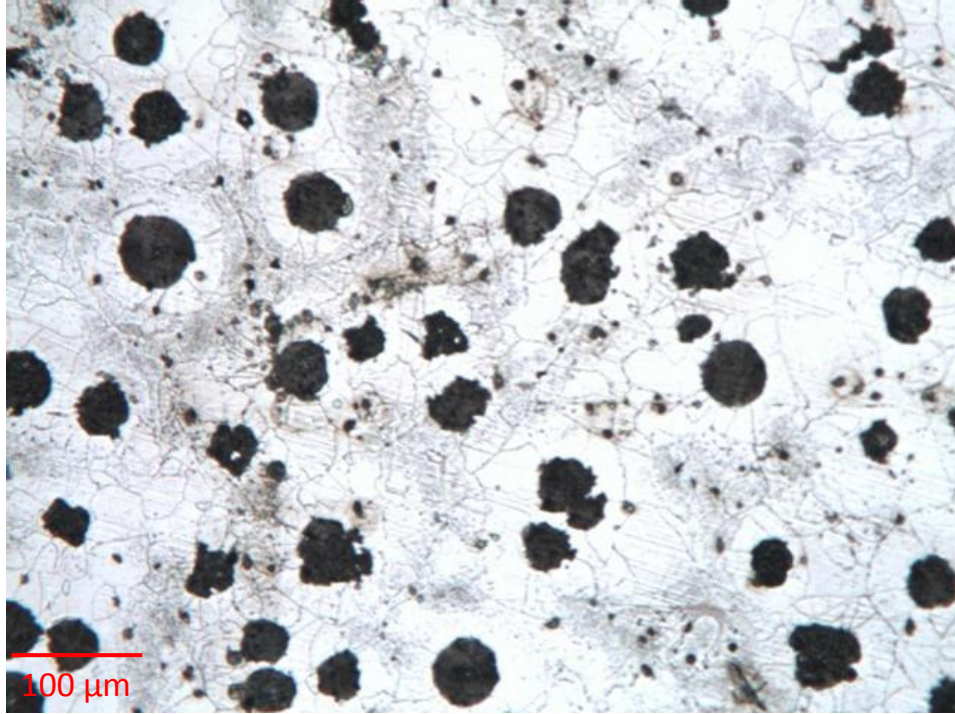
HSM Room 200X, Edge



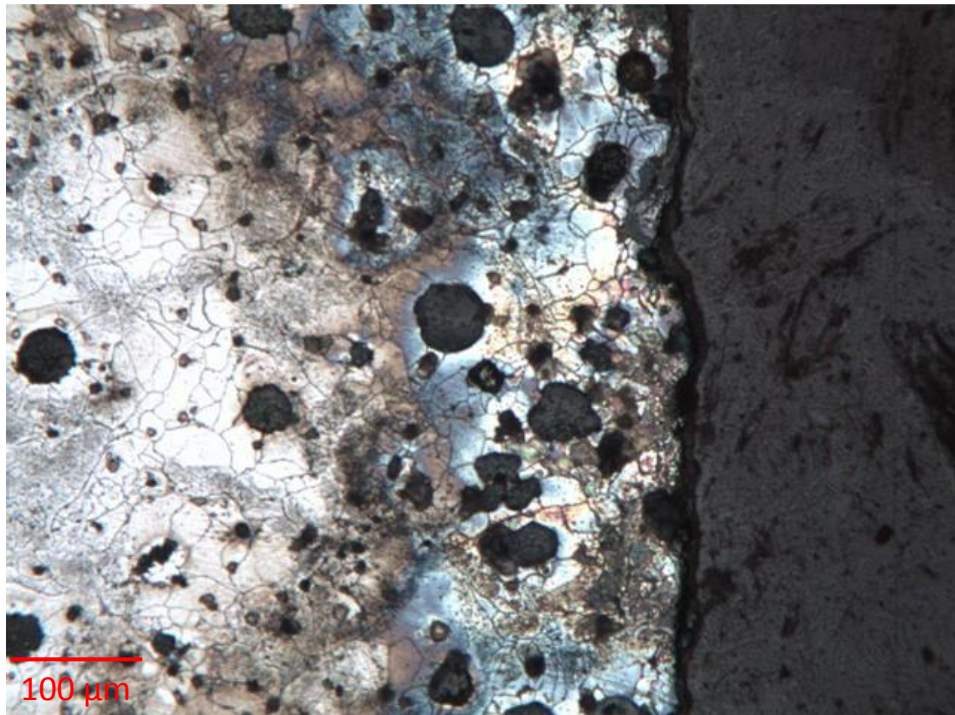
HSM 700C 200X, Interior, 30 Hour heat treatment



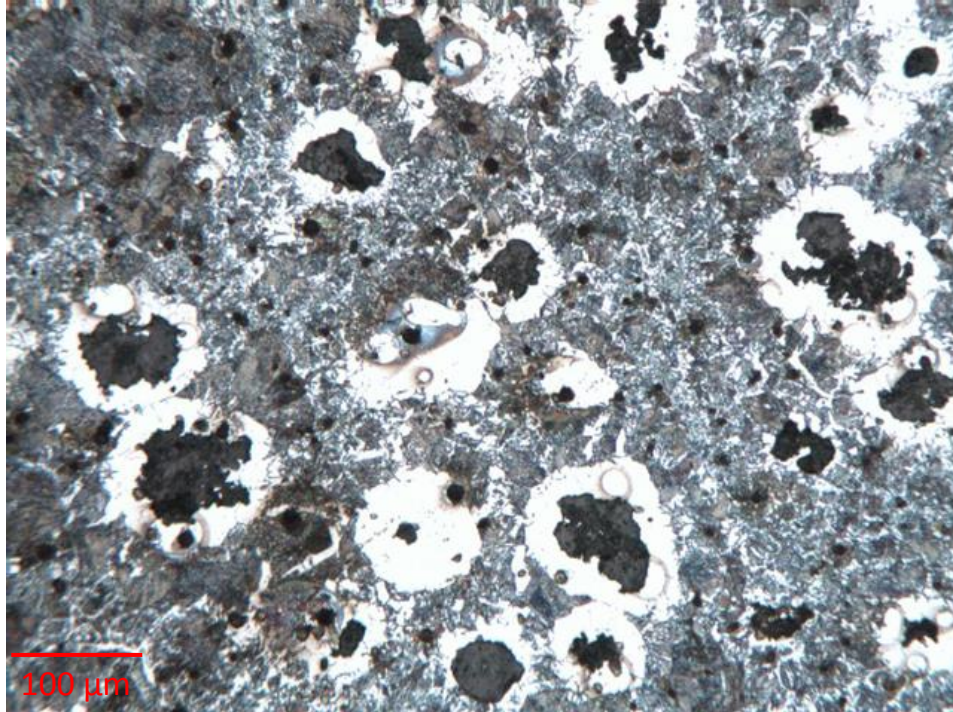
HSM 700C 200X, Edge, 30 Hour heat treatment



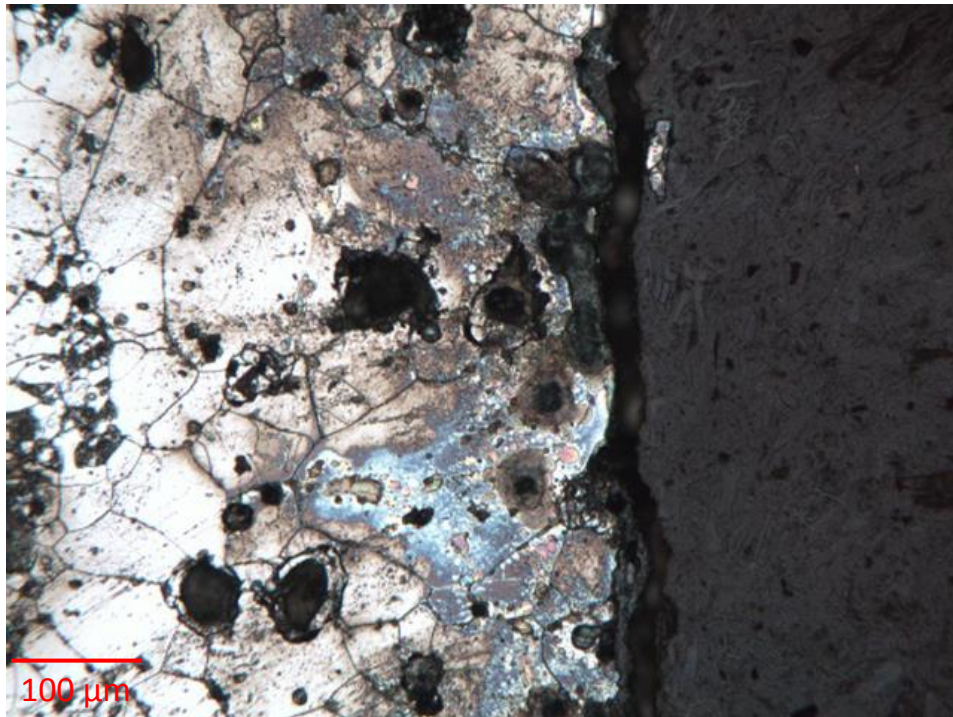
HSM 800C 200X, Interior, 30 Hour heat treatment



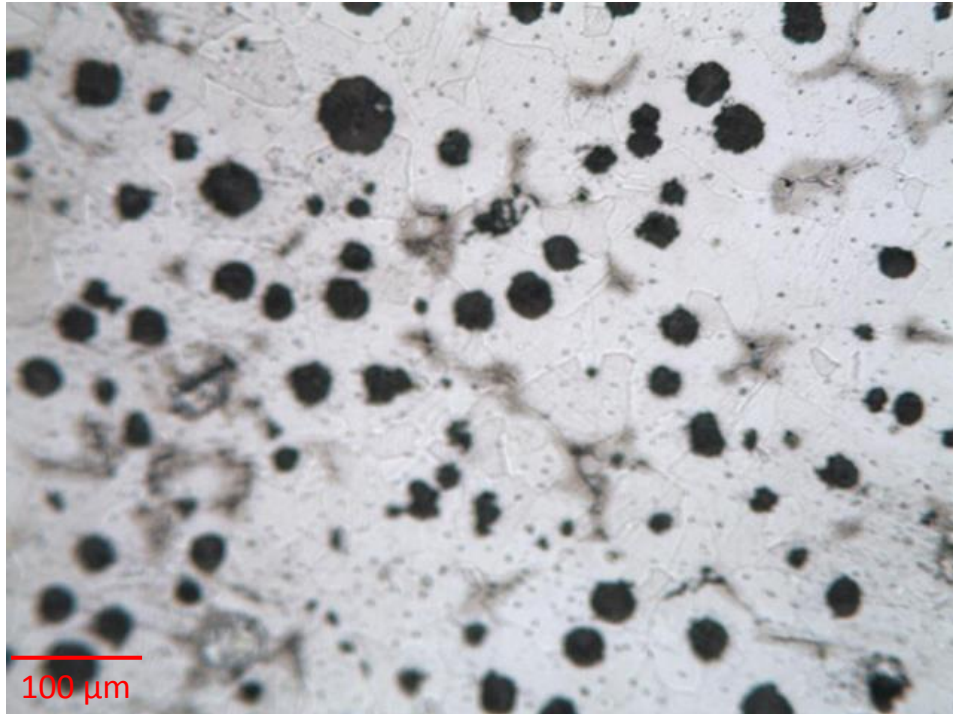
HSM 800C 200X, Edge, 30 Hour heat treatment



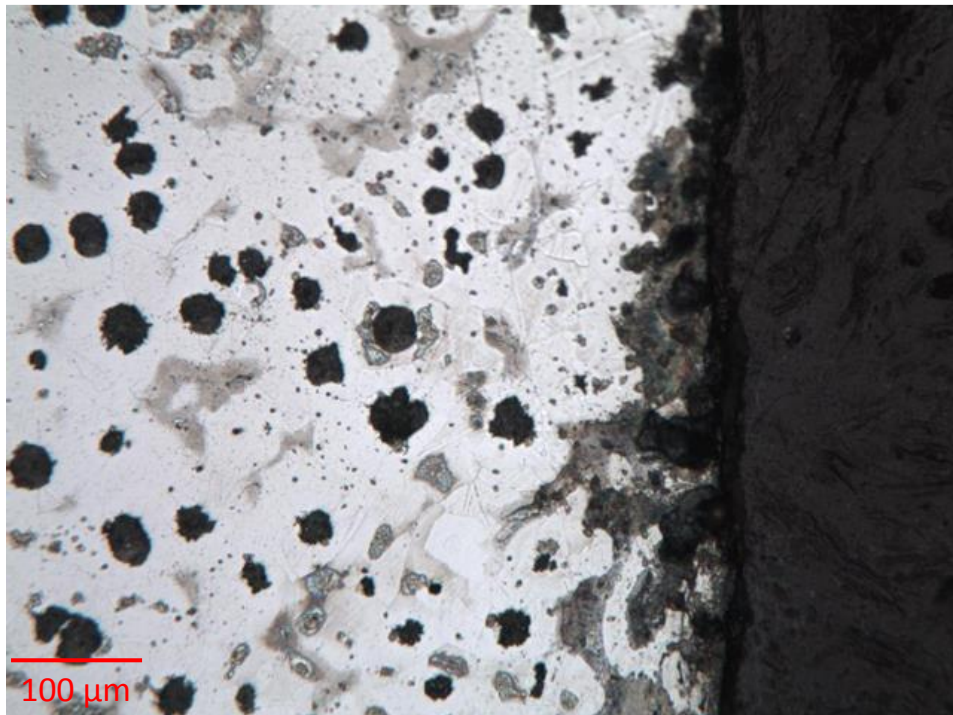
HSM 900C 200X, Interior, 30 Hour heat treatment



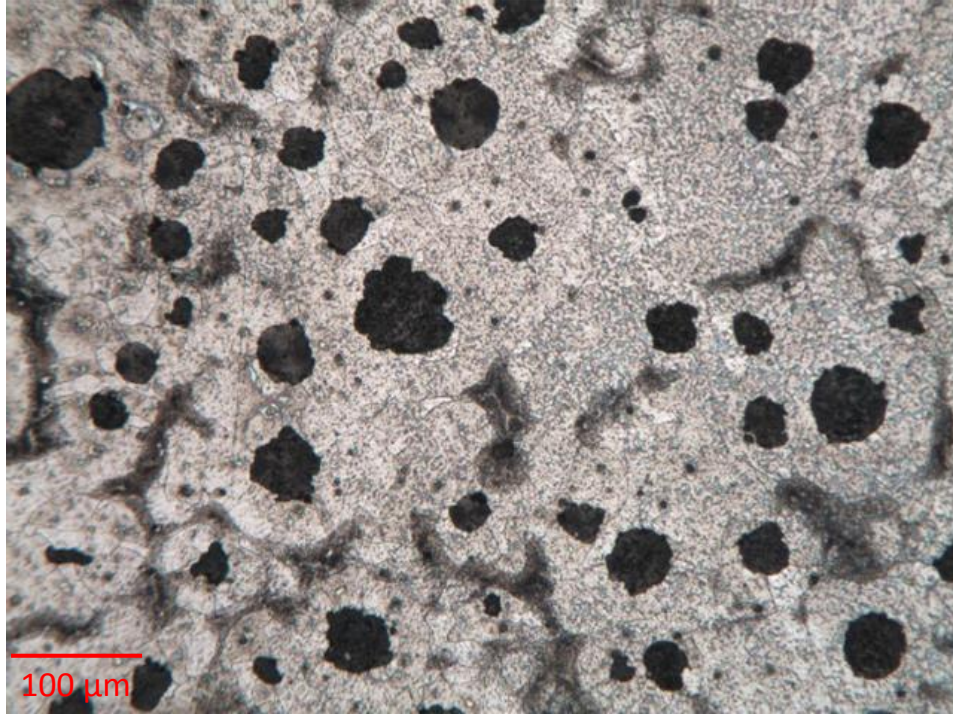
HSM 900C 200X, Edge, 30 Hour heat treatment



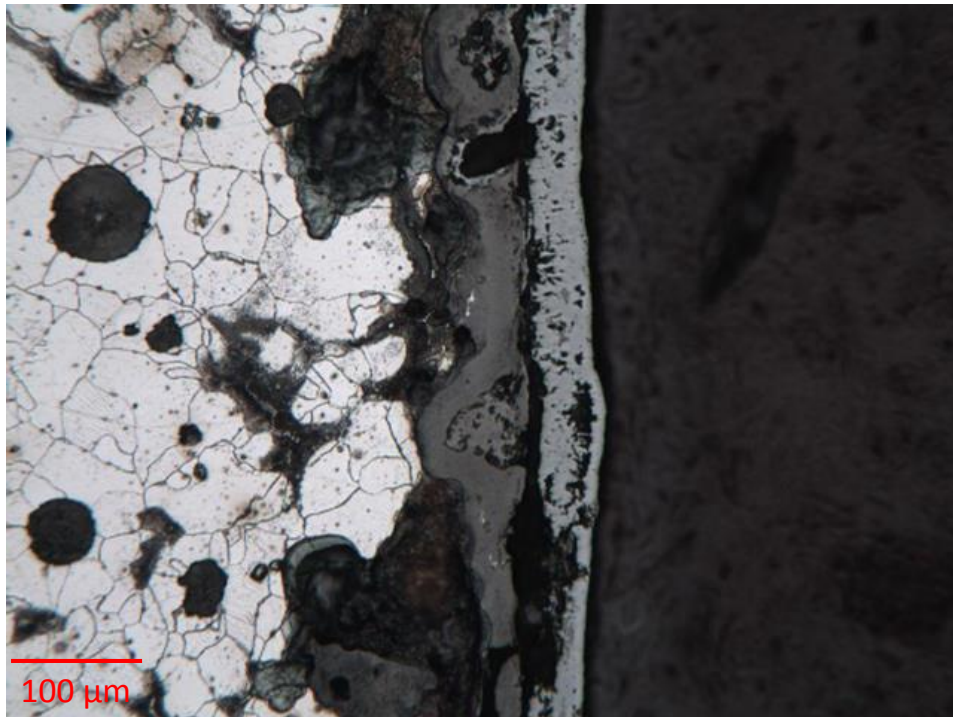
50HS Room 200X, Interior, 30 Hour heat treatment



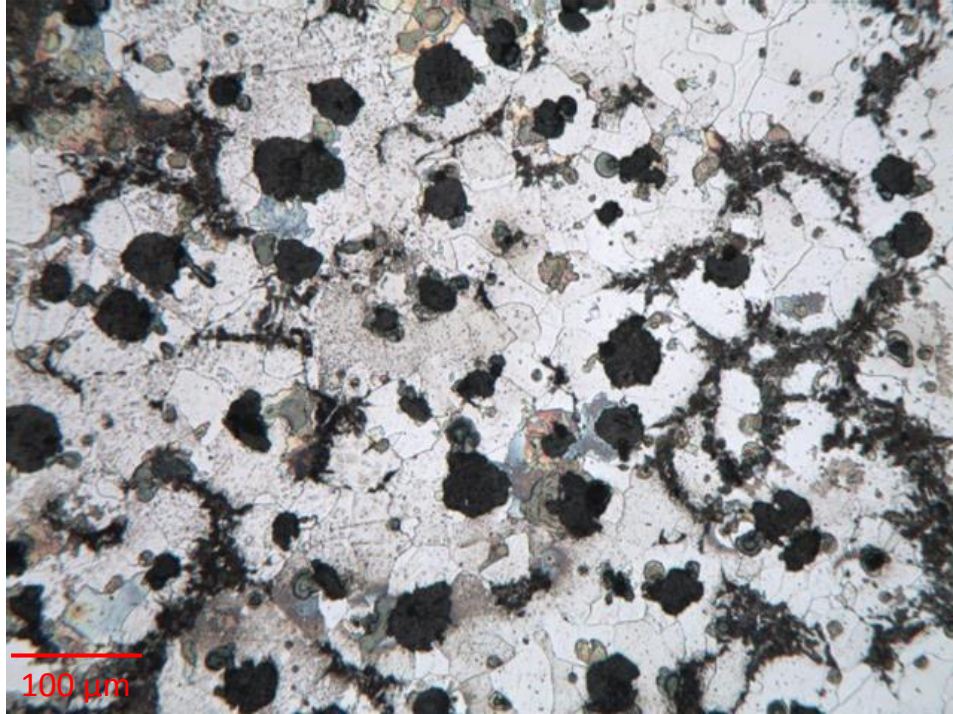
50HS Room 200X, Edge, 30 Hour heat treatment



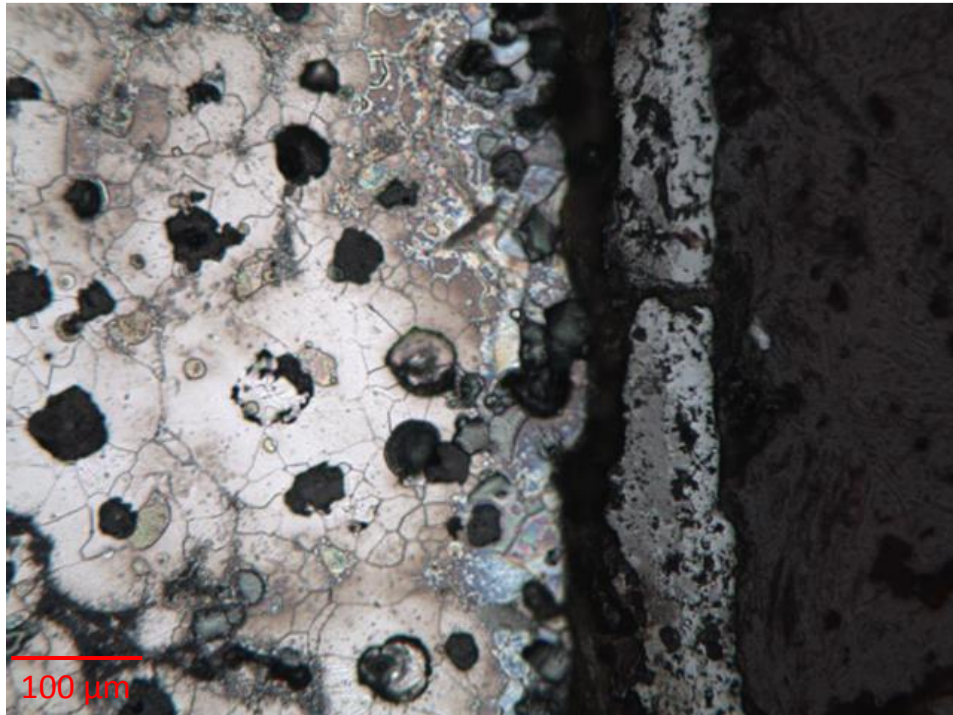
50HS 700C 200X, Interior, 30 Hour heat treatment



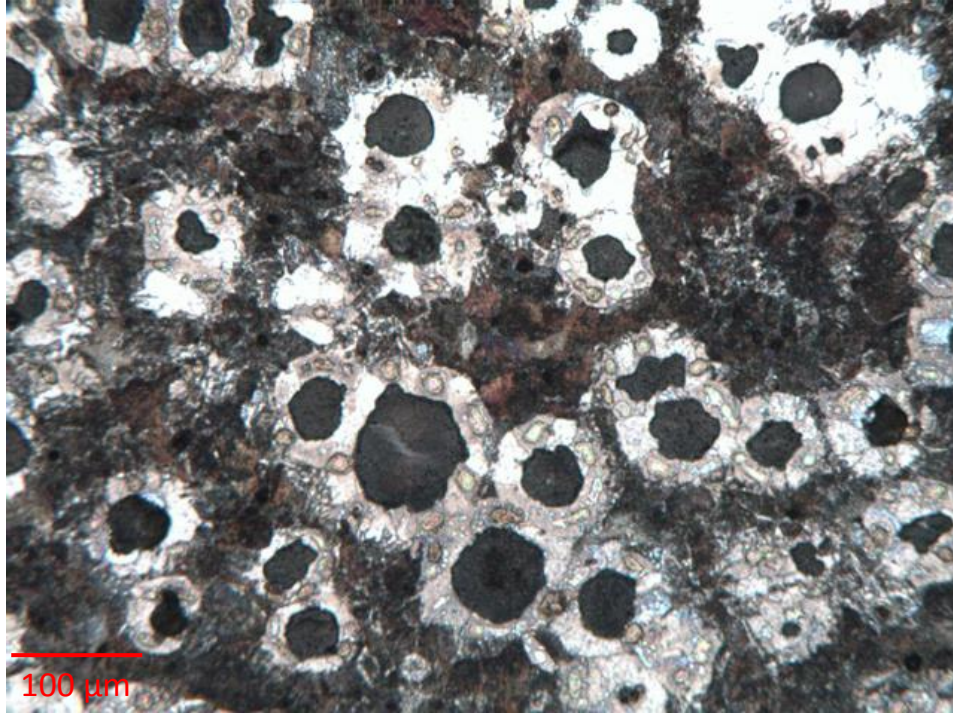
50HS 700C 200X, Edge, 30 Hour heat treatment



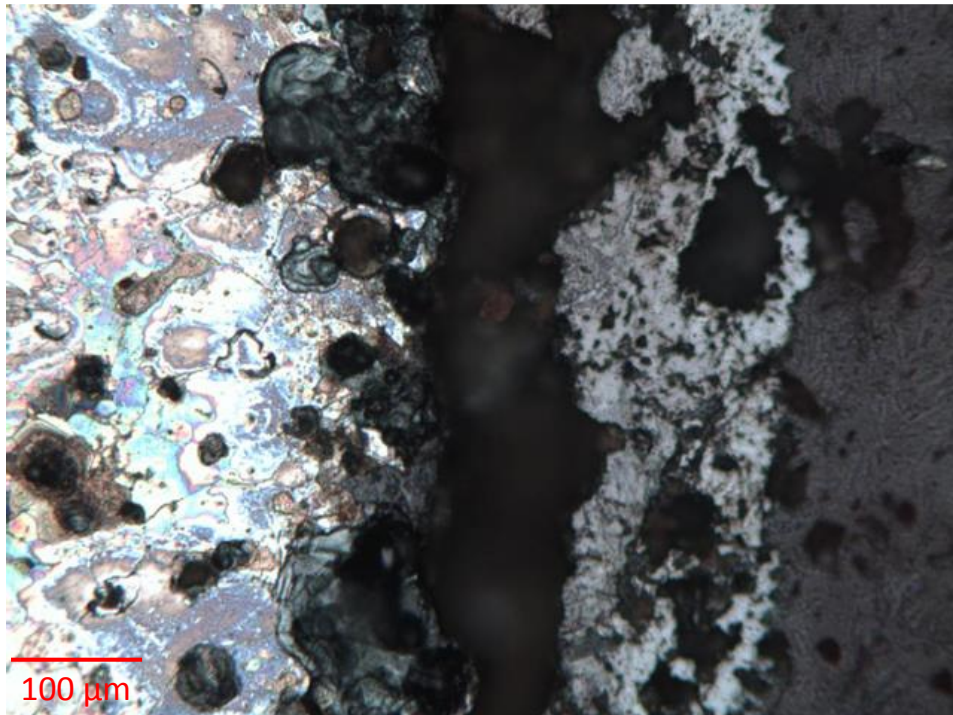
50HS 800C 200X, Interior, 30 Hour heat treatment



50HS 800C 200X, Edge, 30 Hour heat treatment



50HS 900C 200X, Interior, 30 Hour heat treatment



50HS 900C 200X, Edge, 30 Hour heat treatment

APPENDIX C

CROSS SECTION OF HSM 700 °C



HSM 700 °C 50X image of cross section from compression to tension